

# 000 001 002 003 004 005 006 007 008 009 010 011 012 013 014 015 016 017 018 019 020 021 022 023 024 025 026 027 028 029 030 031 032 033 034 035 036 037 038 039 040 041 042 043 044 045 046 047 048 049 050 051 052 053 PRACTICAL MECHANISM VIA SIMPLE INPUT CONTROL FOR FAULT-TOLERANT SPIKING NEURAL NETWORKS

Anonymous authors

Paper under double-blind review

## ABSTRACT

Spiking Neural Networks (SNNs) attract researchers due to their energy-efficient operations in neuromorphic devices. Despite their energy efficiency, hardware-implemented SNNs in neuromorphic devices are vulnerable to hardware faults, which impair the functionality of learnable parameters (e.g., Stuck-At-Faults (SAFs) in synaptic weights). This impairment reduces the capacity to absorb information. When input data contains information exceeding the capacity, SNNs may not absorb information correctly, referred to as **the bottleneck problem**. Existing approaches have relied on complex algorithms or direct modification to most synaptic weights in hardware-implemented SNNs, limiting their practicality in neuromorphic devices. This paper proposes a simple yet effective input control mechanism to address the problem, grounded in a thorough motivation study. Our mechanism divides the input samples into small fragments, following the best fragmentation strategy, derived by analyzing the characteristics of the input samples and diagnosing the current influence of faults. Experimental results demonstrate that our mechanism significantly enhances fault tolerance over existing methods, achieving these gains without complex algorithms or direct weight modification in various SNN models. Additionally, our mechanism improves the fault tolerance of SNN models implemented with actual hardware devices.

## 1 INTRODUCTION

Spiking Neural Networks (SNNs) attract researchers to develop neuromorphic devices that are necessary to implement Artificial Intelligence (AI) in low-end devices (Garaffa et al., 2021; Jeong et al., 2025). SNNs are third-generation neural networks that process data using spikes. They are well-suited for neuromorphic devices with limited power sources and biological operations, as SNNs consume less energy than other neural networks and exhibit high biological plausibility (Schuman et al., 2022; Pfeiffer & Pfeil, 2018). Although SNNs are essential for neuromorphic devices, hardware-implemented SNNs remain highly vulnerable to permanent hardware faults, which frequently occur in the electrical components of neuromorphic devices and significantly impair the SNNs' learning performance (Spyrou et al., 2021; Lee & Lim, 2023). Their fault vulnerability stems from the instability of hardware components and the fault sensitivity of SNNs' neuron models in neuromorphic devices (Garaffa et al., 2021).

Previous approaches to improve hardware-implemented SNNs' tolerance against hardware faults rely on complex algorithms to regulate abnormal neuronal activities or demand hardware reconfigurability to manage electric components directly in neuromorphic devices (Vu et al., 2019; Putra et al., 2022). Although these approaches have improved the fault tolerance of the SNNs, they exhibit the following problems that reduce their practicality in implementation.

**1. Algorithmic complexity in conventional mechanisms:** The previous approaches require complex algorithms that are impractical for hardware implementation (Vu et al., 2019; Yang et al., 2022; Han et al., 2023). These approaches cannot work properly in neuromorphic devices that demand low-power operation and prevent stable operation (Basu et al., 2018). This is because the complex algorithms frequently malfunction due to unexpected events such as wrong input values and hardware faults (Liu et al., 2017).

**2. Difficulties for direct modifications to synapses:** Modifying synaptic weights directly is essential for the previous approaches to improve hardware-implemented SNNs' fault tolerance, such as

054 **synapse pruning and weight bounding.** These approaches forcibly adjust whole synaptic weights and  
 055 configurations in neuromorphic devices (Putra et al., 2022; Chen & Chakrabarty, 2021). However,  
 056 external methods that enable direct modification require additional costs to design reconfigurable  
 057 hardware (Garaffa et al., 2021; Takano & Amano, 2022; Putra et al., 2023).

058 Pragmatic approaches for meeting these two problems are necessary to improve SNN’s fault tolerance  
 059 in the real world. To address these limitations, we identify a critical issue that significantly degrades  
 060 SNN performance in faulty neuromorphic devices through a detailed motivation study. We name this  
 061 issue **the bottleneck problem**, severely damaging SNNs’ usable learning capacity. Here, we explain  
 062 how the bottleneck problem occurs. When faults appear in SNNs’ synapses, the weights of the faulty  
 063 synapses become fixed during training. This means that the capacity is reduced because the faulty  
 064 synapses, which do not change their weight during training, cannot be used for memorizing data.  
 065 Furthermore, the pre-activation value (linear combination) of spiking neurons lies at an abnormal  
 066 point of the surrogate gradient function, causing a serious gradient vanishing problem, which results  
 067 in the capacity degradation. With the low usable capacity of faulty SNNs, they cannot memorize input  
 068 data properly when the data contains information exceeding the learning capacity. **The bottleneck**  
 069 **problem occurs in neuromorphic devices that use gradients for on-chip learning during training**  
 070 (Eslami et al., 2024; Martemucci et al., 2025). We aim to solve this problem as neuromorphic devices  
 071 with gradient-based online learning frequently suffer from hardware faults despite the necessity of  
 072 gradient-based online learning to enhance the data-processing ability of hardware-implemented SNNs  
 073 (Spyrou et al., 2021; Lee & Lim, 2023; Rostami et al., 2022; Lagorce et al., 2015; Stewart et al., 2020;  
 074 Cramer et al., 2022; Payvand et al., 2020; Renner et al., 2024; Yin et al., 2024).

075 Motivated by **flow control methods used in computer networks** (Kurose & Ross, 2012), we first  
 076 propose a practical mechanism based on **simple input control** to solve the bottleneck problem based  
 077 on **data fragmentation**. Our mechanism enhances the fault tolerance of SNNs by dividing input data  
 078 samples into small fragments. Our control scheme addresses the constraint of SNNs’ usable learning  
 079 capacity in faulty neuromorphic devices by exploiting an effective fragmentation strategy for fault  
 080 mitigation based on analysis of input images’ characteristics and the influence of faults. The novelty  
 081 of our mechanism is as follows. **Unlike the previous approaches, our mechanism does not require**  
 082 **complex algorithms to control neuronal activities and hardware reconfigurability for modifying**  
 083 **synapses directly.** This novelty is derived from the following features of our mechanism.

084 **1. Data sample division into small fragments:** Our algorithm fragments input data samples to  
 085 decrease the input samples’ size and shrink information in the input samples, leading the faulty SNN  
 086 models to memorize the information despite their degraded usable learning capacity due to faults.  
 087 **2. Fragmentation method to minimize the adverse effect from faults:** To ensure that our mechanism  
 088 provides the fragments that models can handle, we develop a fragmentation strategy that adapts  
 089 fragment geometry (i.e., the cut angle) to mitigate fault-induced damage during the forward pass.

090 We develop our mechanism through a thorough motivation study with faulty SNN models. With our  
 091 mechanism, various SNN models achieve significantly higher classification accuracy than models  
 092 using previous approaches for fault mitigation under fault-injected conditions, while consuming less  
 093 energy due to our simple approach. We additionally conduct experiments with real hardware SNNs  
 094 built in a Field-Programmable Gate Array (FPGA) device. Our work has the following contributions.

- 095 • We develop a practical mechanism to enhance hardware-implemented SNNs’ fault tolerance  
 096 without complex algorithms and direct synapse modifications, which easily malfunction and  
 097 demand high hardware reconfigurability.
- 100 • We present a concrete theoretical basis for our mechanism by mathematically and experimen-  
 101 tally investigating how synaptic faults degrade the usable learning capacity of SNN models  
 102 in our motivation study. Due to our detailed motivation study, we propose a theoretically  
 103 sound fragmentation mechanism.
- 104 • We provide a rich set of evaluation results in various scenarios, including hardware environ-  
 105 ments. The evaluation results demonstrate that our mechanism, which is based on simple  
 106 data fragmentation, improves the fault tolerance of SNNs more significantly than previous  
 107 approaches.

108  
109  

## 2 BACKGROUNDS

110  
111  

### 2.1 SPIKING NEURAL NETWORKS

112  
113  
114  
115  

SNNs are third-generation neural networks motivated by the learning mechanisms of the human brain (Yao et al., 2023). In SNNs, spiking neurons fire and emit output spikes at every time interval, corresponding to each time step. Here, the time step is a unit of time for spike occurrence. The spiking neurons generate spikes only when the membrane potential of the neurons reaches a threshold.

116  
117  
118  
119  
120  
121  
122  

Researchers use various neuron models to build SNNs. Among them, the Integrate-and-Fire (IF) model and Leaky Integrate-and-Fire (LIF) model, which have leakage in membrane potential unlike IF, are widely used (Moitra et al., 2023). Synaptic weights determine how input spikes from pre-synaptic neurons of the previous layer affect the post-synaptic neurons (Venkatesha et al., 2021). SNNs update the weights with two approaches: supervised and unsupervised learning rules. Supervised learning rules calculate gradients to update weights using surrogate gradient functions. Unsupervised learning rules utilize the time difference between pre-synaptic and post-synaptic activity to update weights.

123  
124  
125  
126  
127  
128  

SNNs are necessary to implement neuromorphic devices. They exhibit less energy consumption than conventional neural networks for the following reasons. First, spiking neurons fire and update synaptic weights only when a specific event occurs (Lee & Lim, 2024). The SNN’s infrequent spike generation is associated with sporadic data processing, resulting in low power consumption. Second, SNNs replace complex Multiply-ACcumulate (MAC) operations with simple ACcumulate (AC) operations, eliminating weight multiplication to input data while accumulating input information.

129  
130  

### 2.2 SYNAPTIC FAULTS

131  
132  
133  
134  
135  
136  
137  
138  
139  
140  
141  
142  

Synaptic faults are persistent or transient defects in the synaptic weights of a connection. They distort pre-activations and inject biased or structured noise, which disrupts the learning process of SNN models. A representative case of them is the Stuck-At Faults (SAFs), where a weight is fixed to the highest (SA1) and lowest (SA0) synaptic weight, ignoring updates and introducing systematic bias (Vatajelu et al., 2019). **In other words, SAFs make synapses permanently stuck at a max or min weight value, regardless of training or input.** Note that SA0 and SA1 do not mean the weights are stuck at the exact values 0 and 1. Another common case is Random Weight Faults (RWFs). **RWFs force synapses to randomly fluctuate around their original weight values due to thermal noise.** They transiently remove intended synaptic connections or create unintended connections (Vatajelu et al., 2019). Additionally, Connectivity Error Faults (CEFs) permanently change the connections between synapses, ruining synaptic connections. These faults shift the pre-activation away from useful operating regions, shrink the effective gradient signal, and reduce usable learning capacity.

143  
144  

## 3 STATE OF THE ARTS

145  
146  

### 3.1 ANALYSIS ABOUT FAULTS IN NEUROMORPHIC DEVICES

147  
148  
149  
150  
151  
152  
153  
154  
155  

Researchers have deeply investigated how faults affect neuromorphic devices. They inject faults into synapses and neurons of SNNs in neuromorphic devices, and how these faults ruin the classification performance of SNNs (Vatajelu et al., 2019). They build a memristive neuromorphic simulator and analyze how faults disturb data classification (Lee & Lim, 2023). In this study, researchers prove that the faults occurring in synapses correlated with important features of data samples influence the devices more severely. Researchers also apply various fault types in neuromorphic devices and study how spiking neurons act in detail (Ali El Sayed, 2021; Garaffa et al., 2021). However, these analysis studies overlook the excessive updates caused by hardware faults in neuromorphic devices.

156  
157  

### 3.2 MECHANISMS TO IMPROVE FAULT TOLERANCE OF HARDWARE-IMPLEMENTED SNNs

158  
159  
160  
161  

**The conventional methods to improve the fault tolerance of hardware-implemented SNNs in neuromorphic devices rely on modifying faulty elements and implementing additional fault-mitigation architectures.** Researchers utilize the error correction ability of binary codes in output decoding to enhance the fault tolerance of neural networks (Liu et al., 2019; Yu et al., 2023). **They also induce spikes to avoid faults of hardware-implemented SNNs in neuromorphic devices to reduce**

the bad effects caused by faults (Vu et al., 2019; Yang et al., 2022). They build a fault map of hardware-implemented SNNs to identify spiking neurons severely affected by faults and reduce these neurons’ influence in neuromorphic devices (Putra et al., 2022; Wicaksana Putra et al., 2021; Yang et al., 2022). Additionally, they mask faulty elements by setting affected pre-trained weights to zero, then retrain with per-layer threshold (Siddique & Hoque, 2023). Researchers also employ self-recovering mechanisms from astrocytes in the human brain to neuromorphic devices. With their self-recovering ability, these approaches significantly strengthen neuromorphic devices’ fault tolerance (Han et al., 2023; Varshika et al., 2023). Enhancing the astrocyte-based approaches, they augment SNNs with an astrocyte-inspired leaky integrator, stabilizing spiking dynamics and markedly improving fault tolerance (Yunusoglu et al., 2025). **Lightweight approaches, such as suppressing abnormal pre-activation, removing fault-affected neurons, and tuning thresholds, have enhanced the fault tolerance either (Saha et al., 2023; Spyrou et al., 2021; Saha et al., 2024).** Despite their enhancement of fault tolerance, these works require complex architectures based on complicated algorithms and neglect the reconfigurability of electric components in neuromorphic devices.

## 4 MOTIVATION STUDY

### 4.1 OVERVIEW

We have discovered that the faults cause the bottleneck problem with the following procedures.

1. **Synaptic faults increase the magnitude of pre-activation  $|z|$ , which is a linear combination of inputs ( $z = Wx + b$ ) (Berzal, 2025).** This is because the pre-activation changes significantly when faults perturb the weights to  $W + \Delta W$ . Here,  $W$  is the synaptic weights,  $x$  is an input sample, and  $b$  is a bias.  $\Delta W$  indicates a weight change caused by faults.
2. As  $|z|$  grows and moves away from the (spiking) threshold of spiking neurons, the surrogate gradient near the threshold collapses toward zero, so the learning signal cannot propagate backward.
3. The faulty weights are fixed to abnormal values, and the non-faulty weights barely change due to near-zero gradients. This problem significantly reduces SNNs’ usable learning capacity, creating a bottleneck that prevents the model from fitting the data it should learn.

We provide thorough explanations, describing mathematically how faults fail the learning process of SNN models in Appendix C.

### 4.2 PRE-ACTIVATION MAGNITUDE INCREASE BY FAULTS

To demonstrate that the synaptic faults cause the pre-activation magnitude to increase, we inject the SAFs ( $SA0 : SA1 = 1.75 : 9.04$ ) (Chen et al., 2017) and RWFs (representative permanent and transient faults) into 50% of synapses in a spiking Multi-Layered Perceptron (MLP) with 4 layers, VGG-7, and ResNet-18 with MNIST, CIFAR-10, and CIFAR-100 during training. We use the Poisson encoder to convert input into spikes. We observe the change in pre-activation magnitude of all neurons in the SNN models due to faults after training models with an Adam optimizer and Root-Mean-Square Error (RMSE) as a loss function. We obtain the experimental results by repeating experiments 10 times and present the pre-activation magnitude as a 95% confidence interval.

**Table 1:** Pre-activation magnitude of MLP, VGG-7, and ResNet-18 SNN models under fault injection.

	MLP(MNIST)	VGG-7(CIFAR-10)	RESNET-18(CIFAR-100)
NOMINAL	$2.7 \pm 0.13$	$8.75 \pm 2.08$	$14.54 \pm 3.56$
SAFs	$393.42 \pm 10.89$	$273.66 \pm 13.69$	$140.03 \pm 15.77$
RWFs	$8.08 \pm 1.75$	$205.73 \pm 10.27$	$103.41 \pm 11.8$

Table 1 compares the summation of the pre-activation magnitude of all spiking neurons in the MLP (LIF), VGG-7 (LIF), and ResNet-18 (IF) SNN models with and without SAF and RWF injection. Our experimental results show that SAFs and RWFs significantly increase the pre-activation magnitude around all neurons with fault-injected synapses.

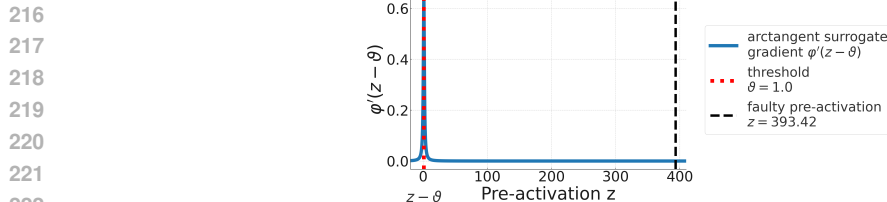


**Figure 1:** The value (average on the layers of the model) of surrogate gradient  $\phi'(z - \vartheta)$  (arctangent) when we inject SAFs into the synapses of the MLP model.

### 4.3 GRADIENT COLLAPSE BY ABNORMAL PRE-ACTIVATION MAGNITUDE

We call the region where the surrogate derivative is non-negligible the *surrogate gradient corridor* and denote its half-width by  $\delta$  (or threshold-aligned bound  $z^*$ ); outside this corridor,  $\phi'(z - \vartheta) \approx 0$ . As the pre-activation magnitude increases, the pre-activation value moves away from the corridor. This alignment error, due to an abnormal pre-activation magnitude, makes the surrogate gradient values nearly zero.

Figure 1 depicts the surrogate gradient function (arctangent) of an LIF neuron model and the position of pre-activation of the SAF-injected neurons in the MLP model. The surrogate gradient  $\phi'(z - \vartheta)$  of the SAF-injected neurons is near zero, and the gradient of these neurons vanishes. This is because the following equation calculates the gradient:  $\delta^{(l)} = (\nabla_{a^{(l)}} L) \odot \phi'(z^{(l)} - \vartheta)$  ( $L$  is a loss function and  $l$  is the index of a layer).

### 4.4 LEARNING ABILITY DEGRADATION BY GRADIENT COLLAPSE

We demonstrate that gradient vanishing due to faults causes degradation in the SNNs’ learning ability.

**Table 2:** The gradients’ L1 norm in 95% confidence interval upon all neurons and classification accuracy of MLP, VGG-7, and ResNet-18 SNN models under fault injection with 50% fault ratio.

	MLP(MNIST)	VGG-7(CIFAR-10)	RESNET-18(CIFAR-100)
NOMINAL (L1 NORM)	$11.67 \pm 1.71$	$25.68 \pm 2.89$	$7.76 \pm 1.92$
NOMINAL (ACCURACY)	$97.57 \pm 0.38\%$	$56.63 \pm 0.91\%$	$25.59 \pm 1.24\%$
SAFs (L1 NORM)	$0.01 \pm 0.00026$	$1.83 \pm 0.16$	$1.36 \pm 0.25$
SAFs (ACCURACY)	$11.35 \pm 0.01\%$	$9.99 \pm 0.08\%$	$5.04 \pm 1.07\%$
RWFs (L1 NORM)	$65.86 \pm 10.57$	$2.18 \pm 0.45$	$0.49 \pm 0.07$
RWFs (ACCURACY)	$79.8 \pm 8.74\%$	$22.28 \pm 5.34\%$	$1.5 \pm 0.51\%$

Table 2 shows the gradients’ L1 norm upon all neurons in the SNN models during training and the classification accuracy of the models with the various datasets after testing. The classification accuracy is proportional to the L1 norm of the gradient under fault injection with 50% fault ratio. This point demonstrates that vanishing surrogate gradients stall weight updates, preventing the network from making new decision boundaries and thus directly reducing its learning capacity (occurrence of the bottleneck problem). Interestingly, the MLP model does not accurately classify MNIST data samples, despite having a large gradient L1 norm, when the model is under RWF injection. This occurs because RWFs induce random changes in synaptic weights, which transiently perturb the loss and cause a temporary increase in the gradient (Foret et al., 2021). Since the MLP model has limited learning ability, it cannot effectively compensate for such perturbations.

### 4.5 PRE-ACTIVATION SENSITIVITY OF LAYERS IN MLP

Our motivation study outlines an interesting finding: in MLP, the gradients of neurons in the previous layers are more sensitive to abnormal changes in pre-activation by faults than the later layers.

Table 3 shows the gradients’ L1 norm of all neurons in each layer of the MLP model. The error signal that reaches layer  $\ell$  is obtained by repeatedly applying the Jacobians of all higher layers in MLP. Under faults, pre-activations drift away from the operating threshold, so the surrogate derivatives  $\phi'(z - \vartheta)$  on affected layers become very small. During gradient calculation, gradients are multiplicatively contracted by a chain of small factors. Because earlier layers, such as the first

270 **Table 3:** The gradients' L1 norm in a 95% confidence interval upon all neurons in each layer of the MLP model  
 271 under fault injection.

	Layer 1	Layer 2	Layer 3	Layer 4
MNIST (SAFs)	$(3.18 \pm 1.13) \times 10^{-6}$	$(3.31 \pm 1.64) \times 10^{-3}$	$(1.15 \pm 0.93) \times 10^{-3}$	$(2.67 \pm 0.65) \times 10^{-3}$
MNIST (RWFs)	$(5.61 \pm 1.46) \times 10^{-5}$	$(5.19 \pm 1.52) \times 10^{-5}$	$(1.37 \pm 0.58) \times 10^{-4}$	$(1.39 \pm 0.29) \times 10^{-3}$
FMNIST (SAFs)	$(3.45 \pm 0.91) \times 10^{-15}$	$(1.01 \pm 0.37) \times 10^{-12}$	$(1.6 \pm 0.69) \times 10^{-7}$	$(1.02 \pm 0.36) \times 10^{-2}$
FMNIST (RWFs)	$(4.91 \pm 1.55) \times 10^{-5}$	$(5.11 \pm 1.71) \times 10^{-5}$	$(1.46 \pm 0.62) \times 10^{-4}$	$(1.76 \pm 0.82) \times 10^{-3}$

277 layer (smaller  $\ell$ ), accumulate more of these factors, they suffer disproportionately severe gradient  
 278 vanishing, explaining the front-loaded degradation we observe under faults.  
 279

#### 280 4.6 SIMILARITY TO FLOW CONTROL IN COMPUTER NETWORKS

282 Data flow control mitigates the congestion problem in computer networks (Kurose & Ross, 2012;  
 283 Wigren & Karaki, 2018). The information of input samples in SNNs is related to the data in the  
 284 packets of computer networks, and the surrogate gradient corridor is related to the data capacity  
 285 that a receiver can handle in computer networks. The bottleneck problem in neural networks is also  
 286 similar to that of the receiver, which prevents the receiver from processing the large data packet  
 287 simultaneously. The objective of flow control, which involves adjusting the size of data in a packet to  
 288 satisfy the receiver's data capacity, is similar to that of enhancing fault tolerance: changing the size of  
 289 information in the input samples to maintain the pre-activation within the surrogate gradient corridor.

## 291 5 PROPOSED MECHANISM

293 Our motivation study demonstrates that synaptic faults can inflate pre-activations beyond the surrogate  
 294 gradient corridor, causing the gradient collapse. **To prevent the gradients from vanishing in hardware-**  
 295 **implemented SNNs of neuromorphic devices, we design an adaptive input fragmentation mechanism** to  
 296 **avoid drift in pre-activation magnitude based on flow control in computer networks by shrinking** the  
 297 **probability of cases where input data samples enter faulty synapses, which have abnormal weights** that  
 298 **cause the pre-activation magnitude to increase significantly.** The main idea of our paper is to  
 299 **enhance the fault tolerance of SNNs under synaptic faults by dividing inputs into fragments, selecting** the  
 300 **division angle that optimally ensures the suppression of sudden pre-activation drift in SNNs.** We  
 301 mathematically prove why our mechanism is nearly-optimal in Appendix D.

### 302 5.1 OVERVIEW

304 The proposed mechanism consists of the sensitivity score, Gini coefficient, and fragment processing  
 305 modules. Here, we briefly explain how the three modules cooperate relatively.

- 307 1. The sensitivity score module generates a sensitivity map that quantifies the extent to which each  
 308 input pixel and its associated synapses influence pre-activation under fault conditions.
- 309 2. The Gini coefficient module searches over 1D projection angles on the sensitivity map, selecting  
 310 the direction along which the accumulated sensitivity is most evenly distributed. This procedure  
 311 defines a fair axis for fragmentation.
- 312 3. Our fragment processing module cuts the image along the fair axis into equal-sensitivity fragments,  
 313 normalizes each fragment's energy via RMS normalization to keep pre-activations ( $z$ ) inside the  
 314 surrogate corridor (Zhang & Sennrich, 2019). Then, it accumulates time-step outputs with entropy-  
 315 based weighting (Qiu et al., 2025).

316 Overall, these three modules cooperate by first identifying fault-sensitive pixels, then choosing the  
 317 most balanced way to partition them, and finally enforcing the pre-activation in the surrogate corridor  
 318 by RMS normalization (Zhang & Sennrich, 2019). Moreover, we ensure the accurate decoding of  
 319 fragment-oriented outputs by the entropy-based approach (Qiu et al., 2025). We execute these three  
 320 procedures per batch.

### 321 5.2 SENSITIVITY SCORE DEFINITION AND CALCULATION

323 **Key point 1: The sensitivity score represents which pixel changes the pre-activation the most**  
**significantly under faults.**

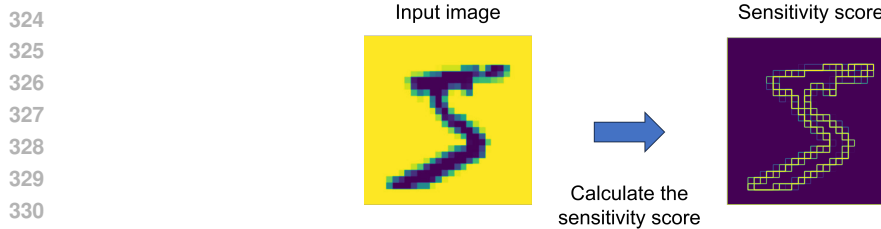
**Figure 2:** Sensitivity score calculation with an MNIST image.

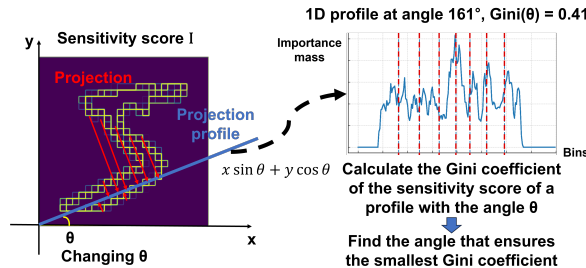
Figure 2 depicts the sensitivity score of an MNIST image. To measure how input data samples are affected by synaptic faults and explore the best fragment shape that prevents a significant increase in pre-activation magnitude, we define the sensitivity score of input samples, consisting of an image sample's complexity and the influence measurement from faults.

$$I(x) = \text{PN} \left( (\text{LoG}(x) + \text{Sobel}(x) + \text{Var}(x)) \odot (1 + \lambda_s \text{SP}(x) + \lambda_w \text{WP}(x)) \right). \quad (1)$$

where  $\text{LoG}(x)$ ,  $\text{Sobel}(x)$ , and  $\text{Var}(x)$  are information about edges, blobs, and texture contrast of images. We adopt them to calculate the complexity of an image sample and design our algorithm to minimize each fragment's complexity (Lowe, 2004). This is because an image with high complexity significantly changes the pre-activation since its norm is large.  $\text{SP}(x)$  is a saliency map (Petsiuk et al., 2018), and  $\text{WP}(x)$  is the absolute value of the first layer's weight projection to input resolution. We decide to use the first layer's weight projection since the pre-activation drift in the first layer causes the most severe gradient vanishing.  $\text{SP}(x)$  identifies the input pixels whose perturbations cause large shifts in pre-activations and, consequently, substantial changes in the final output.  $\text{WP}(x)$  converts the pixel-derived map into a fault-influence field on the weights of the first layer. We apply it to our mechanism to minimize the increase in pre-activation by reducing the probability that pixel values enter many faulty synapses at once.  $\odot$  is the Hadamard product.  $\text{PN}$  is a percentile normalization, which normalizes the values of the fault influence map in the range of 0 to 1. We adopt  $\text{PN}$  to prevent the sensitivity score from increasing excessively. For batch stability and fast operation, we measure the sensitivity score of the averaged image sample of a batch.

### 5.3 GINI COEFFICIENT CALCULATION WITH A 1D PROFILE

**Key point 2: The Gini coefficient indicates the equality of the sensitivity score (Farris, 2010). It should be minimized to increase the equality of the sensitivity score upon the fragments and prevent the pre-activation from falling outside of the surrogate gradient corridor.**

**Figure 3:** 1D projection and Gini coefficient calculation changing the projection angle.

In figure 3, we change the angle  $\theta$  of the 1D sensitivity profile and project the pixels on the 1D profile. Specifically, we transform 2D coordinated pixel position  $(x, y)$  into 1D bin index  $s$  using the equation  $s = x \sin(\theta) + y \cos(\theta)$ . Then, we calculate the Gini coefficient with equation 2 (Farris, 2010)

$$\text{Gini}(p_\theta) = \frac{1}{2L \bar{p}_\theta} \sum_{i=0}^{L-1} \sum_{j=0}^{L-1} |p_\theta[i] - p_\theta[j]|. \quad (2)$$

where,  $p_\theta$  is the 1D sensitivity profile bin obtained by projecting along an angle  $\theta$  (range of  $[0^\circ, 360^\circ]$ ).  $p_\theta[i]$  is the value of bin  $i$  ( $i = 0, \dots, L - 1$ ). In other words, we obtain  $p_\theta$  by projecting each pixel's sensitivity  $I$  onto the index of the 1D profile  $s$ , and aggregating along that axis.  $L$  is the number

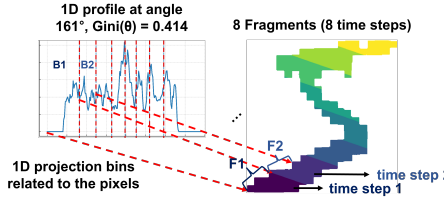
378 of bins, which is related to the granularity of angle division.  $\bar{p}_\theta$  is the mean value of  $p_\theta$  over the  
 379 number of bins ( $L$ ).  $|p_\theta[i] - p_\theta[j]|$  is absolute difference between  $p_\theta[i]$  and  $p_\theta[j]$ . We divide the sum  
 380 of pairwise absolute differences by  $(2L\bar{p}_\theta)$  for normalization, so the coefficient is 0 for a uniform  
 381 profile and grows with inequality.

382 We explore the angle  $\theta$  which makes the 1D profile have the minimum Gini coefficient. This is  
 383 because the Gini coefficient is a strictly Schur-convex function, ensuring the Gini coefficient strictly  
 384 increases under majorization: if  $x \succ y$  (i.e.,  $x$  is more unequal), then  $\text{Gini}(x) > \text{Gini}(y)$ , with  
 385 equality only for permutations (Sandor, 2007). By minimizing the Gini coefficient, the fragment's  
 386 equality of sensitivity score is maximized. We design our mechanism to maximize equality and  
 387 prevent the pre-activation from leaving the corridor. This is because as a fragment's sensitivity score  
 388 becomes more equal by minimizing Gini coefficient, the maximum of each fragment's energy  $\|x_t\|_2$   
 389 decreases, so the upper bounds  $|w^\top x_t| \leq \|w\|_2 \|x_t\|_2$  and  $|u_t| = |w^\top x_t + m|$ , ( $m = b - \vartheta$ ) are  
 390 pushed below  $\delta$ , keeping the pre-activation fixed inside the corridor ( $b$  is a bias in SNNs' layers.).

391

#### 392 5.4 FRAGMENT GENERATION BASED ON EQUAL SENSITIVITY SCORE AND IN/OUT FOR SNNs

393 **Key point 3: The fragmentation line is set by the 1D profile cutting to make the 1D bins have an**  
 394 **equal cumulative sum of the sensitivity score.**



402 **Figure 4:** Dividing an image sample based on the cumulative sum of the sensitivity score.

403 After finding the angle that ensures the minimum Gini coefficient, we calculate the cumulative sum  
 404 of the sensitivity score. As depicted in figure 4, the division line for fragmentation (dashed line in  
 405 the figure) indicates the position to cut the 1D profile into bins  $B_1, \dots, B_T$ , making the bins have  
 406 equal sensitivity score. We generate fragments  $F_1, \dots, F_T \in \{0, 1\}^{H \times W}$  with the pixels correlated  
 407 to the points in bins  $B_1, \dots, B_T$  and feed the SNN models the fragments  $F_1, \dots, F_T$  over time steps  
 408  $t = 1..T$ . We zero-pad the generated fragment to align the input dimension of fragments with the  
 409 input dimension of the original samples because the input dimension of SNNs is not changeable  
 410 during training and testing. We apply the same division angle to all data samples in the same batch.

411 To ensure that pre-activation  $z_t$  of fragment  $F_t$  positions in the corridor, keeping the scale of active  
 412 pixels in each fragment to a target Root-Mean-Square (RMS) is also important. Therefore, we adopt  
 413 RMS normalization to the input fragments with the equation 3 (Zhang & Sennrich, 2019)

$$416 \quad \tilde{x}_t = g_t x_t, \quad \|\tilde{x}_t\|_2 = \alpha \Rightarrow |z_t| \leq \|\hat{w}\|_2 \alpha. \quad (3)$$

417 where  $x_t$  is an input of time step  $t$  and  $g_t$  is the per-fragment normalization gain.  $\alpha$  is the L2 norm  
 418 of the  $\tilde{x}_t$  (the multiplication of  $x_t$  and  $g_t$ ) and denotes the non-zero pixels in the fragment for the  
 419 input of time step  $t$ . We set  $g_t$  to ensure that  $\|\hat{w}\|_2 \alpha$  is always smaller than the bound of the surrogate  
 420 corridor, placing  $z_t$  inside the surrogate-derivative corridor.

421 We also adopt an entropy-based output decoding technique to aggregate the outputs (logits) from  
 422 SNNs across all time steps accurately with the equation 4 (Qiu et al., 2025)

$$425 \quad \bar{\ell} = \sum_{t=1}^T e_t \ell_t, \quad e_t = \frac{\exp(-\tau H(\text{softmax}(\ell_t)))}{\sum_{s=1}^T \exp(-\tau H(\text{softmax}(\ell_s)))}. \quad (4)$$

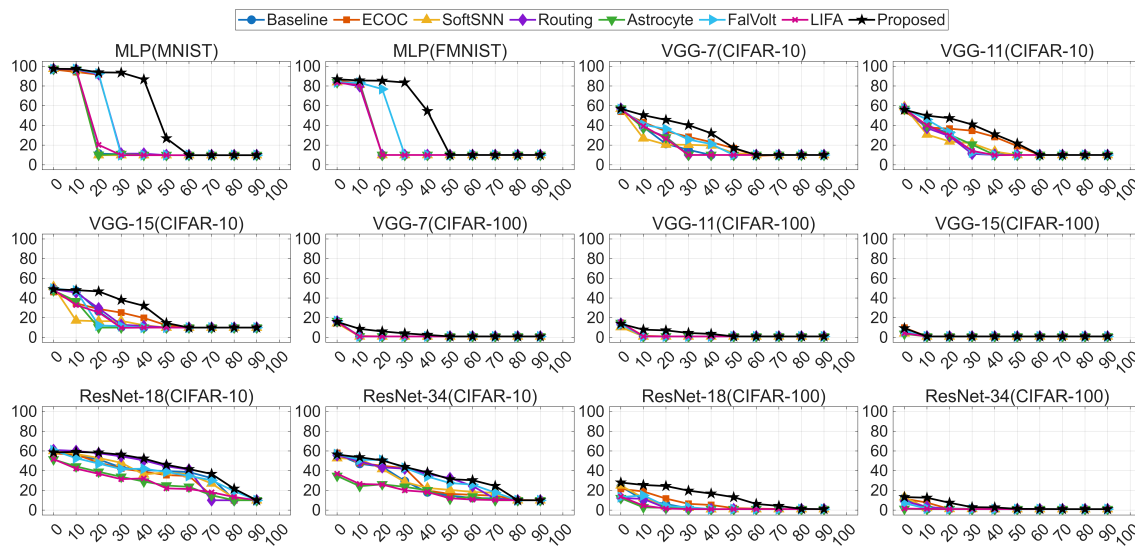
428 where  $\bar{\ell}$  is the final output vector from the entropy-weighted aggregation.  $\ell_t$  is an output vector  
 429 from SNNs at time  $t$  and  $T$  is the total number of steps.  $H(\text{softmax}(\ell_t))$  is the Shannon entropy  
 430 of the output vector's softmax result, and  $\tau$  controls how strongly low-entropy (confident) steps are  
 431 emphasized.  $e_t$  is a scaling factor to reflect the entropy of output vectors while decoding.  $\exp$  is an  
 exponential function, and  $s$  is the start index of time steps.

## 432 6 EXPERIMENTS

### 434 6.1 EXPERIMENTAL SETTINGS

436 We conduct various experiments with MLP (LIF neurons), VGG-7/11/15 (LIF neurons), and ResNet-  
 437 18/34 (IF neurons) SNN models based on SpikingJelly, widely used for SNN implementation, by  
 438 classifying samples in MNIST/FMNIST/UCI-HAR/AudioMNIST (MLP), CIFAR-10/100 (VGG  
 439 and ResNet), and Tiny-ImageNet (ResNet) (Fang et al., 2023; LeCun et al., 1998; Xiao et al., 2017;  
 440 Krizhevsky, 2009; Reyes-Ortiz et al., 2013; Becker et al., 2024; Deng et al., 2015). We select these  
 441 SNN models and datasets because current SNN technologies do not adequately train large and deep  
 442 models on complex datasets (Fang et al., 2023; Schuman et al., 2022). We measure the classification  
 443 accuracy of the SNN models using our mechanism and the benchmarks under SAFs (injected during  
 444 training), setting the ratio of SA1 and SA0 to  $SA1 : SA0 = 1.75 : 9.04$  (Chen et al., 2017) and  
 445 the weight boundary to  $[-1, 1]$  (Le Gallo et al., 2023; Lammie et al., 2022). Additionally, we inject  
 446 RWFs and CEFs into the synapses of these models. We use ECOC (Liu et al., 2019), SoftSNN  
 447 (Putra et al., 2022), Routing (Yang et al., 2022), Astrocyte (Han et al., 2023), FalVolt (Siddique &  
 448 Hoque, 2023), and LIFA (Yunusoglu et al., 2025) for our benchmarks<sup>1</sup>. The SNN models without  
 449 any fault-mitigation mechanism serve as the baseline. We use RMSE as a loss function and Adam  
 450 as the optimizer for SNN models (Fang et al., 2023). The batch size is 100, and the learning rate is  
 451 0.001 for MLP/VGG and 0.01 for ResNet. We set the number of time steps (fragments) to 2, 4, and 8.  
 452 We use 50 epochs for training. We set  $\lambda_s$ ,  $\lambda_w$  to 0.1, and  $\tau$  to 2.0 by tuning these parameters through  
 453 experimental repetition with the proposed mechanism. We repeat all experiments 10 times with  
 454 different random seeds and present the experimental results in a 95% confidence interval. We inject  
 455 faults into the synapses sporadically in a uniform distribution, resulting in the uniform position of  
 456 synaptic faults. Note that the additional results from the additional datasets (UCI-HAR, AudioMNIST,  
 457 and Tiny-ImageNet), different time steps (4 and 8 steps), other fault types (RWFs and CEFs), the  
 458 ablation study with the combination of our mechanism, various hyperparameter ( $\lambda_s$  and  $\lambda_w$ ) settings,  
 459 and the results with DNN models are presented in Appendix A. Additionally, we demonstrate that  
 460 our mechanism successfully improves the fault tolerance of hardware-implemented SNNs through  
 461 evaluations with an actual FPGA device.

### 462 6.2 CLASSIFICATION ACCURACY COMPARISON



480 **Figure 5:** Average classification accuracy of various SNN models with the baseline, benchmarks,  
 481 and proposed mechanism under SAFs using 2 time steps. The x-axis is the fault ratio (%) and the y-axis is the accuracy (%).

482 Figure 5 illustrates the classification accuracy of SNN models compared to the baseline, benchmarks,  
 483 and proposed mechanism under SAFs with 2 time steps. Under SAFs, the SNN models with our  
 484 mechanism exhibit the best classification accuracy across all datasets and models in most cases.

485 <sup>1</sup>We briefly explain how these benchmarks enhance the fault tolerance in Section 3.

486 6.2.1 MLP MODELS  
487

488 In the MLP model, the classification accuracy drops dramatically as the fault ratio increases. This  
489 is because the faulty weights are directly multiplied by the input values, and the pre-activation  
490 magnitude increases significantly, allowing it to easily escape from the surrogate gradient corridor.  
491 Our mechanism definitely outperforms the baseline and benchmarks, since it utilizes the input saliency  
492 and weight projection map of the first layer in Gini-based equal fragmentation. The MLP model is  
493 vulnerable to faults in the first layer, as mentioned in Subsection 4.1. By adopting the saliency and  
494 weight projection map (fault influence map) of the first layer, we suppress its pre-activation, which  
495 decides the surrogate gradient, from increasing significantly and escaping from the corridor. Thus,  
496 the pre-activation does not lie far from the corridor, preserving the power of the first layer’s gradient.  
497

498 6.2.2 VGG MODELS  
499

500 While VGG models with the benchmarks using CIFAR-10 maintain proper classification perfor-  
501 mance only up to a fault ratio of 30–40%, the models with the proposed mechanism sustain correct  
502 classification even at fault ratios as high as 50%. This is because our mechanism targets to make  
503 the pre-activation lie at the point in the surrogate gradient corridor with Gini-based equal mass  
504 fragmentation, despite the large amount of faults. Contrarily, the benchmarks do not consider the  
505 relations between pre-activation, corridor, and surrogate gradient, failing to bound the pre-activation  
506 in the corridor. Therefore, the classification accuracy of the model using the benchmarks degrades  
507 sharply with fewer faults. We also observe that the classification accuracy declines as the model  
508 gets deeper. This occurs because surrogate gradients in deep SNNs cannot reliably approximate the  
509 hypothetical gradients of LIF neurons (Guo et al., 2024). When we use CIFAR-100, the models do  
510 not classify the data samples accurately due to their low learning ability. However, the models with  
our mechanism exhibit the highest classification accuracy under SAFs in most cases.  
511

512 6.2.3 RESNET MODELS  
513

514 Different from VGG models, ResNet models integrated with the benchmarks and proposed mechanism  
515 maintain the classification accuracy up to a fault ratio of 80-90% when we use CIFAR-10. This is  
516 because ResNet models have internal mechanisms to compensate for errors in gradient calculations,  
517 such as residual blocks. They also classify CIFAR-100 samples more accurately than VGG models  
518 under faults, since they have a more powerful learning ability than VGG models. ResNet-18 using  
519 CIFAR-100 maintains its classification ability up to the ratio of 60-70% only with our mechanism,  
520 and the ResNet-34 with CIFAR-100 maintains the classification ability up to the ratio of 30-40% only  
521 with our mechanism. These results demonstrate that our mechanism successfully enhances the fault  
522 tolerance with complicated datasets and models. We observe that the astrocyte-based approaches  
523 (Astrocyte and LIFA) do not improve the deep ResNet models’ fault tolerance at all. This problem  
524 derives from the fact that they only mimic biological mechanisms of neuronal activity in brains,  
525 which enhances the fault tolerance of shallow and highly bio-plausible models such as Diehl & Cook  
2015, using a bio-plausible unsupervised learning rule (Han et al., 2023; Yunusoglu et al., 2025).  
526 However, our mechanism successfully strengthens the models’ fault tolerance in most cases since  
527 we tackle a fundamental problem of faulty SNN models regardless of the types of SNN models, and  
528 develop a solution to mitigate the problem.  
529

530 7 CONCLUSION  
531

532 This paper introduces a simple yet effective fault mitigation mechanism for SNNs that does not require  
533 complicated architectures or direct weight modifications based on input data control. Our mechanism  
534 improves fault tolerance more effectively than conventional approaches in various SNN models  
535 and datasets. Experimental results exhibited improvement in the fault tolerance of our mechanism  
536 over benchmarks in various network models and datasets, including real hardware environments.  
537 We emphasize that this improvement is primarily achieved through an effective input data control  
538 mechanism based on detailed observation of how synaptic faults ruin the learning capability of SNNs.  
539 Our mechanism allows SNNs to maintain reliable operation and high fault tolerance in a practical  
and hardware-compatible manner, enabling more sustainable and reliable edge AI computing.

540 ETHICS STATEMENT  
541

542 This work does not involve human subjects, sensitive personal data, or potentially harmful applications.  
543 We trained and validated our models using publicly available datasets (e.g., MNIST, FMNIST, CIFAR-  
544 10, and CIFAR-100), without any private or identifiable information. We design our mechanism to  
545 enhance the robustness of neuromorphic systems against hardware faults. We declare no conflict of  
546 interest or external sponsorship that might have influenced the research outcomes.  
547

548 REPRODUCIBILITY STATEMENT  
549

550 We conducted all experiments on publicly available datasets with standard train/validation/test  
551 splits. To facilitate replication, we provide our full implementation of the proposed mechanisms  
552 in the anonymous supplementary material. We also present the hyperparameter settings, model  
553 configurations, and hardware specifications to support reproducibility. We will publicly release the  
554 code and scripts on GitHub if our paper is accepted for the conference.  
555

556 LARGE LANGUAGE MODEL USAGE STATEMENT  
557

558 We used Large Language Models (LLMs) as writing and experiment assistants to improve the clarity  
559 of writing/editing mathematical equations (fixing typos/suggesting algebraic simplifications), and  
560 assist us in conducting experiments with the benchmarks. We did not use LLMs for idea generation,  
561 methodological design, analysis, or to originate any mathematical arguments or claims. We derived,  
562 verified, and finalized all derivations, results, and claims.  
563

564 REFERENCES  
565

566 Sarah Ali El Sayed. *Fault Tolerance in Hardware Spiking Neural Networks*. Theses, Sorbonne  
567 Université, October 2021. URL <https://theses.hal.science/tel-03681910>.

568 Arindam Basu, Jyotibdha Acharya, Tanay Karnik, Huichu Liu, Hai Li, Jae-Sun Seo, and Chang Song.  
569 Low-power, adaptive neuromorphic systems: Recent progress and future directions. *IEEE Journal*  
570 *on Emerging and Selected Topics in Circuits and Systems*, 8(1):6–27, 2018. doi: 10.1109/JETCAS.  
571 2018.2816339.  
572

573 Sören Becker, Johanna Vielhaben, Marcel Ackermann, Klaus-Robert Müller, Sebastian Lapuschkin,  
574 and Wojciech Samek. Audiomnist: Exploring explainable artificial intelligence for audio analysis  
575 on a simple benchmark. *Journal of the Franklin Institute*, 361(1):418–428, 2024. ISSN 0016-  
576 0032. doi: 10.1016/j.jfranklin.2023.11.038. URL <https://www.sciencedirect.com/science/article/pii/S0016003223007536>.  
577

578 Fernando Berzal. Dl101 neural network outputs and loss functions, 2025. URL <https://arxiv.org/abs/2511.05131>.  
579

580 Léon Bottou, Frank E. Curtis, and Jorge Nocedal. Optimization methods for large-scale machine  
581 learning, 2018. URL <https://arxiv.org/abs/1606.04838>.  
582

583 Stephen Boyd and Lieven Vandenberghe. *Convex Optimization*. Cambridge University Press,  
584 Cambridge, 2004. doi: 10.1017/CBO9780511804441.  
585

586 BrainChipInc. Akd1000 akida system-on-chip — product brief. Technical Report V2.3, BrainChip-  
587 Inc., 8 2025. URL <https://brainchip.com/wp-content/uploads/2025/08/Akida-AKD1000-SoC-Product-Brief-V2.3-Aug.25.pdf>. Accessed 2025-09-07.  
588

589 Alessio Carpegna, Alessandro Savino, and Stefano Di Carlo. Spiker+: a framework for the generation  
590 of efficient spiking neural networks fpga accelerators for inference at the edge. *IEEE Transactions*  
591 *on Emerging Topics in Computing*, pp. 1–15, 2024. doi: 10.1109/TETC.2024.3511676.  
592

594 Kaiwei Che, Liziwei Leng, Kaixuan Zhang, Jianguo Zhang, Max Q.-H. Meng, Jie Cheng, Qinghai  
 595 Guo, and Jiangxing Liao. Differentiable hierarchical and surrogate gradient search for spik-  
 596 ing neural networks. In *Proceedings of the 36th International Conference on Neural Infor-  
 597 mation Processing Systems*, NIPS '22, Red Hook, NY, USA, 2022. Curran Associates Inc. ISBN  
 598 9781713871088.

599 Ching-Yuan Chen and Krishnendu Chakrabarty. Pruning of deep neural networks for fault-tolerant  
 600 memristor-based accelerators. In *2021 58th ACM/IEEE Design Automation Conference (DAC)*,  
 601 pp. 889–894. IEEE Press, 2021. doi: 10.1109/DAC18074.2021.9586269. URL <https://doi.org/10.1109/DAC18074.2021.9586269>.

602 Lerong Chen, Jiawen Li, Yiran Chen, Qiuping Deng, Jiyuan Shen, Xiaoyao Liang, and Li Jiang.  
 603 Accelerator-friendly neural-network training: Learning variations and defects in rram crossbar. In  
 604 *Design, Automation & Test in Europe Conference & Exhibition (DATE)*, 2017, pp. 19–24, 2017.  
 605 doi: 10.23919/DATE.2017.7926952.

606 Benjamin Cramer, Sebastian Billaudelle, Simeon Kanya, Aron Leibfried, Andreas Grübl, Vi-  
 607 tali Karasenko, Christian Pehle, Korbinian Schreiber, Yannik Stradmann, Johannes Weis, Jo-  
 608 hannes Schemmel, and Friedemann Zenke. Surrogate gradients for analog neuromorphic com-  
 609 puting. *Proceedings of the National Academy of Sciences*, 119(4):e2109194119, 2022. doi:  
 610 10.1073/pnas.2109194119. URL <https://www.pnas.org/doi/abs/10.1073/pnas.2109194119>.

611 Jia Deng, Wei Dong, Richard Socher, Li-Jia Li, Kai Li, and Li Fei-Fei. Tiny ImageNet challenge.  
 612 <http://cs231n.stanford.edu/tiny-imagenet-200.zip>, 2015. Stanford CS231n  
 613 course dataset. Accessed: 2025-11-12.

614 Peter Diehl and Matthew Cook. Unsupervised learning of digit recognition using spike-timing-  
 615 dependent plasticity. *Frontiers in Computational Neuroscience*, 9, 2015. doi: 10.3389/fncom.2015.  
 616 00099. URL <https://www.frontiersin.org/article/10.3389/fncom.2015.00099>.

617 M. Reza Eslami, Dhiman Biswas, Soheib Takhtardeshir, Sarah S. Sharif, and Yaser M. Banad. On-  
 618 chip learning with memristor-based neural networks: Assessing accuracy and efficiency under  
 619 device variations, conductance errors, and input noise, 2024. URL <https://arxiv.org/abs/2408.14680>.

620 Wei Fang, Yanqi Chen, Jianhao Ding, Zhaofei Yu, Timothée Masquelier, Ding Chen, Liwei Huang,  
 621 Huihui Zhou, Guoqi Li, and Yonghong Tian. Spikingjelly: An open-source machine learning  
 622 infrastructure platform for spike-based intelligence. *Science Advances*, 9(40):eadi1480, 2023.  
 623 doi: 10.1126/sciadv.ad1480. URL <https://www.science.org/doi/abs/10.1126/sciadv.ad1480>.

624 Frank A. Farris. The gini index and measures of inequality. *The American Mathematical Monthly*,  
 625 117(10):pp. 851–864, 2010. ISSN 00029890, 19300972. URL <https://www.jstor.org/stable/10.4169/000298910x523344>.

626 Pierre Foret, Ariel Kleiner, Hossein Mobahi, and Behnam Neyshabur. Sharpness-aware minimiza-  
 627 tion for efficiently improving generalization, 2021. URL <https://arxiv.org/abs/2010.01412>.

628 Luíza C. Garaffa, Abdullah Aljuffri, Cezar Reinbrecht, Said Hamdioui, Mottaqiallah Taouil, and  
 629 Johanna Sepulveda. Revealing the secrets of spiking neural networks: The case of izhikevich  
 630 neuron. In *2021 24th Euromicro Conference on Digital System Design (DSD)*, pp. 514–518, 2021.  
 631 doi: 10.1109/DSD53832.2021.00083.

632 Yufei Guo, Yuanpei Chen, Zecheng Hao, Weihang Peng, Zhou Jie, Yuhang Zhang, Xiaode Liu, and Zhe  
 633 Ma. Take a shortcut back: Mitigating the gradient vanishing for training spiking neural networks.  
 634 In A. Globerson, L. Mackey, D. Belgrave, A. Fan, U. Paquet, J. Tomczak, and C. Zhang (eds.),  
 635 *Advances in Neural Information Processing Systems*, volume 37, pp. 24849–24867. Curran Asso-  
 636 ciates, Inc., 2024. URL [https://proceedings.neurips.cc/paper\\_files/paper/2024/file/2c37c5bcef24b9541550261dcd63261b-Paper-Conference.pdf](https://proceedings.neurips.cc/paper_files/paper/2024/file/2c37c5bcef24b9541550261dcd63261b-Paper-Conference.pdf).

648 Zhuangyu Han, A N M Nafiu Islam, and Abhranil Sengupta. Astromorphic self-repair of neuro-  
 649 morphic hardware systems. *Proceedings of the AAAI Conference on Artificial Intelligence*, 37  
 650 (6):7821–7829, Jun. 2023. doi: 10.1609/aaai.v37i6.25947. URL <https://ojs.aaai.org/index.php/AAAI/article/view/25947>.  
 651

652 Hananel Hazan, Daniel J. Saunders, Hassaan Khan, Devdhar Patel, Darpan T. Sanghavi, Hava T.  
 653 Siegelmann, and Robert Kozma. Bindsnet: A machine learning-oriented spiking neural networks  
 654 library in python. *Frontiers in Neuroinformatics*, 12, 2018. doi: 10.3389/fninf.2018.00089. URL  
 655 <https://www.frontiersin.org/article/10.3389/fninf.2018.00089>.  
 656

657 Wassily Hoeffding. Probability inequalities for sums of bounded random variables. *Journal of the  
 658 American Statistical Association*, 58(301):13–30, 1963. doi: 10.1080/01621459.1963.10500830.  
 659

660 Hakcheon Jeong, Seungjae Han, See-On Park, Tae Ryong Kim, Jongmin Bae, Taehwan Jang, Yoonho  
 661 Cho, Seokho Seo, Hyun-Jun Jeong, Seungwoo Park, Taehoon Park, Juyoung Oh, Jeongwoo Park,  
 662 Kwangwon Koh, Kang-Ho Kim, Dongsuk Jeon, Inyong Kwon, Young-Gyu Yoon, and Shinyun  
 663 Choi. Self-supervised video processing with self-calibration on an analogue computing platform  
 664 based on a selector-less memristor array. *Nature Electronics*, Jan 2025. ISSN 2520-1131. doi: 10.  
 665 1038/s41928-024-01318-6. URL <https://doi.org/10.1038/s41928-024-01318-6>.  
 666

666 Mehrzad Karamimanesh, Ebrahim Abiri, Mahyar Shahsavari, Kourosh Hassani, André van Schaik,  
 667 and Jason Eshraghian. Spiking neural networks on fpga: A survey of methodologies and recent  
 668 advancements. *Neural Networks*, 186:107256, 2025. ISSN 0893-6080. doi: <https://doi.org/10.1016/j.neunet.2025.107256>. URL <https://www.sciencedirect.com/science/article/pii/S0893608025001352>.  
 669

670 Hamed Karimi, Julie Nutini, and Mark Schmidt. Linear convergence of gradient and proximal-  
 671 gradient methods under the polyak-łojasiewicz condition, 2020. URL <https://arxiv.org/abs/1608.04636>.  
 672

673 Asif Ali Khan, João Paulo C. De Lima, Hamid Farzaneh, and Jeronimo Castrillon. The landscape  
 674 of compute-near-memory and compute-in-memory: A research and commercial overview, 2024.  
 675 URL <https://arxiv.org/abs/2401.14428>.  
 676

677 Alex Krizhevsky. Learning multiple layers of features from tiny images. Technical report,  
 678 University of Toronto, 2009. URL <https://www.cs.toronto.edu/~kriz/learning-features-2009-TR.pdf>.  
 679

680 James F. Kurose and Keith W. Ross. *Computer Networking: A Top-Down Approach (6th Edition)*.  
 681 Pearson, 6th edition, 2012. ISBN 0132856204.  
 682

683 Xavier Lagorce, Evangelos Stromatias, Francesco Galluppi, Luis A. Plana, Shih-Chii Liu,  
 684 Steve B. Furber, and Ryad B. Benosman. Breaking the millisecond barrier on spinnaker:  
 685 implementing asynchronous event-based plastic models with microsecond resolution. *Frontiers in  
 686 Neuroscience*, Volume 9 - 2015, 2015. ISSN 1662-453X. doi: 10.3389/fnins.2015.00206. URL  
 687 <https://www.frontiersin.org/journals/neuroscience/articles/10.3389/fnins.2015.00206>.  
 688

689 Corey Lammie, Wei Xiang, Bernabé Linares-Barranco, and Mostafa Rahimi Azghadi. Mem-  
 690 torch: An open-source simulation framework for memristive deep learning systems. *Neu-  
 691 rocomputing*, 485:124–133, 2022. ISSN 0925-2312. doi: <https://doi.org/10.1016/j.neucom.2022.02.043>. URL <https://www.sciencedirect.com/science/article/pii/S0925231222002053>.  
 692

693 Manuel Le Gallo, Corey Lammie, Julian Büchel, Fabio Carta, Omobayode Fagbohungbe, Charles  
 694 Mackin, Hsinyu Tsai, Vijay Narayanan, Abu Sebastian, Kaoutar El Maghraoui, and Malte J.  
 695 Rasch. Using the ibm analog in-memory hardware acceleration kit for neural network training  
 696 and inference. *APL Machine Learning*, 1(4), November 2023. ISSN 2770-9019. doi: 10.1063/5.  
 697 0168089. URL <http://dx.doi.org/10.1063/5.0168089>.  
 698

699 Yann LeCun, Léon Bottou, Yoshua Bengio, and Patrick Haffner. Gradient-based learning applied to  
 700 document recognition. *Proceedings of the IEEE*, 86(11):2278–2324, 1998. doi: 10.1109/5.726791.  
 701

702 Hyun-Jong Lee and Jae-Han Lim. Analysis on effects of fault elements in memristive neuromorphic  
 703 systems. In *IJCAI 2023 GLOW workshop*, 2023. URL <https://arxiv.org/abs/2312.04840>.

704

705 Hyun-Jong Lee and Jae-Han Lim. Adaptive synaptic adjustment mechanism to improve learning  
 706 performances of spiking neural networks. *Computational Intelligence*, 40(5):e70001, 2024. doi:  
 707 <https://doi.org/10.1111/coin.70001>. URL <https://onlinelibrary.wiley.com/doi/abs/10.1111/coin.70001>.

708

709 Yudong Li, Yunlin Lei, and Xu Yang. Spikeformer: Training high-performance spiking neural network  
 710 with transformer. *Neurocomputing*, 574:127279, 2024a. ISSN 0925-2312. doi: <https://doi.org/10.1016/j.neucom.2024.127279>. URL <https://www.sciencedirect.com/science/article/pii/S092523122400050X>.

711

712 Yuhang Li, Tamar Geller, Youngeun Kim, and Priyadarshini Panda. Seenn: towards temporal  
 713 spiking early-exit neural networks. In *Proceedings of the 37th International Conference on Neural  
 714 Information Processing Systems*, NIPS '23, Red Hook, NY, USA, 2024b. Curran Associates Inc.

715

716 Shuang Lian, Jiangrong Shen, Qianhui Liu, Ziming Wang, Rui Yan, and Huajin Tang. Learnable  
 717 surrogate gradient for direct training spiking neural networks. In Edith Elkind (ed.), *Proceedings  
 718 of the Thirty-Second International Joint Conference on Artificial Intelligence, IJCAI-23*, pp.  
 719 3002–3010. International Joint Conferences on Artificial Intelligence Organization, 8 2023. doi:  
 720 <https://doi.org/10.24963/ijcai.2023/335>. URL <https://doi.org/10.24963/ijcai.2023/335>. Main  
 721 Track.

722

723 Ling Liang, Xing Hu, Lei Deng, Yujie Wu, Guoqi Li, Yufei Ding, Peng Li, and Yuan Xie. Exploring  
 724 adversarial attack in spiking neural networks with spike-compatible gradient. *IEEE Transactions  
 725 on Neural Networks and Learning Systems*, 34(5):2569–2583, 2023. doi: 10.1109/TNNLS.2021.  
 726 3106961.

727

728 Tao Liu, Wujie Wen, Lei Jiang, Yanzhi Wang, Chengmo Yang, and Gang Quan. A fault-tolerant  
 729 neural network architecture. In *2019 56th ACM/IEEE Design Automation Conference (DAC)*, pp.  
 730 1–6, 2019.

731

732 Tongliang Liu, Gábor Lugosi, Gergely Neu, and Dacheng Tao. Algorithmic stability and hypothesis  
 733 complexity, 2017. URL <https://arxiv.org/abs/1702.08712>.

734

735 David G. Lowe. Distinctive image features from scale-invariant keypoints. *International Journal of  
 736 Computer Vision*, 60(2):91–110, Nov 2004. ISSN 1573-1405. doi: 10.1023/B:VISI.0000029664.  
 99615.94. URL <https://doi.org/10.1023/B:VISI.0000029664.99615.94>.

737

738 M. Martemucci, F. Rummens, Y. Malot, et al. A ferroelectric–memristor memory for both training  
 739 and inference. *Nature Electronics*, 8:921–933, 2025. doi: 10.1038/s41928-025-01454-7.

740

741 Abhishek Moitra, Abhiroop Bhattacharjee, Runcong Kuang, Gokul Krishnan, Yu Cao, and  
 742 Priyadarshini Panda. Spikesim: An end-to-end compute-in-memory hardware evaluation tool  
 743 for benchmarking spiking neural networks. *IEEE Transactions on Computer-Aided Design of  
 744 Integrated Circuits and Systems*, 42(11):3815–3828, 2023. doi: 10.1109/TCAD.2023.3274918.

745

746 Emre O. Neftci, Hesham Mostafa, and Friedemann Zenke. Surrogate gradient learning in spiking  
 747 neural networks: Bringing the power of gradient-based optimization to spiking neural networks.  
 748 *IEEE Signal Processing Magazine*, 36(6):51–63, 2019. doi: 10.1109/MSP.2019.2931595.

749

750 Yurii Nesterov. *Introductory Lectures on Convex Optimization: A Basic Course*. Springer Publishing  
 751 Company, Incorporated, 1 edition, 2014. ISBN 1461346916.

752

753 Sathish Panchapakesan, Zhenman Fang, and Jian Li. Syncenn: Evaluating and accelerating spiking  
 754 neural networks on fpgas. In *2021 31st International Conference on Field-Programmable Logic  
 755 and Applications (FPL)*, pp. 286–293, 2021. doi: 10.1109/FPL53798.2021.00058.

756

757 Melika Payvand, Mohammed E. Fouda, Fadi Kurdahi, Ahmed M. Eltawil, and Emre O. Neftci.  
 758 On-chip error-triggered learning of multi-layer memristive spiking neural networks. *IEEE Journal  
 759 on Emerging and Selected Topics in Circuits and Systems*, 10(4):522–535, 2020. doi: 10.1109/  
 760 JETCAS.2020.3040248.

756 Vitali Petsiuk, Abir Das, and Kate Saenko. Rise: Randomized input sampling for explanation of  
 757 black-box models, 2018. URL <https://arxiv.org/abs/1806.07421>.

758

759 Michael Pfeiffer and Thomas Pfeil. Deep learning with spiking neurons: Opportunities and  
 760 challenges. *Frontiers in Neuroscience*, 12, 2018. ISSN 1662-453X. doi: 10.3389/fnins.  
 761 2018.00774. URL <https://www.frontiersin.org/journals/neuroscience/articles/10.3389/fnins.2018.00774>.

762

763 Rachmad Vidya Wicaksana Putra, Muhammad Abdullah Hanif, and Muhammad Shafique. Softsnn:  
 764 low-cost fault tolerance for spiking neural network accelerators under soft errors. In *Proceedings  
 765 of the 59th ACM/IEEE Design Automation Conference*, DAC '22, pp. 151–156, New York, NY,  
 766 USA, 2022. Association for Computing Machinery. ISBN 9781450391429. doi: 10.1145/3489517.  
 767 3530657. URL <https://doi.org/10.1145/3489517.3530657>.

768

769 Rachmad Vidya Wicaksana Putra, Muhammad Abdullah Hanif, and Muhammad Shafique. Res-  
 770 cuesnn: enabling reliable executions on spiking neural network accelerators under perma-  
 771 nent faults. *Frontiers in Neuroscience*, 17, 2023. ISSN 1662-453X. doi: 10.3389/fnins.  
 772 2023.1159440. URL <https://www.frontiersin.org/journals/neuroscience/articles/10.3389/fnins.2023.1159440>.

773

774 Zexuan Qiu, Zijing Ou, Bin Wu, Jingjing Li, Aiwei Liu, and Irwin King. Entropy-based decod-  
 775 ing for retrieval-augmented large language models. In *Proceedings of the 2025 Conference of  
 776 the North American Chapter of the Association for Computational Linguistics (NAACL), Long  
 777 Papers*, pp. 4616–4627, Albuquerque, New Mexico, 2025. Association for Computational Linguis-  
 778 tics. doi: 10.18653/v1/2025.naacl-long.236. URL [https://aclanthology.org/2025.naacl-long.236/](https://aclanthology.org/2025.naacl-long.236).

779

780 Mehul Rastogi, Sen Lu, Nafiu Islam, and Abhroni Sengupta. On the self-repair role of astrocytes  
 781 in stdp enabled unsupervised snns. *Frontiers in Neuroscience*, Volume 14 - 2020, 2021. ISSN  
 782 1662-453X. doi: 10.3389/fnins.2020.603796. URL <https://www.frontiersin.org/journals/neuroscience/articles/10.3389/fnins.2020.603796>.

783

784 Alpha Renner, Forrest Sheldon, Anatoly Zlotnik, Louis Tao, and Andrew Sornborger. The backpropa-  
 785 gation algorithm implemented on spiking neuromorphic hardware. *Nature Communications*, 15(1):  
 786 9691, 2024. doi: 10.1038/s41467-024-53827-9.

787

788 Reyes-Ortiz, Jorge, Anguita, Davide, Ghio, Alessandro, Oneto, Luca, Parra, and Xavier. Hu-  
 789 man activity recognition using smartphones. UCI Machine Learning Repository, 2013. DOI:  
 790 <https://doi.org/10.24432/C54S4K>.

791

792 Amirhossein Rostami, Bernhard Vogginger, Yexin Yan, and Christian G. Mayr. E-prop on  
 793 spinnaker 2: Exploring online learning in spiking rnns on neuromorphic hardware. *Front-  
 794 iers in Neuroscience*, Volume 16 - 2022, 2022. ISSN 1662-453X. doi: 10.3389/fnins.  
 795 2022.1018006. URL <https://www.frontiersin.org/journals/neuroscience/articles/10.3389/fnins.2022.1018006>.

796

797 Anurup Saha, Chandramouli Amarnath, and Abhijit Chatterjee. A resilience framework for synapse  
 798 weight errors and firing threshold perturbations in rram spiking neural networks. In *2023 IEEE  
 799 European Test Symposium (ETS)*, pp. 1–4, 2023. doi: 10.1109/ETS56758.2023.10174229.

800

801 Anurup Saha, Chandramouli Amarnath, Kwondo Ma, and Abhijit Chatterjee. Signature driven  
 802 post-manufacture testing and tuning of rram spiking neural networks for yield recovery. In *2024  
 803 29th Asia and South Pacific Design Automation Conference (ASP-DAC)*, pp. 740–745, 2024. doi:  
 804 10.1109/ASP-DAC58780.2024.10473874.

805

806 Jozsef Sandor. The Schur-convexity of Stolarsky and Gini means. *Banach Journal of Mathematical  
 807 Analysis*, 1(2):212 – 215, 2007. doi: 10.15352/bjma/1240336218. URL <https://doi.org/10.15352/bjma/1240336218>.

808

809 Catherine D. Schuman, Shruti R. Kulkarni, Maryam Parsa, J. Parker Mitchell, Prasanna Date,  
 810 and Bill Kay. Opportunities for neuromorphic computing algorithms and applications. *Nature  
 811 Computational Science*, 2(1):10–19, Jan 2022. doi: 10.1038/s43588-021-00184-y. URL <https://doi.org/10.1038/s43588-021-00184-y>.

810     Sumit Bam Shrestha and Garrick Orchard. Slayer: Spike layer error reassignment in time, 2018.  
 811     URL <https://arxiv.org/abs/1810.08646>.  
 812

813     Ayesha Siddique and Khaza Anuarul Hoque. Improving reliability of spiking neural networks through  
 814     fault aware threshold voltage optimization, 2023. URL <https://arxiv.org/abs/2301.05266>.  
 815

816     Steven S. Skiena. *The Algorithm Design Manual*. Springer, 2 edition, 2008. doi: 10.1007/978-1-84800-070-4.  
 817

818     Theofilos Spyrou, Sarah A. El-Sayed, Engin Afacan, Luis A. Camuñas-Mesa, Bernabé Linares-  
 819     Barranco, and Haralampos-G. Stratigopoulos. Neuron fault tolerance in spiking neural networks.  
 820     In *2021 Design, Automation & Test in Europe Conference & Exhibition (DATE)*, pp. 743–748,  
 821     2021. doi: 10.23919/DATE51398.2021.9474081.  
 822

823     Kenneth Stewart, Garrick Orchard, Sumit Bam Shrestha, and Emre Neftci. Live demonstration:  
 824     On-chip few-shot learning with surrogate gradient descent on a neuromorphic processor. In *2020*  
 825     *2nd IEEE International Conference on Artificial Intelligence Circuits and Systems (AICAS)*, pp.  
 826     128–128, 2020. doi: 10.1109/AICAS48895.2020.9073961.  
 827

828     Shigeyuki Takano and Hideharu Amano. Reconfiguration cost for reconfigurable computing archi-  
 829     tec tures. In *2022 23rd ACIS International Summer Virtual Conference on Software Engineering,*  
 830     *Artificial Intelligence, Networking and Parallel/Distributed Computing (SNPD-Summer)*, pp. 62–  
 831     67, 2022. doi: 10.1109/SNPD-Summer57817.2022.00019.  
 832

833     Yudong Tao, Rui Ma, Mei-Ling Shyu, and Shu-Ching Chen. Challenges in energy-efficient deep  
 834     neural network training with FPGA. In *Proceedings of the 2020 IEEE/CVF Conference on*  
 835     *Computer Vision and Pattern Recognition Workshops (CVPRW)*, pp. 1602–1611. Computer Vision  
 836     Foundation / IEEE, 2020. ISBN 978-1-7281-9360-1. doi: 10.1109/CVPRW50498.2020.00208.  
 837     URL [https://openaccess.thecvf.com/content\\_CVPRW\\_2020/html/w28/Tao\\_Challenges\\_in\\_Energy-Efficient\\_Deep\\_Neural\\_Network\\_Training\\_with\\_FPGA\\_CVPRW\\_2020\\_paper.html](https://openaccess.thecvf.com/content_CVPRW_2020/html/w28/Tao_Challenges_in_Energy-Efficient_Deep_Neural_Network_Training_with_FPGA_CVPRW_2020_paper.html).  
 838

839     M. L. Varshika, Sarah Johari, Jayanth Dubey, and Anup Das. Design of a tunable astrocyte neuromor-  
 840     phic circuitry with adaptable fault tolerance. In *2023 IEEE 66th International Midwest Symposium*  
 841     *on Circuits and Systems (MWSCAS)*, pp. 904–908, 2023. doi: 10.1109/MWSCAS57524.2023.  
 842     10405978.  
 843

844     Elena-Ioana Vatajelu, Giorgio Di Natale, and Lorena Anghel. Special session: Reliability of hardware-  
 845     implemented spiking neural networks (snn). In *2019 IEEE 37th VLSI Test Symposium (VTS)*, pp.  
 846     1–8, 2019. doi: 10.1109/VTS.2019.8758653.  
 847

848     Yeshwanth Venkatesha, Youngeun Kim, Leandros Tassiulas, and Priyadarshini Panda. Federated  
 849     learning with spiking neural networks. *IEEE Transactions on Signal Processing*, 69:6183–6194,  
 850     2021. doi: 10.1109/TSP.2021.3121632.  
 851

852     The H. Vu, Ogbodo Mark Ikechukwu, and Abderazek Ben Abdallah. Fault-tolerant spike routing  
 853     algorithm and architecture for three dimensional noc-based neuromorphic systems. *IEEE Access*,  
 854     7:90436–90452, 2019. doi: 10.1109/ACCESS.2019.2925085.  
 855

856     Ziming Wang, Runhao Jiang, Shuang Lian, Rui Yan, and Huajin Tang. Adaptive smoothing gradient  
 857     learning for spiking neural networks. In Andreas Krause, Emma Brunskill, Kyunghyun Cho, Bar-  
 858     bara Engelhardt, Sivan Sabato, and Jonathan Scarlett (eds.), *Proceedings of the 40th International*  
 859     *Conference on Machine Learning*, volume 202 of *Proceedings of Machine Learning Research*, pp.  
 860     35798–35816. PMLR, 23–29 Jul 2023. URL <https://proceedings.mlr.press/v202/wang23j.html>.  
 861

862     Rachmad Vidya Wicaksana Putra, Muhammad Abdullah Hanif, and Muhammad Shafique. Respawn:  
 863     Energy-efficient fault-tolerance for spiking neural networks considering unreliable memories. In  
 864     *2021 IEEE/ACM International Conference On Computer Aided Design (ICCAD)*, pp. 1–9, 2021.  
 865     doi: 10.1109/ICCAD51958.2021.9643524.

864 Torbjörn Wigren and Reem Karaki. Globally stable wireless data flow control. *IEEE Transactions on*  
 865 *Control of Network Systems*, 5(1):469–478, 2018. doi: 10.1109/TCNS.2016.2619906.

866

867 Han Xiao, Kashif Rasul, and Roland Vollgraf. Fashion-MNIST: A novel image dataset for  
 868 benchmarking machine learning algorithms. *arXiv preprint arXiv:1708.07747*, 2017. URL  
 869 <https://arxiv.org/abs/1708.07747>.

870

871 Shuangming Yang, Jiang Wang, Bin Deng, Mostafa Rahimi Azghadi, and Bernabe Linares-Barranco.  
 872 Neuromorphic context-dependent learning framework with fault-tolerant spike routing. *IEEE*  
 873 *Transactions on Neural Networks and Learning Systems*, 33(12):7126–7140, 2022. doi: 10.1109/  
 874 TNNLS.2021.3084250.

875

876 Man Yao, Guangshe Zhao, Hengyu Zhang, Yifan Hu, Lei Deng, Yonghong Tian, Bo Xu, and Guoqi  
 877 Li. Attention spiking neural networks. *IEEE Transactions on Pattern Analysis and Machine*  
 878 *Intelligence*, 45(8):9393–9410, 2023. doi: 10.1109/TPAMI.2023.3241201.

879

880 Mingqi Yin, Xiaole Cui, Feng Wei, Hanqing Liu, Yuanyuan Jiang, and Xiaoxin Cui. A re-  
 881 configurable fpga-based spiking neural network accelerator. *Microelectronics Journal*, 152:  
 882 106377, 2024. ISSN 1879-2391. doi: <https://doi.org/10.1016/j.mejo.2024.106377>. URL <https://www.sciencedirect.com/science/article/pii/S187923912400081X>.

883

884 Shlomo Yitzhaki and Edna Schechtman. *The Gini Methodology: A Primer on a Statistical Method-  
 885 ology*. Springer Series in Statistics. Springer, New York, 2013. ISBN 978-1-4614-4719-1. doi:  
 886 10.1007/978-1-4614-4720-7.

887

888 Anlan Yu, Ning Lyu, Jieming Yin, Zhiyuan Yan, and Wujie Wen. COLA: Orchestrating error coding  
 889 and learning for robust neural network inference against hardware defects. In Andreas Krause,  
 890 Emma Brunskill, Kyunghyun Cho, Barbara Engelhardt, Sivan Sabato, and Jonathan Scarlett  
 891 (eds.), *Proceedings of the 40th International Conference on Machine Learning*, volume 202 of  
 892 *Proceedings of Machine Learning Research*, pp. 40277–40289. PMLR, 23–29 Jul 2023. URL  
 893 <https://proceedings.mlr.press/v202/yu23a.html>.

894

895 Aybars Yunusoglu, Dexter Le, Murat Isik, I. Can Dikmen, and Teoman Karadag. Neuromorphic  
 896 circuits with spiking astrocytes for increased energy efficiency, fault tolerance, and memory  
 897 capacitance, 2025. URL <https://arxiv.org/abs/2502.20492>.

898

899 Friedemann Zenke and Tim P. Vogels. The remarkable robustness of surrogate gradient learning for  
 900 instilling complex function in spiking neural networks. *Neural Computation*, 33(4):899–925, 03  
 901 2021. ISSN 0899-7667. doi: 10.1162/neco\_a\_01367. URL [https://doi.org/10.1162/neco\\_a\\_01367](https://doi.org/10.1162/neco_a_01367).

902

903 Biao Zhang and Rico Sennrich. Root mean square layer normalization. In *Advances in Neural Infor-  
 904 mation Processing Systems 32 (NeurIPS 2019)*, pp. 12360–12371, 2019. URL <https://papers.nips.cc/paper/2019/file/1e8a19426224ca89e83cef47f1e7f53b-Paper.pdf>.

905

906

907

908

909

910

911

912

913

914

915

916

917

918 APPENDIX INDEX  
919920 **Appendix A** Discussion  
921922     **A** Discussion923 **Appendix B** Additional experimental results on classification accuracy924     **B.1** Additional datasets beyond MNIST, FMNIST, CIFAR-10, and CIFAR-100925         **B.1.1** Sequential dataset926         **B.1.2** Large image dataset927     **B.2** Changing the number of time steps928         **B.2.1** 4 time steps929         **B.2.2** 8 time steps930     **B.3** Under the different types of synaptic faults931         **B.3.1** RWFs932         **B.3.2** CEFs933     **B.4** Ablation study on the combination of our mechanism934         **B.4.1** MLP model (MNIST, FMNIST)935         **B.4.2** VGG-7 and ResNet-18 models (CIFAR-10 and CIFAR-100)936     **B.5** Various hyperparameter settings with our mechanism937         **B.5.1** MLP model (MNIST and FMNIST)938         **B.5.2** VGG-7 and ResNet-18 models (CIFAR-10 and CIFAR-100)939     **B.6** Using Deep Neural Networks (DNNs)940     **B.7** Using SNNs with unsupervised learning941     **B.8** Evaluations with real FPGA hardware942 **Appendix C** Efficiency analysis based on time/spatial complexity and time/energy consumption943     **C.1** Complexity analysis944         **C.1.1** Time complexity945         **C.1.2** Spatial complexity946     **C.2** Training time947     **C.3** Energy consumption on the real FPGA device948 **Appendix D** Detailed mathematical explanation of the motivation study949     **D.1** Setup and notation950     **D.2** Surrogate gradient corridor951     **D.3** Fault modeling952     **D.4** From faults to saturation953     **D.5** Expected gradient bound for a single neuron954     **D.6** Depth- and time-wise compounding955     **D.7** First-layer sensitivity in MLP956     **D.8** Sufficient condition for gradient collapse957     **D.9** Effective bias interpretation for SA0/SA1 of SAFs958     **D.10** Summary959 **Appendix E** Near-optimality of the proposed mechanism960     **E.1** Setup and notation961     **E.2** Fault models and a basic upper bound962     **E.3** Calibration: aligning the importance map with the effective per-index load963     **E.4** Quantile stripes are additively near-optimal (contiguous case)964     **E.5** Corridor preservation: sufficient conditions965     **E.6** On the Gini objective (primary surrogate for min–max load)966     **E.7** Computing the scan-stripes967     **E.8** Summary

972     **Appendix F** Fault-tolerance capacity prediction of our mechanism  
973

974       **F.1** Setup and notation

975       **F.2** Capacity under SAFs

976       **F.3** Capacity under RWFs

977       **F.4** Capacity under CEFs

978       **F.5** Summary

979     **Appendix G** Convergence analysis with the proposed mechanism

980       **G.1** Setup and notation

981       **G.2** Band condition enforced by our mechanism

982       **G.3** Optimization objective and assumptions

983       **G.4** Descent lemma and master inequality

984       **G.5** Summary

985

986

987

988

989

990

991

992

993

994

995

996

997

998

999

1000

1001

1002

1003

1004

1005

1006

1007

1008

1009

1010

1011

1012

1013

1014

1015

1016

1017

1018

1019

1020

1021

1022

1023

1024

1025

## 1026 A DISCUSSION

1028 In this section, we discuss the pros and cons of the proposed mechanism and the lightweight  
 1029 approaches mentioned in Subsection 3.2 (Saha et al., 2023; Spyrou et al., 2021; Saha et al., 2024).  
 1030 Furthermore, we demonstrate that our mechanism exhibits stronger fault mitigation ability than the  
 1031 lightweight approaches, consuming less overhead than the other approaches. Existing lightweight  
 1032 mechanisms for hardware SNN fault mitigation rely on continuously monitoring internal neuron  
 1033 currents or spike statistics and mitigating the adversarial effects of hardware defects (Spyrou et al.,  
 1034 2021; Saha et al., 2023). These designs are acceptable and lightweight for neuromorphic devices that  
 1035 frequently perform inferences due to their simple operations. However, their computational overhead  
 1036 significantly increases in large SNN models. This is because scanning all weights or neuron states  
 1037 and aggregating their statistics grows exponentially as the model’s size increases. Furthermore, they  
 1038 inevitably discard fault-affected pre-activation values, which causes information loss. In contrast, our  
 1039 mechanism avoids direct inspection of entire elements in SNN models or modification of synaptic  
 1040 weights or circuits in hardware. Instead, it computes a sensitivity score from the input samples and a  
 1041 single reference layer for fragmentation. Therefore, the external controller only needs to exchange  
 1042 a small amount of metadata with the neuromorphic device instead of full weight or neuron maps  
 1043 (Khan et al., 2024). When it comes to test-based schemes, they amortize their cost by running only  
 1044 intermittently (Spyrou et al., 2021; Saha et al., 2024). However, they cannot react to permanent faults  
 1045 that arise during deployment. On the other hand, our mechanism always executes during training  
 1046 and inference, incurs modest per-execution overhead, and can immediately adapt the fragmentation  
 1047 strategy to the current fault state in agile environments. Overall, the proposed mechanism provides  
 1048 the following complementary points in the design space. First, it scales better than forward-pass  
 1049 approaches with scanning to large hardware-implemented SNNs, which are important for modern  
 1050 neuromorphic devices (Yin et al., 2024). Second, it trades higher continuous overhead than periodic  
 1051 self-test approaches, achieving substantially stronger mitigation of permanent faults. We compare the  
 1052 accuracy and inference time of the proposed mechanism to that of other representative lightweight  
 1053 mechanisms: input suppression, fault hopping, and threshold tuning (Saha et al., 2023; Spyrou et al.,  
 1054 2021; Saha et al., 2024).

1054 **Table 4:** The SNN model’s classification accuracy and summation of inference time over 100 repetitions in a  
 1055 95% confidence interval with other lightweight approaches and our mechanism under the 30% fault ratio of  
 1056 SAFs.

DATASETS (MODELS)	INPUT SUPPRESSION	FAULT HOPPING	THRESHOLD TUNING	PROPOSED
ACCURACY (%) IN SOFTWARE-BASED SNN MODELS				
MNIST (MLP)	$88.38 \pm 1.15$	$86.41 \pm 0.98$	$87.23 \pm 1.52$	<b><math>93.79 \pm 1.06</math></b>
FMNIST (MLP)	$80.45 \pm 1.22$	$79.86 \pm 1.16$	$78.98 \pm 1.39$	<b><math>85.47 \pm 0.92</math></b>
CIFAR-10 (VGG-7)	$34.67 \pm 3.21$	$30.28 \pm 3.34$	$27.91 \pm 3.26$	<b><math>45.94 \pm 3.17</math></b>
ACCURACY (%) IN FPGA-IMPLEMENTED SNN MODELS				
MNIST (MLP)	$86.7 \pm 1.32$	$84.28 \pm 1.28$	$85.87 \pm 1.65$	<b><math>91.43 \pm 1.17</math></b>
FMNIST (MLP)	$78.46 \pm 0.98$	$75.39 \pm 1.14$	$73.63 \pm 1.27$	<b><math>84.05 \pm 1.09</math></b>
CIFAR-10 (VGG-7)	$31.94 \pm 3.8$	$27.14 \pm 3.72$	$24.75 \pm 2.87$	<b><math>38.11 \pm 3.58</math></b>
INFERENCE TIME (SEC) IN FPGA-IMPLEMENTED SNN MODELS				
MNIST (MLP)	$283.64 \pm 4.85$	$254.43 \pm 2.1$	$213.67 \pm 2.38$	<b><math>191.28 \pm 1.25</math></b>
FMNIST (MLP)	$285.27 \pm 5.17$	$255.79 \pm 1.98$	$215.09 \pm 2.51$	<b><math>193.54 \pm 1.62</math></b>
CIFAR-10 (VGG-7)	$500.59 \pm 7.34$	$327.11 \pm 3.83$	$292.41 \pm 4.86$	<b><math>277.09 \pm 3.47</math></b>
INFERENCE TIME (SEC) IN FPGA-IMPLEMENTED SNN MODELS				
MNIST (MLP)	$80.26 \pm 1.06$	$62.35 \pm 0.93$	$50.39 \pm 0.61$	<b><math>45.26 \pm 0.73</math></b>
FMNIST (MLP)	$81.38 \pm 1.19$	$64.84 \pm 1.25$	$51.08 \pm 0.67$	<b><math>46.38 \pm 0.76</math></b>
CIFAR-10 (VGG-7)	$124.22 \pm 2.42$	$101.57 \pm 2.61$	$78.53 \pm 1.3$	<b><math>68.91 \pm 1.05</math></b>

1076 Table 4 presents the accuracy and summation of inference time over 100 iterations (assuming the actual  
 1077 scenarios) for the SNN models using the lightweight approaches and the proposed mechanism under  
 1078 20% SAFs. Our mechanism exhibits more effective fault mitigation ability than other lightweight  
 1079 approaches, consuming less or comparable inference time to these approaches.

## 1080 B ADDITIONAL EXPERIMENTAL RESULTS ON CLASSIFICATION ACCURACY 1081

1082 We present additional experimental results that support the proposed mechanism in this section.  
1083 The extra results demonstrate that our mechanism enhances the neural networks' fault tolerance  
1084 more effectively than the previous methods<sup>2</sup> in various environments and scenarios, including real  
1085 hardware. Furthermore, we discuss the changes in the proposed mechanism's fault mitigation ability  
1086 by adopting various settings to our mechanism.

### 1088 B.1 ADDITIONAL DATASETS BEYOND MNIST, FMNIST, CIFAR-10, AND CIFAR-100 1089

1090 We use UCI-HAR, AudioMNIST, and Tiny-ImageNet to evaluate the fault mitigation ability of our  
1091 mechanism on a sequential and large-scale dataset.

#### 1092 B.1.1 SEQUENTIAL DATASET 1093

1094 To demonstrate that our mechanism works well with the models using sequential datasets, we conduct  
1095 experiments with UCI-HAR and AudioMNIST, which comprises six types of human activities  
1096 collected by electric sensors and a dataset consisting of verbal sounds of digits (Reyes-Ortiz et al.,  
1097 2013; Becker et al., 2024).

1098 **Table 5:** The MLP model's classification accuracy in a 95% confidence interval using MNIST, FMNIST,  
1099 UCI-HAR, and AudioMNIST with 2 time steps under SAFs.

1100 FAULT RATIO(%)	1101 BASELINE	1101 ECOC	1101 SOFTSNN	1101 ROUTING	1101 ASTROCYTE	1101 FALVOLT	1101 LIFA	1101 PROPOSED
ACCURACY (%) WITH MLP (UCI-HAR)								
0	64.14 $\pm$ 4.91	<b>69.86 <math>\pm</math> 4.73</b>	63.41 $\pm$ 4.78	65.17 $\pm$ 4.65	64.78 $\pm$ 4.39	65.76 $\pm$ 4.55	64.69 $\pm$ 4.81	63.14 $\pm$ 4.8
10	20.19 $\pm$ 2.95	23.01 $\pm$ 4.28	22.21 $\pm$ 4.63	23.1 $\pm$ 4.58	21.25 $\pm$ 3.56	23.24 $\pm$ 4.01	16.93 $\pm$ 4.52	<b>50.31 <math>\pm</math> 4.68</b>
20	19.66 $\pm$ 2.54	17.1 $\pm$ 0	20.52 $\pm$ 3.85	17.1 $\pm$ 0	20.59 $\pm$ 2.81	22.34 $\pm$ 3.68	17.1 $\pm$ 0	<b>49.24 <math>\pm</math> 4.59</b>
30	17.1 $\pm$ 0	17.1 $\pm$ 0	19.9 $\pm$ 2.26	17.1 $\pm$ 0	17.1 $\pm$ 0	19.85 $\pm$ 2.92	17.1 $\pm$ 0	<b>47.31 <math>\pm</math> 4.36</b>
40	17.1 $\pm$ 0	17.1 $\pm$ 0	17.1 $\pm$ 0	17.1 $\pm$ 0	17.1 $\pm$ 0	16.93 $\pm$ 0	17.1 $\pm$ 0	<b>17.21 <math>\pm</math> 0.09</b>
50	17.1 $\pm$ 0	17.1 $\pm$ 0	17.1 $\pm$ 0	17.1 $\pm$ 0	17.1 $\pm$ 0	16.93 $\pm$ 0	17.1 $\pm$ 0	17.1 $\pm$ 0
60	17.1 $\pm$ 0	17.1 $\pm$ 0	17.1 $\pm$ 0	17.1 $\pm$ 0	17.1 $\pm$ 0	16.93 $\pm$ 0	17.1 $\pm$ 0	17.1 $\pm$ 0
70	17.1 $\pm$ 0	17.1 $\pm$ 0	17.1 $\pm$ 0	17.1 $\pm$ 0	17.1 $\pm$ 0	16.93 $\pm$ 0	17.1 $\pm$ 0	17.1 $\pm$ 0
80	17.1 $\pm$ 0	17.1 $\pm$ 0	17.1 $\pm$ 0	17.1 $\pm$ 0	17.1 $\pm$ 0	16.93 $\pm$ 0	17.1 $\pm$ 0	17.1 $\pm$ 0
90	17.1 $\pm$ 0	17.1 $\pm$ 0	17.1 $\pm$ 0	17.1 $\pm$ 0	17.1 $\pm$ 0	16.93 $\pm$ 0	17.1 $\pm$ 0	17.1 $\pm$ 0
ACCURACY (%) WITH MLP (AUDIOMNIST)								
0	96.45 $\pm$ 0.91	<b>96.88 <math>\pm</math> 0.97</b>	95.89 $\pm$ 0.92	96.21 $\pm$ 0.85	96.29 $\pm$ 0.93	96.34 $\pm$ 0.89	96.09 $\pm$ 0.93	96.31 $\pm$ 0.87
10	94.47 $\pm$ 1.07	94.56 $\pm$ 1.79	92.56 $\pm$ 1.61	94.03 $\pm$ 1.84	93.08 $\pm$ 1.92	94.47 $\pm$ 1.58	93.28 $\pm$ 2.18	<b>94.98 <math>\pm</math> 1.54</b>
20	93.17 $\pm$ 1.56	93.29 $\pm$ 1.98	88.15 $\pm$ 2.84	92.59 $\pm$ 2.02	85.24 $\pm$ 3.68	93.29 $\pm$ 2.13	88.57 $\pm$ 4.26	<b>93.78 <math>\pm</math> 1.98</b>
30	92.89 $\pm$ 2.05	93.33 $\pm$ 2.32	75.83 $\pm$ 3.51	91.7 $\pm$ 2.75	51.47 $\pm$ 5.56	92.76 $\pm$ 2.47	55.81 $\pm$ 6.01	<b>93.43 <math>\pm</math> 3.09</b>
40	89.5 $\pm$ 3.21	92.51 $\pm$ 2.15	62.49 $\pm$ 5.07	91.24 $\pm$ 3.18	37.55 $\pm$ 6.27	90.63 $\pm$ 2.99	39.64 $\pm$ 6.8	<b>92.65 <math>\pm</math> 3.17</b>
50	86.15 $\pm$ 4.18	85.46 $\pm$ 3.83	48.61 $\pm$ 6.92	86.45 $\pm$ 3.97	22.13 $\pm$ 4.49	87.51 $\pm$ 4.24	24.48 $\pm$ 5.07	<b>88.93 <math>\pm</math> 4.16</b>
60	52.87 $\pm$ 5.71	66.42 $\pm$ 5.2	34.62 $\pm$ 5.33	64.92 $\pm$ 5.34	10.96 $\pm$ 0.96	65.97 $\pm$ 5.93	12.74 $\pm$ 2.38	<b>67.83 <math>\pm</math> 5.77</b>
70	14.6 $\pm$ 1.23	21.64 $\pm$ 2.15	14.58 $\pm$ 1.4	25.84 $\pm$ 3.42	10 $\pm$ 0	28.18 $\pm$ 3.85	10 $\pm$ 0	<b>37.17 <math>\pm</math> 3.01</b>
80	11.77 $\pm$ 0.95	13.38 $\pm$ 0.94	9.83 $\pm$ 1.05	14.19 $\pm$ 1.36	10 $\pm$ 0	15.53 $\pm$ 2.36	10 $\pm$ 0	<b>19.75 <math>\pm</math> 2.89</b>
90	11.21 $\pm$ 1.01	11.86 $\pm$ 0.87	9.46 $\pm$ 1.22	11.68 $\pm$ 0.96	10 $\pm$ 0	10 $\pm$ 0	10 $\pm$ 0	<b>12.83 <math>\pm</math> 1.02</b>

1106 Table 5 shows the classification accuracy of the MLP model using UCI-HAR. Using the MLP model  
1107 with a sequential dataset, the model with the proposed mechanism exhibits better fault tolerance  
1108 than the baseline and benchmarks, classifying data samples more accurately than the models with  
1109 the baseline and benchmarks. As results with UCI-HAR, the model with the proposed mechanism  
1110 achieves the highest classification accuracy under SAFs. These experimental results with the two  
1111 sequential datasets demonstrate that our mechanism successfully improves fault tolerance of SNNs  
1112 on other domains, such as sensor-obtained and audio data samples.

1113 <sup>2</sup>The benchmarks mentioned in Section 6.

1134  
1135

## B.1.2 LARGE IMAGE DATASET

1136 We use the ResNet-34 model to classify data samples in Tiny-ImageNet, which is a small version  
1137 of the ImageNet dataset, consisting of  $64 \times 64$  pixel images with 200 classes. We measure the  
1138 classification accuracy of the model with Tiny-ImageNet under SAFs.1139 **Table 6:** The ResNet-34 model’s classification accuracy in a 95% confidence interval using Tiny-ImageNet  
1140 under SAFs with 2 time steps.

1141

FAULT RATIO(%)	BASELINE	ECOC	SOFTSNN	ROUTING	ASTROCYTE	FALVOLT	LIFA	PROPOSED
0	$3.38 \pm 2.11$	$3.61 \pm 2.24$	$3.27 \pm 2.08$	$3.24 \pm 2.16$	$0.65 \pm 0.15$	$3.47 \pm 1.98$	$0.59 \pm 0.09$	<b><math>3.96 \pm 2.39</math></b>
10	$0.65 \pm 0.12$	$0.69 \pm 0.15$	$0.68 \pm 0.13$	$0.71 \pm 0.19$	$0.5 \pm 0$	$0.72 \pm 0.16$	$0.5 \pm 0$	<b><math>1.17 \pm 0.28</math></b>
20	$0.5 \pm 0$	<b><math>0.63 \pm 0.12</math></b>						
30	$0.5 \pm 0$	<b><math>0.56 \pm 0.06</math></b>						
40	$0.5 \pm 0$							
50	$0.5 \pm 0$							
60	$0.5 \pm 0$							
70	$0.5 \pm 0$							
80	$0.5 \pm 0$							
90	$0.5 \pm 0$							

1142

1143 Table 6 presents the average classification accuracy of the ResNet-34 model with the baseline,  
1144 benchmarks, and proposed mechanism using Tiny-ImageNet. The classification accuracy of the  
1145 model degrades because the dataset is complex, and SNN models have lower learning capabilities  
1146 compared to DNN models. Despite the low classification accuracy, the model with our mechanism  
1147 classifies data samples in Tiny-ImageNet with the highest accuracy. Moreover, the model with our  
1148 mechanism exhibits higher accuracy than others in the clean scenario (without SAFs). This is because  
1149 our mechanism leads the models to emit the output precisely through entropy-based decoding.

1150

1151

1152

1153

1154

1155

1156

1157

1158

1159

1160

1161

1162

1163

1164

1165

1166

1167

1168

1169

1170

1171

1172

1173

1174

1175

1176

1177

1178

1179

1180

1181

1182

1183

1184

1185

1186

1187

1188  
1189

## B.2 CHANGING THE NUMBER OF TIME STEPS

1190  
1191  
1192

We change the number of time steps to 4 and 8, observing the accuracy trend of all SNN models in the number of time steps. We obtain the experiment results with 4 and 8 time steps by repeating the experiments 10 times.

1193

## B.2.1 4 TIME STEPS

1194

1195

1196

1197

1198

1199

1200

1201

1202

1203

1204

1205

1206

1207

1208

1209

1210

1211

1212

1213

1214

1215

1216

1217

1218

1219

1220

1221

1222

1223

1224

1225

1226

1227

1228

1229

1230

1231

1232

1233

1234

1235

1236

1237

1238

1239

1240

1241

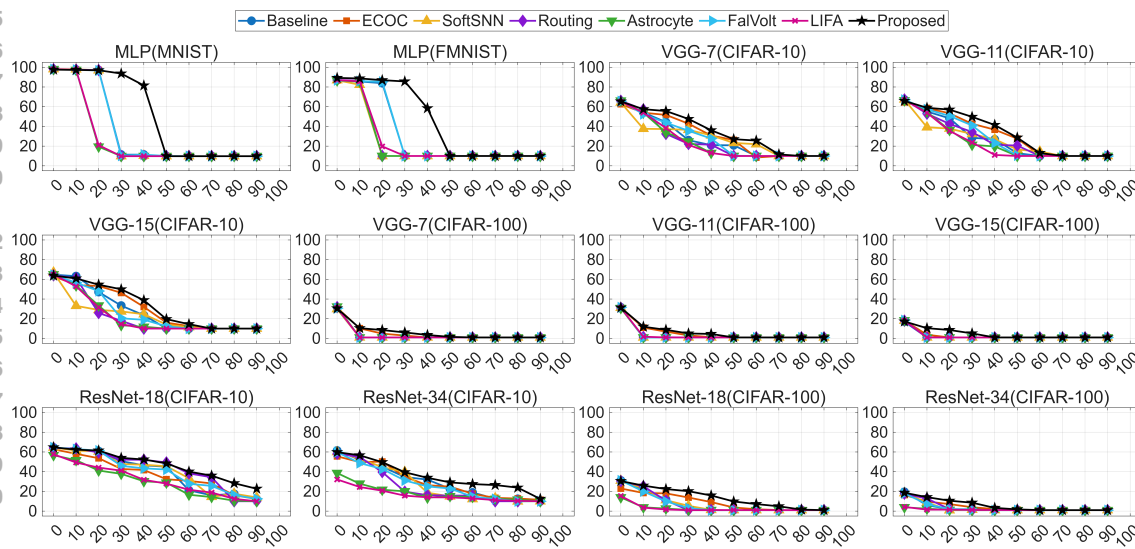


**Figure 6:** Average classification accuracy of various SNN models with the baseline, benchmarks, and proposed mechanism under SAFs using 4 time steps. The x-axis is the fault ratio (%) and the y-axis is the accuracy (%).

Figure 6 illustrates the classification accuracy of SNN models compared to the baseline, benchmarks, and proposed mechanism under SAFs with 4 time steps. The models with our mechanism exhibit the best fault tolerance to faults in most cases, like the experimental results with 2 time steps. We observe that the classification accuracy of all models overall improves as the number of time steps increases, because the large number of time steps improves the performance of SNNs (Li et al., 2024b).

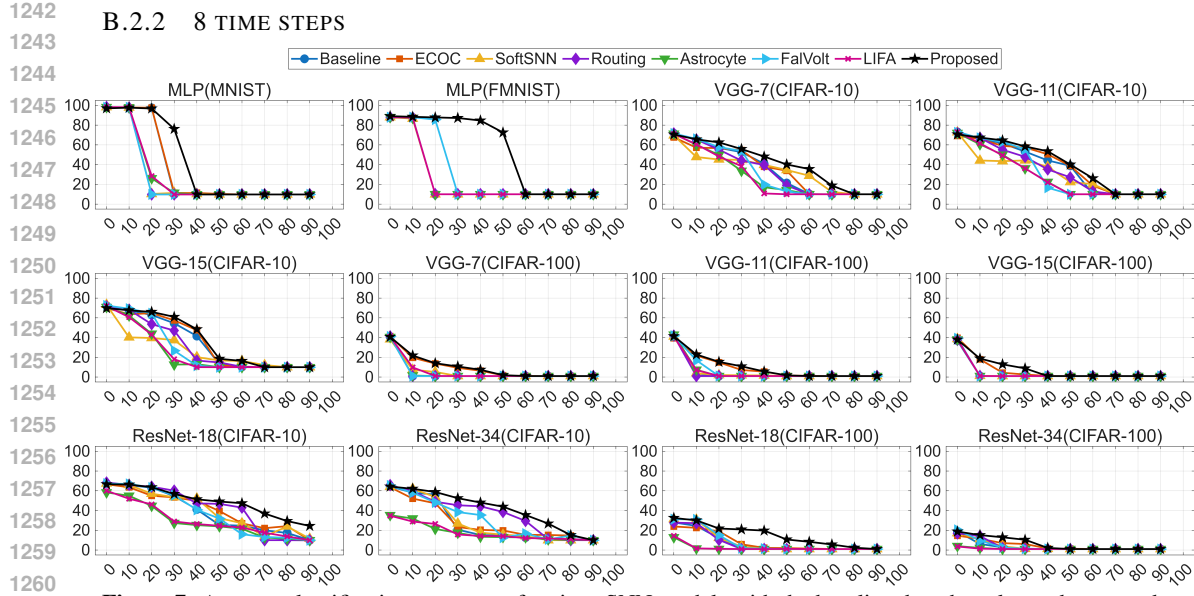


**Figure 7:** Average classification accuracy of various SNN models with the baseline, benchmarks, and proposed mechanism under SAFs using 8 time steps. The x-axis is the fault ratio (%) and the y-axis is the accuracy (%).

Figure 7 depicts the classification accuracy of SNN models compared to the baseline, benchmarks, and proposed mechanism under SAFs with 8 time steps. As demonstrated in the experimental results with 2 and 4 time steps, the models with our mechanism classify data samples most accurately. The models' accuracy is also higher than when using 2 and 4 time steps. Interestingly, the fault mitigation ability of our mechanism degrades only in the experiment with MNIST samples. This is because the MNIST samples contain fewer pixels than FFMNIST, CIFAR-10, and CIFAR-100. However, they are divided into too small fragments, and these fragments do not have sufficient information for the MLP model to learn. Thus, the fault tolerance of the model with our mechanism weakens, although it is more fault-robust than models with the benchmarks.

1296  
1297

## B.3 UNDER THE DIFFERENT TYPES OF SYNAPTIC FAULTS

1298  
1299  
1300

We inject RWFs and CEFs into the synapses of the SNN models and measure the fault mitigation ability of the benchmarks and the proposed mechanism. The models with our mechanism classify data samples most accurately under RWFs and CEFs.

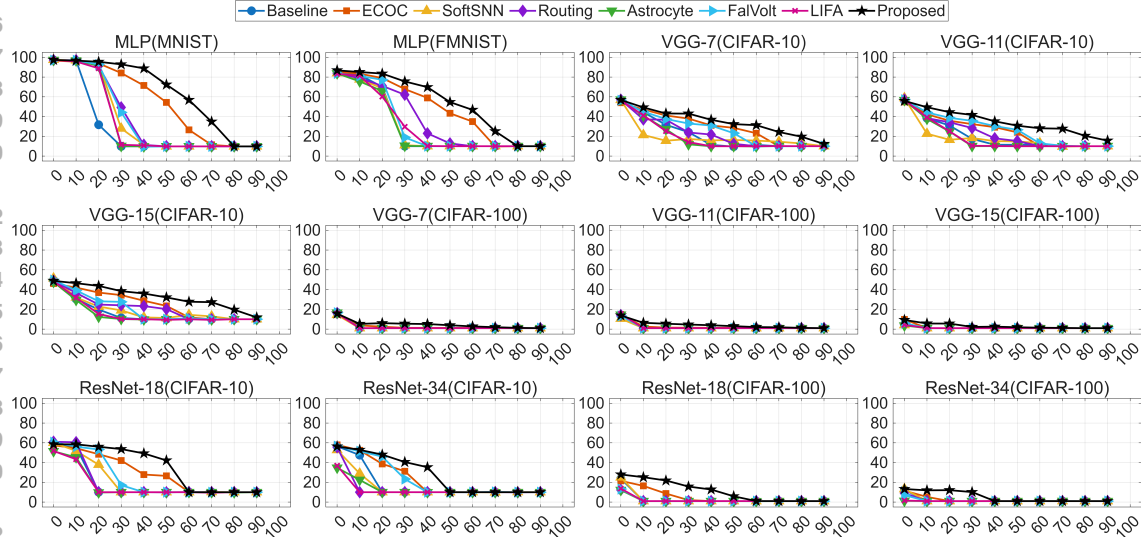
1301

## B.3.1 RWFs

1303  
1304  
1305

We use a Gaussian distribution to model RWFs, setting the standard deviation of the distribution to 0.5 (Garaffa et al., 2021; Spyrou et al., 2021; Vatajelu et al., 2019). We

1306

1311  
1312  
1313  
1314  
1315  
1316  
1317  
1318  
1319  
1320  
1321  
1322

**Figure 8:** Average classification accuracy of various SNN models with the baseline, benchmarks, and proposed mechanism under RWFs using 2 time steps. The x-axis is the fault ratio (%) and the y-axis is the accuracy (%).

1323  
1324  
1325  
1326  
1327  
1328  
1329  
1330  
1331  
1332  
1333  
1334  
1335  
1336  
1337  
1338  
1339  
1340  
1341  
1342  
1343  
1344  
1345  
1346  
1347  
1348  
1349

Figure 8 depicts the classification accuracy of SNN models with the baseline, benchmarks, and proposed mechanism under RWFs. The models with our mechanism exhibit the highest accuracy in classifying MNIST, FMNIST, CIFAR-10, and CIFAR-100. This is because our mechanism successfully prevents the pre-activation magnitude from increasing excessively by RWFs. Interestingly, ECOC presents high fault mitigation ability under RWFs. This is because ECOC uses error correcting codes, which are robust against Gaussian noise in channels to compensate for errors caused by faults in the last layer (Liu et al., 2019).

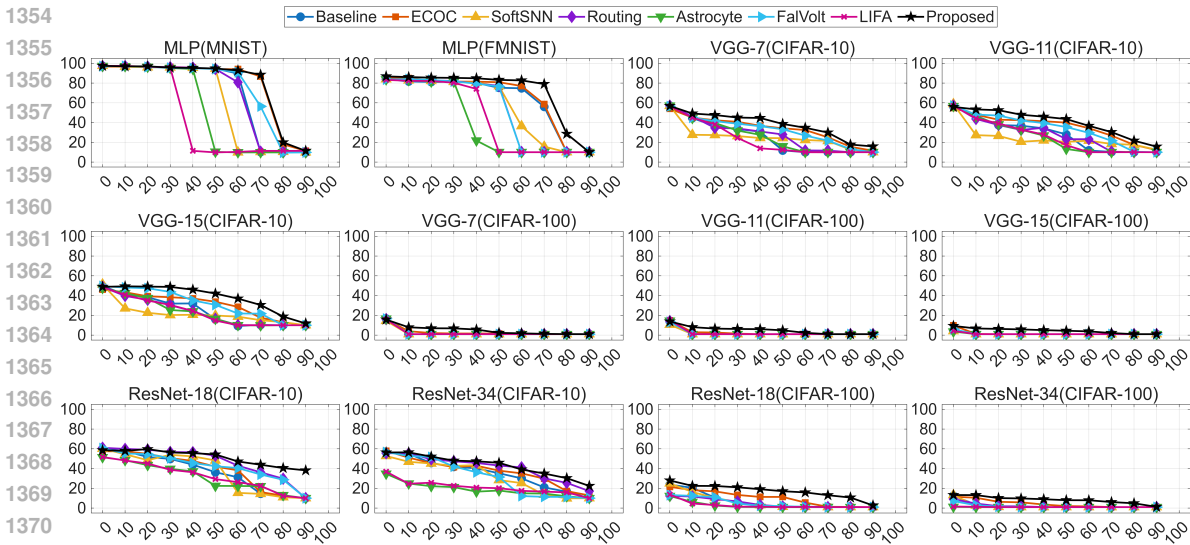
1350 B.3.2 CEFs  
13511352 CEFs change the connections between spiking neurons randomly, ruining the learned information of  
1353 SNN models (Vatajelu et al., 2019).1354  
1355  
1356  
1357  
1358  
1359  
1360  
1361  
1362  
1363  
1364  
1365  
1366  
1367  
1368  
1369  
1370  
1371  
1372  
1373  
1374  
1375  
1376  
1377  
1378  
1379  
1380  
1381  
1382  
1383  
1384  
1385  
1386  
1387  
1388  
1389  
1390  
1391  
1392  
1393  
1394  
1395  
1396  
1397  
1398  
1399  
1400  
1401  
1402  
1403  
**Figure 9:** Average classification accuracy of various SNN models with the baseline, benchmarks, and proposed mechanism under CEFs using 2 time steps. The x-axis is the fault ratio (%) and the y-axis is the accuracy (%).

Figure 9 illustrates the classification accuracy of SNN models with the baseline, benchmarks, and proposed mechanism under CEFs. Our mechanism also presents the best fault mitigation ability. The classification accuracy of SNN models under CEFs is higher than that of the models under SAFs and RWFs. This is because the weights of faulty synapses are uniform under CEFs, and the pre-activation magnitude does not increase significantly. Thus, the pre-activation does not lie in a value that is far from the surrogate gradient corridor.

1404 B.4 ABLATION STUDY ON THE COMBINATION OF OUR MECHANISM  
14051406 We conduct ablation studies by changing the settings of our mechanism (horizontally-fixed vs Gini-  
1407 based and only complexity-based sensitivity score vs complexity and influence combined sensitivity  
1408 score).1409 B.4.1 MLP MODEL (MNIST, FMNIST)  
14101411 **Table 7:** The MLP model’s classification accuracy in a 95% confidence interval with different settings of our  
1412 mechanism under SAFs.  
1413

FAULT RATIO(%)	BASELINE	HORIZONTAL	GINI(COMPLEXITY ONLY)	GINI(PROPOSED)
ACCURACY (%) WITH MLP (MNIST)				
0	$97.35 \pm 0.46$	$86.68 \pm 3.51$	$97.37 \pm 0.44$	<b><math>97.44 \pm 0.39</math></b>
10	$96.94 \pm 1.01$	$75.77 \pm 4.96$	$96.76 \pm 0.95$	<b><math>97.25 \pm 0.98</math></b>
20	$11.35 \pm 0$	$71.13 \pm 4.81$	$93.64 \pm 1.44$	<b><math>93.84 \pm 1.37</math></b>
30	$10.82 \pm 0$	$65.78 \pm 5.39$	$91.56 \pm 2.61$	<b><math>93.55 \pm 1.94</math></b>
40	$10.82 \pm 0$	$11.35 \pm 0$	$11.35 \pm 0$	<b><math>86.71 \pm 4.68</math></b>
50	$9.8 \pm 0$	$9.8 \pm 0$	$9.8 \pm 0$	<b><math>26.91 \pm 7.53</math></b>
60	$9.8 \pm 0$	$9.8 \pm 0$	$9.8 \pm 0$	$9.8 \pm 0$
70	$9.8 \pm 0$	$9.8 \pm 0$	$9.8 \pm 0$	$9.8 \pm 0$
80	$9.8 \pm 0$	$9.8 \pm 0$	$9.8 \pm 0$	$9.8 \pm 0$
90	$9.8 \pm 0$	$9.8 \pm 0$	$9.8 \pm 0$	$9.8 \pm 0$
ACCURACY (%) WITH MLP (FMNIST)				
0	$83.99 \pm 0.86$	$78.09 \pm 1.03$	$86.29 \pm 0.94$	<b><math>86.8 \pm 0.89</math></b>
10	$83.74 \pm 1.79$	$76.78 \pm 1.9$	$85.49 \pm 1.43$	<b><math>85.6 \pm 1.23</math></b>
20	$10 \pm 0$	$74.22 \pm 2.54$	$80.41 \pm 2.19$	<b><math>85.33 \pm 1.45</math></b>
30	$10 \pm 0$	$70.65 \pm 6.17$	$79.6 \pm 3.72$	<b><math>83.53 \pm 2.69</math></b>
40	$10 \pm 0$	$17.16 \pm 8.84$	$21.93 \pm 7.63$	<b><math>54.55 \pm 6.76</math></b>
50	$10 \pm 0$	$10 \pm 0$	$10 \pm 0$	$10 \pm 0$
60	$10 \pm 0$	$10 \pm 0$	$10 \pm 0$	$10 \pm 0$
70	$10 \pm 0$	$10 \pm 0$	$10 \pm 0$	$10 \pm 0$
80	$10 \pm 0$	$10 \pm 0$	$10 \pm 0$	$10 \pm 0$
90	$10 \pm 0$	$10 \pm 0$	$10 \pm 0$	$10 \pm 0$

1437 Table 7 presents the classification accuracy of the baseline, horizontally-fixed fragmentation, Gini-  
1438 based fragmentation using image complexity for the sensitivity score, and Gini-based fragmentation  
1439 using image complexity and fault influence of the first layer for the sensitivity score (proposed)  
1440 when using MNIST models to classify MNIST and FMNIST data samples. The proposed version  
1441 significantly enhances the fault tolerance of the MLP model, as demonstrated by its performance  
1442 on MNIST and FMNIST, compared to other settings. This is because the MLP model is vulnerable  
1443 to faults in the first layer, as mentioned in Section 4. Thus, using fault influence for the sensitivity  
1444 score enhances our mechanism’s fault mitigation ability since it induces the mechanism to minimize  
1445 the pre-activation magnitude. We also observe that the wrong fragmentation strategy degrades  
1446 classification performance because it damages the information of data samples.  
1447  
1448  
1449  
1450  
1451  
1452  
1453  
1454  
1455  
1456  
1457

1458 B.4.2 VGG-7 AND RESNET-18 MODELS (CIFAR-10 AND CIFAR-100)  
14591460 **Table 8:** The VGG-7 and ResNet-18 models’ classification accuracy in a 95% confidence interval with different  
1461 settings of our mechanism under SAFs.  
1462

FAULT RATIO(%)	BASELINE	HORIZONTAL	GINI(COMPLEXITY ONLY)	GINI(PROPOSED)
ACCURACY (%) WITH VGG-7 (CIFAR-10)				
0	56.26 ± 1.28	55.75 ± 1.33	56.68 ± 1.28	<b>56.86 ± 1.63</b>
10	40.09 ± 3.34	48.8 ± 2.67	49.13 ± 2.32	<b>50.38 ± 2.07</b>
20	31.78 ± 4.97	42.69 ± 3.83	45.39 ± 3.44	<b>45.58 ± 3.76</b>
30	11.74 ± 4.81	36.55 ± 4.64	38.23 ± 4.91	<b>40.26 ± 5.04</b>
40	10.79 ± 3.56	29.09 ± 5.72	31.18 ± 5.52	<b>32.07 ± 5.15</b>
50	10 ± 0	10 ± 0	10 ± 0	<b>17.08 ± 5.74</b>
60	10 ± 0	10 ± 0	10 ± 0	10 ± 0
70	10 ± 0	10 ± 0	10 ± 0	10 ± 0
80	10 ± 0	10 ± 0	10 ± 0	10 ± 0
90	10 ± 0	10 ± 0	10 ± 0	10 ± 0
ACCURACY (%) WITH RESNET-18 (CIFAR-100)				
0	23.77 ± 4.56	24.12 ± 4.69	25.11 ± 4.74	<b>27.96 ± 4.83</b>
10	10.64 ± 3.82	23.98 ± 4.41	24.15 ± 4.32	<b>25.5 ± 4.79</b>
20	6.1 ± 2.65	19.86 ± 5.52	21.92 ± 5.48	<b>24.41 ± 5.38</b>
30	1.98 ± 0.93	16.62 ± 4.63	18.43 ± 5.01	<b>19.72 ± 5.23</b>
40	1.03 ± 0.82	13.53 ± 4.29	14.26 ± 4.57	<b>16.8 ± 4.72</b>
50	0.97 ± 0.79	11.89 ± 4.17	12.34 ± 4.48	<b>13.13 ± 4.52</b>
60	1.01 ± 0.86	4.68 ± 2.1	5.12 ± 2.96	<b>6.25 ± 3.26</b>
70	1 ± 0	2.25 ± 1.12	3.9 ± 1.44	<b>4.27 ± 1.56</b>
80	1 ± 0	1 ± 0	1 ± 0	<b>1.24 ± 0.81</b>
90	1 ± 0	1 ± 0	1 ± 0	1 ± 0

1485 Table 8 exhibits our ablation study with VGG-7 and ResNet-18 models using CIFAR-10 and CIFAR-  
1486 100. Although the proposed mechanism outperforms other settings, the improvement in fault  
1487 mitigation ability is not as large as in the cases with the MLP models. This is because VGG-7 and  
1488 ResNet-18 models are not as vulnerable to faults in the first layer as the MLP model since they have  
1489 additional features to compensate for errors during gradient calculations. Therefore, containing the  
1490 fault influence in the sensitivity score does not significantly enhance the fault mitigation ability of our  
1491 mechanism.  
1492  
1493  
1494  
1495  
1496  
1497  
1498  
1499  
1500  
1501  
1502  
1503  
1504  
1505  
1506  
1507  
1508  
1509  
1510  
1511

1512  
1513

## B.5 VARIOUS HYPERPARAMETER SETTINGS WITH OUR MECHANISM

1514  
1515We change  $(\lambda_s, \lambda_w)$  to  $(0.5, 0.5)$ ,  $(0.5, 0.1)$ , and  $(0.1, 0.5)$  to show the influence of hyperparameters on our mechanism.

1516

1517

## B.5.1 MLP MODEL (MNIST AND FMNIST)

1518

1519  
1520**Table 9:** The MLP model’s classification accuracy in a 95% confidence interval with different settings of the hyperparameter  $(\lambda_s, \lambda_w)$  under SAFs.

1521

1522

FAULT RATIO(%)	(0.5, 0.5)	(0.5, 0.1)	(0.1, 0.5)	(0.1, 0.1) (DEFAULT)
ACCURACY (%) WITH MLP (MNIST)				
0	$97.28 \pm 0.53$	$97.35 \pm 0.54$	$97.29 \pm 0.51$	<b><math>97.44 \pm 0.39</math></b>
10	$96.34 \pm 1.25$	$96.58 \pm 1.38$	$96.05 \pm 1.19$	<b><math>97.25 \pm 0.98</math></b>
20	$95.29 \pm 1.67$	$93.3 \pm 1.63$	$95.43 \pm 1.58$	<b><math>93.84 \pm 1.37</math></b>
30	$91.59 \pm 2.82$	$92.15 \pm 2.97$	$86.93 \pm 2.86$	<b><math>93.55 \pm 1.94</math></b>
40	$9.8 \pm 0$	$14.28 \pm 5.47$	$10.48 \pm 1.39$	<b><math>86.71 \pm 4.68</math></b>
50	$9.8 \pm 0$	$12.6 \pm 5.61$	$9.8 \pm 0$	<b><math>26.91 \pm 7.53</math></b>
60	$9.8 \pm 0$	$9.8 \pm 0$	$9.8 \pm 0$	$9.8 \pm 0$
70	$9.8 \pm 0$	$9.8 \pm 0$	$9.8 \pm 0$	$9.8 \pm 0$
80	$9.8 \pm 0$	$9.8 \pm 0$	$9.8 \pm 0$	$9.8 \pm 0$
90	$9.8 \pm 0$	$9.8 \pm 0$	$9.8 \pm 0$	$9.8 \pm 0$
ACCURACY (%) WITH MLP (FMNIST)				
0	$85.53 \pm 1.05$	$85.56 \pm 1.14$	$85.29 \pm 0.99$	<b><math>86.8 \pm 0.89</math></b>
10	$85.46 \pm 1.46$	$85.52 \pm 1.31$	$85.23 \pm 1.36$	<b><math>85.6 \pm 1.23</math></b>
20	$80.89 \pm 3.48$	$83.57 \pm 2.12$	$84.41 \pm 2.29$	<b><math>85.33 \pm 1.45</math></b>
30	$80.23 \pm 3.8$	$31.58 \pm 7.03$	$75.39 \pm 5.45$	<b><math>83.53 \pm 2.69</math></b>
40	$33.54 \pm 6.15$	$18.84 \pm 7.65$	$10 \pm 0$	<b><math>54.55 \pm 6.76</math></b>
50	$10 \pm 0$	$10 \pm 0$	$10 \pm 0$	$10 \pm 0$
60	$10 \pm 0$	$10 \pm 0$	$10 \pm 0$	$10 \pm 0$
70	$10 \pm 0$	$10 \pm 0$	$10 \pm 0$	$10 \pm 0$
80	$10 \pm 0$	$10 \pm 0$	$10 \pm 0$	$10 \pm 0$
90	$10 \pm 0$	$10 \pm 0$	$10 \pm 0$	$10 \pm 0$

1543

Table 9 exhibits the MLP model’s classification accuracy by changing  $(\lambda_s$  and  $\lambda_w)$  under SAFs. The hyperparameter settings predominantly affect the classification accuracy of the MLP model, as they adjust how the mechanism mitigates the adverse influence of synaptic faults in the first layer, which damages the model the most severely. We observe that increasing the hyperparameters and strengthening the effects of the fault influence map do not always leverage the MLP model’s fault tolerance. This is because the excessive effects of the fault influence map prevent our mechanism from setting the angle accurately by reflecting the complexity of the input samples and the fault influence in a balanced way. In addition, we observe that the weight projection map affects our mechanism more predominantly than the saliency map, since the weight projection map is more sensitive to changes in weights due to synaptic faults.

1553

1554

1555

1556

1557

1558

1559

1560

1561

1562

1563

1564

1565

1566 B.5.2 VGG-7 AND RESNET-18 MODELS (CIFAR-10 AND CIFAR-100)  
15671568 **Table 10:** The VGG-7 and ResNet-18 models’ classification accuracy in a 95% confidence interval with different  
1569 settings of the hyperparameter ( $\lambda_s, \lambda_w$ ) under SAFs.  
1570

FAULT RATIO(%)	(0.5, 0.5)	(0.5, 0.1)	(0.1, 0.5)	(0.1, 0.1) (DEFAULT)
ACCURACY (%) WITH VGG-7 (CIFAR-10)				
0	56.48 $\pm$ 1.84	56.06 $\pm$ 1.73	56.03 $\pm$ 1.89	<b>56.86 <math>\pm</math> 1.63</b>
10	48.12 $\pm$ 3.04	48.88 $\pm$ 2.85	49.34 $\pm$ 2.16	<b>50.38 <math>\pm</math> 2.07</b>
20	44.68 $\pm$ 3.69	44.56 $\pm$ 3.66	45.3 $\pm$ 3.59	<b>45.58 <math>\pm</math> 3.76</b>
30	39.42 $\pm$ 5.25	39.22 $\pm$ 5.59	39.92 $\pm$ 5.23	<b>40.26 <math>\pm</math> 5.04</b>
40	29.62 $\pm$ 5.38	29.52 $\pm$ 5.04	30.21 $\pm$ 5.4	<b>32.07 <math>\pm</math> 5.15</b>
50	15.09 $\pm$ 4.76	15.28 $\pm$ 5.17	15.31 $\pm$ 4.98	<b>17.08 <math>\pm</math> 5.74</b>
60	10 $\pm$ 0	10 $\pm$ 0	10 $\pm$ 0	10 $\pm$ 0
70	10 $\pm$ 0	10 $\pm$ 0	10 $\pm$ 0	10 $\pm$ 0
80	10 $\pm$ 0	10 $\pm$ 0	10 $\pm$ 0	10 $\pm$ 0
90	10 $\pm$ 0	10 $\pm$ 0	10 $\pm$ 0	10 $\pm$ 0
ACCURACY (%) WITH RESNET-18 (CIFAR-100)				
0	26.96 $\pm$ 5.08	26.02 $\pm$ 4.93	25.71 $\pm$ 5.86	<b>27.96 <math>\pm</math> 4.83</b>
10	24.26 $\pm$ 4.29	24.76 $\pm$ 4.38	21.75 $\pm$ 4.71	<b>25.5 <math>\pm</math> 4.79</b>
20	20.09 $\pm$ 5.66	21.23 $\pm$ 5.96	19.03 $\pm$ 5.09	<b>24.41 <math>\pm</math> 5.38</b>
30	16.88 $\pm$ 5.48	17.7 $\pm$ 5.48	15.89 $\pm$ 5.42	<b>19.72 <math>\pm</math> 5.23</b>
40	13.25 $\pm$ 5.24	13.68 $\pm$ 5.05	13.25 $\pm$ 4.93	<b>16.8 <math>\pm</math> 4.71</b>
50	12.04 $\pm$ 4.93	12.55 $\pm$ 4.34	9.14 $\pm$ 4.69	<b>13.13 <math>\pm</math> 4.5</b>
60	4.46 $\pm$ 3.52	4.77 $\pm$ 3.15	4.86 $\pm$ 2.96	<b>6.25 <math>\pm</math> 3.26</b>
70	3.61 $\pm$ 1.95	2.89 $\pm$ 1.7	3.05 $\pm$ 1.78	<b>4.27 <math>\pm</math> 1.56</b>
80	1 $\pm$ 0	1 $\pm$ 0	1 $\pm$ 0	<b>1.24 <math>\pm</math> 0.81</b>
90	1 $\pm$ 0	1 $\pm$ 0	1 $\pm$ 0	1 $\pm$ 0

1593 Table 10 presents the VGG and ResNet Models’ classification accuracy by changing ( $\lambda_s$  and  $\lambda_w$ )  
1594 under SAFs. Since the significance of the faults in the first layer of the VGG and ResNet Models is  
1595 weaker than that of the MLP model, the sensitivity to hyperparameter setting is smaller than that of  
1596 the MLP model. Despite the low significance of tuning hyperparameters when using the VGG and  
1597 ResNet Models, setting the hyperparameters to the proper value is still important to ensure the best  
1598 fault mitigation ability of our mechanism.  
1599  
1600  
1601  
1602  
1603  
1604  
1605  
1606  
1607  
1608  
1609  
1610  
1611  
1612  
1613  
1614  
1615  
1616  
1617  
1618  
1619

1620  
1621

## B.6 USING DEEP NEURAL NETWORKS (DNNs)

1622  
1623  
1624  
1625  
1626  
1627  
1628  
1629

We inject SAFs into synapses of Deep Neural Networks (DNNs) version of the SNN models, measuring their classification accuracy with the baseline, benchmarks, and proposed mechanism. We use Cross-Entropy (CE) as a loss function and Rectified Linear Unit (ReLU) as an activation function. We set the range of weights to [-100, 100] for MLP and [-500, 500] for CNNs (VGG and ResNet) since current DNN accelerator devices have a large weight range (Liu et al., 2019; Chen et al., 2017). Other settings are the same as the SNN models. We exclude Astrocyte, FalVolt, and LIFA from the benchmarks since they necessarily require bio-plausible spiking neuron models for operation. We use 2 fragments for our mechanism.

1630  
1631

**Table 11:** The DNN models’ classification accuracy in a 95% confidence interval using MNIST, FMNIST, CIFAR-10, and CIFAR-100 under SAFs.

1632

FAULT RATIO(%)	BASELINE	ECOC	SOFTSNN (TUNED FOR DNN)	ROUTING	PROPOSED
ACCURACY(%) WITH MLP (MNIST)					
0	98.48 $\pm$ 0.19	<b>98.6 <math>\pm</math> 0.26</b>	98.49 $\pm$ 0.23	98.45 $\pm$ 0.31	98.54 $\pm$ 0.25
10	97.32 $\pm$ 0.86	97.28 $\pm$ 0.81	97.48 $\pm$ 0.96	97.28 $\pm$ 0.89	<b>97.56 <math>\pm</math> 0.74</b>
20	96.62 $\pm$ 1.55	9.8 $\pm$ 0	97.02 $\pm$ 1.32	96.76 $\pm$ 1.47	<b>96.85 <math>\pm</math> 1.38</b>
30	96.58 $\pm$ 1.93	9.8 $\pm$ 0	96.3 $\pm$ 1.89	96.64 $\pm$ 1.69	<b>96.72 <math>\pm</math> 1.71</b>
40	96.35 $\pm$ 1.81	9.8 $\pm$ 0	96.02 $\pm$ 1.76	96.43 $\pm$ 1.74	<b>96.48 <math>\pm</math> 1.85</b>
50	93.3 $\pm$ 3.52	9.8 $\pm$ 0	93.47 $\pm$ 3.62	93.54 $\pm$ 4.02	<b>93.58 <math>\pm</math> 3.91</b>
60	77.36 $\pm$ 9.15	9.8 $\pm$ 0	78.03 $\pm$ 8.99	79.89 $\pm$ 8.56	<b>82.62 <math>\pm</math> 8.8</b>
70	65.9 $\pm$ 10.49	9.8 $\pm$ 0	68.39 $\pm$ 10.05	67.79 $\pm$ 9.95	<b>74.8 <math>\pm</math> 9.72</b>
80	39.64 $\pm$ 8.77	9.8 $\pm$ 0	41.31 $\pm$ 9.12	18.71 $\pm$ 8.89	<b>55.43 <math>\pm</math> 8.73</b>
90	8.92 $\pm$ 0	9.8 $\pm$ 0	9.8 $\pm$ 0	15.5 $\pm$ 5.7	<b>19.07 <math>\pm</math> 6.21</b>
ACCURACY(%) WITH MLP (FMNIST)					
0	90.05 $\pm$ 1.22	<b>91.24 <math>\pm</math> 1.3</b>	90.08 $\pm$ 1.24	90.12 $\pm$ 1.13	90.51 $\pm$ 1.19
10	84.38 $\pm$ 2.73	10 $\pm$ 0	84.72 $\pm$ 2.86	86.03 $\pm$ 2.69	<b>86.83 <math>\pm</math> 2.71</b>
20	71.67 $\pm$ 3.49	10 $\pm$ 0	72.07 $\pm$ 3.35	74.51 $\pm$ 3.48	<b>79.66 <math>\pm</math> 3.48</b>
30	68.01 $\pm$ 5.05	10 $\pm$ 0	70.75 $\pm$ 4.94	73.54 $\pm$ 4.75	<b>74.63 <math>\pm</math> 4.79</b>
40	64.93 $\pm$ 5.91	10 $\pm$ 0	63.5 $\pm$ 6.04	64.06 $\pm$ 5.97	<b>65.23 <math>\pm</math> 6.25</b>
50	58.63 $\pm$ 6.27	10 $\pm$ 0	62.78 $\pm$ 6.38	60.92 $\pm$ 6.09	<b>64.8 <math>\pm</math> 6.31</b>
60	53.57 $\pm$ 7.86	10 $\pm$ 0	57.01 $\pm$ 8.11	54.51 $\pm$ 9.23	<b>58.68 <math>\pm</math> 8.77</b>
70	38.01 $\pm$ 9.91	10 $\pm$ 0	39.48 $\pm$ 10.26	35.12 $\pm$ 9.84	<b>41.62 <math>\pm</math> 10.34</b>
80	23.5 $\pm$ 8.44	10 $\pm$ 0	26.45 $\pm$ 8.79	25.41 $\pm$ 7.98	<b>33.21 <math>\pm</math> 8.59</b>
90	10 $\pm$ 0	10 $\pm$ 0	10 $\pm$ 0	10 $\pm$ 0	<b>11.02 <math>\pm</math> 1.02</b>
ACCURACY(%) WITH VGG-7 (CIFAR-10)					
0	83.21 $\pm$ 2.76	83.36 $\pm$ 2.58	83.58 $\pm$ 2.53	83.73 $\pm$ 2.47	<b>84.29 <math>\pm</math> 2.63</b>
0.01	10 $\pm$ 0	10 $\pm$ 0	52.97 $\pm$ 4.84	67.78 $\pm$ 5.04	<b>70.36 <math>\pm</math> 4.81</b>
0.025	10 $\pm$ 0	10 $\pm$ 0	10 $\pm$ 0	10 $\pm$ 0	10 $\pm$ 0
0.05	10 $\pm$ 0	10 $\pm$ 0	10 $\pm$ 0	10 $\pm$ 0	10 $\pm$ 0
0.075	10 $\pm$ 0	10 $\pm$ 0	10 $\pm$ 0	10 $\pm$ 0	10 $\pm$ 0
ACCURACY(%) WITH RESNET-18 (CIFAR-100)					
0	53.09 $\pm$ 1.02	40.96 $\pm$ 1.56	53.51 $\pm$ 1.16	53.6 $\pm$ 1.24	<b>53.82 <math>\pm</math> 1.19</b>
0.01	46.17 $\pm$ 1.35	37.87 $\pm$ 1.53	47.26 $\pm$ 1.58	46.99 $\pm$ 1.56	<b>48.49 <math>\pm</math> 1.47</b>
0.025	43.32 $\pm$ 1.68	34.05 $\pm$ 1.79	43.76 $\pm$ 1.73	44.07 $\pm$ 1.79	<b>45.09 <math>\pm</math> 1.66</b>
0.05	41.14 $\pm$ 1.54	32.28 $\pm$ 2.01	42.23 $\pm$ 1.69	42.51 $\pm$ 1.55	<b>42.78 <math>\pm</math> 1.48</b>
0.075	39.05 $\pm$ 1.82	31.64 $\pm$ 1.98	40.64 $\pm$ 1.91	39.89 $\pm$ 2.05	<b>41.32 <math>\pm</math> 1.85</b>

1661  
1662  
1663  
1664  
1665  
1666  
1667  
1668  
1669  
1670  
1671  
1672  
1673

Table 11 presents the classification accuracy of DNN models with the baseline, benchmarks, and proposed mechanism. The models with ours exhibit the highest fault robustness among the DNN models since our mechanism prevents the pre-activation from increasing excessively, and gradients do not explode severely during training. The MLP DNN model presents higher fault tolerance than the SNN model regardless of the datasets. This is because the gradient vanishing caused by pre-activation magnitude growth does not occur severely, since gradients are active when the pre-activation is larger than 0 in ReLU. Conversely, the fault tolerance of the complicated CNN models (VGG and ResNet) degrades seriously. This situation appears because these models use lots of batch normalization layers. The normalization layers normalize the whole channels in the same scale calculated with the batch samples, causing the amplification of inputs that enter faulty synapses. However, the SNN VGG and ResNet models are more tolerant of faults than the DNN versions. This is because the spiking neurons block the perturbation from faults through their internal activation mechanism: only firing and emitting spikes when their membrane potential reaches the threshold (Liang et al., 2023).

1674 B.7 USING SNNs WITH UNSUPERVISED LEARNING  
1675

1676 The SNN models using unsupervised learning are also important models to implement on-chip  
1677 learning of neuromorphic devices. Therefore, we adopt the benchmarks and proposed mechanism to  
1678 the widely used SNN model: Diehl&Cook2015 using Spike-Timing-Dependent Plasticity (STDP),  
1679 which is a representative unsupervised learning rule (Lee & Lim, 2024; Diehl & Cook, 2015). We  
1680 use a reliable framework to implement STDP-based SNNs, named BindsNET, for our experiments  
1681 (Hazan et al., 2018).

1682 **Table 12:** The Diehl&Cook2015 model’s classification accuracy in a 95% confidence interval using MNIST and  
1683 FMNIST with 250 time steps under SAFs.

FAULT RATIO(%)	BASELINE	SOFTSNN	ROUTING	ASTROCYTE	FALVOLT	LIFA	PROPOSED
ACCURACY (%) WITH DIEHL&COOK2015 (MNIST)							
0	86.37 $\pm$ 1.23	85.96 $\pm$ 1.45	86.34 $\pm$ 1.28	86.49 $\pm$ 1.65	<b>86.41 <math>\pm</math> 1.61</b>	86.16 $\pm$ 1.54	85.69 $\pm$ 1.72
10	77.07 $\pm$ 1.86	79.34 $\pm$ 2.51	78.5 $\pm$ 2.08	79.16 $\pm$ 1.93	78.89 $\pm$ 2.02	79.58 $\pm$ 2.37	<b>81.03 <math>\pm</math> 2.44</b>
20	76.41 $\pm$ 1.9	78.48 $\pm$ 2.67	77.27 $\pm$ 2.36	78.91 $\pm$ 1.88	78.04 $\pm$ 2.45	78.61 $\pm$ 2.51	<b>80.27 <math>\pm</math> 2.53</b>
30	74.45 $\pm$ 2.79	76.59 $\pm$ 2.81	77.03 $\pm$ 3.05	77.62 $\pm$ 2.56	78.04 $\pm$ 3.16	78.72 $\pm$ 2.98	<b>79.86 <math>\pm</math> 3.14</b>
40	70.87 $\pm$ 4.52	71.95 $\pm$ 4.93	72.35 $\pm$ 4.74	72.48 $\pm$ 4.59	73.19 $\pm$ 4.72	73.43 $\pm$ 4.6	<b>76.57 <math>\pm</math> 3.66</b>
50	69.7 $\pm$ 5.15	70.83 $\pm$ 5.26	72.08 $\pm$ 4.91	71.27 $\pm$ 5.38	71.96 $\pm$ 5.84	71.78 $\pm$ 5.64	<b>74.36 <math>\pm</math> 5.42</b>
60	67.79 $\pm$ 5.98	69.25 $\pm$ 6.2	70.7 $\pm$ 6.12	69.49 $\pm$ 5.84	70.35 $\pm$ 6.27	70.96 $\pm$ 6.32	<b>72.18 <math>\pm</math> 5.96</b>
70	63.46 $\pm$ 5.76	65.51 $\pm$ 5.69	65.28 $\pm$ 5.57	66.93 $\pm$ 5.65	65.97 $\pm$ 5.96	68.08 $\pm$ 5.84	<b>70.4 <math>\pm</math> 5.71</b>
80	54.62 $\pm$ 4.84	56.26 $\pm$ 4.98	55.93 $\pm$ 5.05	57.15 $\pm$ 4.72	56.59 $\pm$ 5.13	59.27 $\pm$ 4.99	<b>62.11 <math>\pm</math> 5.27</b>
90	33.25 $\pm$ 3.61	38.59 $\pm$ 4.06	40.27 $\pm$ 3.96	39.45 $\pm$ 4.11	41.73 $\pm$ 4.5	43.98 $\pm$ 4.76	<b>52.64 <math>\pm</math> 4.98</b>
ACCURACY (%) WITH DIEHL&COOK2015 (FMNIST)							
0	27.4 $\pm$ 2.68	27.61 $\pm$ 2.75	27.57 $\pm$ 2.46	27.43 $\pm$ 2.37	<b>27.77 <math>\pm</math> 2.84</b>	27.59 $\pm$ 2.7	26.76 $\pm$ 2.36
10	22.66 $\pm$ 3.83	24.54 $\pm$ 3.96	24.8 $\pm$ 3.69	24.96 $\pm$ 3.92	25.11 $\pm$ 3.63	25.7 $\pm$ 3.91	<b>26.17 <math>\pm</math> 3.94</b>
20	20.84 $\pm$ 3.95	22.55 $\pm$ 4.12	22.89 $\pm$ 4.17	22.74 $\pm$ 3.86	22.68 $\pm$ 4.09	23.59 $\pm$ 4.28	<b>23.85 <math>\pm</math> 4.47</b>
30	18.81 $\pm$ 4.06	20.72 $\pm$ 4.27	21.63 $\pm$ 4.15	20.98 $\pm$ 4.07	21.16 $\pm$ 3.96	22.07 $\pm$ 3.96	<b>22.83 <math>\pm</math> 4.25</b>
40	15.47 $\pm$ 2.97	16.8 $\pm$ 3.11	17.25 $\pm$ 3.08	16.97 $\pm$ 3.2	17.15 $\pm$ 3.19	18.23 $\pm$ 3.38	<b>20.65 <math>\pm</math> 3.8</b>
50	12.35 $\pm$ 1.76	13.15 $\pm$ 2.57	12.98 $\pm$ 2.61	13.41 $\pm$ 2.85	13.61 $\pm$ 2.79	14.02 $\pm$ 2.91	<b>14.58 <math>\pm</math> 3.13</b>
60	10 $\pm$ 0	10 $\pm$ 0	10 $\pm$ 0				
70	10 $\pm$ 0	10 $\pm$ 0	10 $\pm$ 0				
80	10 $\pm$ 0	10 $\pm$ 0	10 $\pm$ 0				
90	10 $\pm$ 0	10 $\pm$ 0	10 $\pm$ 0				

1701 Table 12 shows the classification accuracy of Diehl&Cook2015 with the benchmarks and proposed  
1702 mechanism under SAFs. We set the number of time steps to 250 and the number of fragments to  
1703 2. The model obtains the first fragment repeatedly during the first 125 time steps and the second  
1704 fragment during the second 125 time steps. We apply this setting to Diehl&Cook2015 since it cannot  
1705 classify data samples as accurately as SNN models with supervised learning (Diehl & Cook, 2015).  
1706 We exclude ECOC from the experiment due to its implementation difficulty in STDP-based SNN  
1707 models. This is because it is not available in Diehl&Cook since it disturbs the Winner-Takes-All  
1708 (WTA) mechanism in Diehl&Cook2015 (Lee & Lim, 2024). As presented in the table, the model with  
1709 our mechanism has the highest accuracy under SAFs. This is because our mechanism can mitigate the  
1710 adversarial effects of hardware faults for the following reasons. Hardware faults excessively increase  
1711 the absolute value of membrane potential (pre-activation in SNN using gradient-based learning rules),  
1712 and this unnatural increase causes the over-firing of spiking neurons of the Diehl&Cook2015 (Putra  
1713 et al., 2022; Han et al., 2023; Rastogi et al., 2021). When faulty Diehl&Cook2015 obtains the whole  
1714 data samples that are not fragmented, fault-injected neurons’ membrane potential always increases or  
1715 decreases significantly, preventing the neurons from spiking properly since the pixel values easily  
1716 enter the fault-injected synapses. We divide the input samples into small pieces by considering  
1717 the complexity of the input samples and the influence of faults to minimize the adversarial effects  
1718 of faults and prevent neurons from over- or under-firing. Through fragmentation, the proposed  
1719 mechanism reduces the probability that the input pixels enter faulty synapses, and the neurons’  
1720 membrane potential avoids increasing or decreasing abnormally. Interestingly, the astrocyte-based  
1721 approaches show high fault mitigation ability integrated with Diehl&Cook2015. This is because they  
1722 aim to improve the fault tolerance of SNN models using STDP (Han et al., 2023; Yunusoglu et al.,  
1723 2025).

1724  
1725  
1726  
1727

1728 B.8 EVALUATIONS WITH REAL FPGA HARDWARE  
1729

1730 We implement the MLP SNN model on a real FPGA device (AMD Virtex UltraScale+ HBM VU47P  
1731 of Amazon F2 instance) with **SpikerPlus**, which is a powerful library to convert Python scripts for  
1732 SNNs to VHSIC Hardware Description Language (VHDL) (Carpegna et al., 2024). We choose the  
1733 FPGA device for SNN implementation because FPGAs are necessary devices to develop hardware-  
1734 based SNN models (Karamimanesh et al., 2025). Due to circuit-level limitations, current FPGA-based  
1735 SNN models do not support on-chip training (Carpegna et al., 2024; Tao et al., 2020). Thus, we train  
1736 the fault-injected SNN model in a software environment with a Graphics Processing Unit (GPU),  
1737 saving the trained weights, and convert the Python script of the software-based models to the VHDL  
1738 script. Then, we synthesize the FPGA circuit with Xilinx Vivado and Amazon FPGA Image (AFI),  
1739 which is widely used for handling FPGAs on Amazon F2 instances. We build the SNN models on  
1740 the FPGA chip and the proposed mechanism on the additional control processor connected to the  
1741 FPGA chip. We set the bit-width for the membrane potential and the synaptic weights of the FPGA  
1742 device to 8 and 6, respectively. We set the floating-point precision of the input data samples to 32.  
1743 We select this setting, referring to the setting of real hardware (BrainChipInc, 2025). Other settings  
1744 are the same as the settings in Subsection 6.1.

1744 **Table 13:** The FPGA-based MLP SNNs’ classification accuracy in a 95% confidence interval using MNIST,  
1745 FMNIST, UCI-HAR, and AudioMNIST with 2 time steps under SAFs. Note that we adopt 2 time steps for  
1746 training. For inference, we use 100 cycles to process data in the FPGA device.

FAULT RATIO(%)	BASELINE	ECOC	SOFTSNN	ROUTING	ASTROCYTE	FALVOLT	LIFA	PROPOSED
ACCURACY (%) WITH HARDWARE-IMPLEMENTED MLP (MNIST)								
0	94.36 $\pm$ 0.52	93.86 $\pm$ 0.66	94.56 $\pm$ 0.63	94.34 $\pm$ 0.71	94.06 $\pm$ 0.68	93.92 $\pm$ 0.79	93.98 $\pm$ 0.85	<b>94.59 <math>\pm</math> 0.65</b>
10	93.18 $\pm$ 1.29	90.94 $\pm$ 2.35	93.29 $\pm$ 1.56	93.58 $\pm$ 1.9	93.26 $\pm$ 1.44	92.69 $\pm$ 1.62	92.59 $\pm$ 1.74	<b>94.01 <math>\pm</math> 1.41</b>
20	11.35 $\pm$ 0	88.11 $\pm$ 2.74	9.8 $\pm$ 0	9.8 $\pm$ 0	10.1 $\pm$ 1.05	89.97 $\pm$ 2.69	15.92 $\pm$ 5.31	<b>91.14 <math>\pm</math> 2.03</b>
30	10.82 $\pm$ 0	11.35 $\pm$ 0	9.8 $\pm$ 0	9.8 $\pm$ 0	10.82 $\pm$ 0	9.8 $\pm$ 0	9.8 $\pm$ 0	<b>90.57 <math>\pm</math> 3.16</b>
40	9.8 $\pm$ 0	9.8 $\pm$ 0	9.8 $\pm$ 0	11.35 $\pm$ 0	9.8 $\pm$ 0	9.8 $\pm$ 0	9.8 $\pm$ 0	<b>80.49 <math>\pm</math> 6.65</b>
50	9.8 $\pm$ 0	9.8 $\pm$ 0	9.8 $\pm$ 0	11.35 $\pm$ 0	9.8 $\pm$ 0	9.8 $\pm$ 0	9.8 $\pm$ 0	<b>21.46 <math>\pm</math> 4.72</b>
60	9.8 $\pm$ 0	9.8 $\pm$ 0	9.8 $\pm$ 0	9.8 $\pm$ 0	9.8 $\pm$ 0	9.8 $\pm$ 0	9.8 $\pm$ 0	9.8 $\pm$ 0
70	9.8 $\pm$ 0	9.8 $\pm$ 0	9.8 $\pm$ 0	9.8 $\pm$ 0	9.8 $\pm$ 0	9.8 $\pm$ 0	9.8 $\pm$ 0	9.8 $\pm$ 0
80	9.8 $\pm$ 0	9.8 $\pm$ 0	9.8 $\pm$ 0	9.8 $\pm$ 0	9.8 $\pm$ 0	9.8 $\pm$ 0	9.8 $\pm$ 0	9.8 $\pm$ 0
90	9.8 $\pm$ 0	9.8 $\pm$ 0	9.8 $\pm$ 0	9.8 $\pm$ 0	9.8 $\pm$ 0	9.8 $\pm$ 0	9.8 $\pm$ 0	9.8 $\pm$ 0
ACCURACY (%) WITH HARDWARE-IMPLEMENTED MLP (FMNIST)								
0	84.21 $\pm$ 1.79	83.58 $\pm$ 1.91	83.65 $\pm$ 2.13	84.19 $\pm$ 1.82	83.9 $\pm$ 1.75	83.97 $\pm$ 1.68	84.1 $\pm$ 1.58	<b>87.01 <math>\pm</math> 1.45</b>
10	82.16 $\pm$ 2.28	82.75 $\pm$ 2.46	80.74 $\pm$ 2.67	83.58 $\pm$ 2.33	82.86 $\pm$ 2.09	83.11 $\pm$ 2.53	82.46 $\pm$ 2.38	<b>86.14 <math>\pm</math> 2.84</b>
20	79.6 $\pm$ 3.05	10 $\pm$ 0	10 $\pm$ 0	10 $\pm$ 0	10 $\pm$ 0	82.54 $\pm$ 3.18	17.26 $\pm$ 5.98	<b>83.98 <math>\pm</math> 3.27</b>
30	10 $\pm$ 0	10 $\pm$ 0	10 $\pm$ 0	10 $\pm$ 0	10 $\pm$ 0	10 $\pm$ 0	10 $\pm$ 0	<b>81.71 <math>\pm</math> 3.7</b>
40	10 $\pm$ 0	10 $\pm$ 0	10 $\pm$ 0	10 $\pm$ 0	10 $\pm$ 0	10 $\pm$ 0	10 $\pm$ 0	<b>52.75 <math>\pm</math> 4.89</b>
50	10 $\pm$ 0	10 $\pm$ 0	10 $\pm$ 0	10 $\pm$ 0	10 $\pm$ 0	10 $\pm$ 0	10 $\pm$ 0	10 $\pm$ 0
60	10 $\pm$ 0	10 $\pm$ 0	10 $\pm$ 0	10 $\pm$ 0	10 $\pm$ 0	10 $\pm$ 0	10 $\pm$ 0	10 $\pm$ 0
70	10 $\pm$ 0	10 $\pm$ 0	10 $\pm$ 0	10 $\pm$ 0	10 $\pm$ 0	10 $\pm$ 0	10 $\pm$ 0	10 $\pm$ 0
80	10 $\pm$ 0	10 $\pm$ 0	10 $\pm$ 0	10 $\pm$ 0	10 $\pm$ 0	10 $\pm$ 0	10 $\pm$ 0	10 $\pm$ 0
90	10 $\pm$ 0	10 $\pm$ 0	10 $\pm$ 0	10 $\pm$ 0	10 $\pm$ 0	10 $\pm$ 0	10 $\pm$ 0	10 $\pm$ 0
ACCURACY (%) WITH HARDWARE-IMPLEMENTED MLP (UCI-HAR)								
0	60.14 $\pm$ 3.87	<b>65.27 <math>\pm</math> 3.56</b>	60.48 $\pm$ 3.81	61.15 $\pm$ 3.69	61.78 $\pm$ 3.48	61.83 $\pm$ 3.45	61.52 $\pm$ 3.62	60.08 $\pm$ 3.24
10	17.1 $\pm$ 0	17.1 $\pm$ 0	15.21 $\pm$ 0	17.1 $\pm$ 0	15.21 $\pm$ 0	18.34 $\pm$ 0	16.93 $\pm$ 0	<b>47.01 <math>\pm</math> 5.17</b>
20	18.52 $\pm$ 0	17.1 $\pm$ 0	18.52 $\pm$ 0	17.1 $\pm$ 0	18.52 $\pm$ 0	18.34 $\pm$ 0	17.1 $\pm$ 0	<b>45.85 <math>\pm</math> 5.39</b>
30	17.1 $\pm$ 0	17.1 $\pm$ 0	17.1 $\pm$ 0	17.1 $\pm$ 0	17.1 $\pm$ 0	18.34 $\pm$ 0	17.1 $\pm$ 0	<b>44.86 <math>\pm</math> 4.91</b>
40	17.1 $\pm$ 0	17.1 $\pm$ 0	17.1 $\pm$ 0	17.1 $\pm$ 0	17.1 $\pm$ 0	16.93 $\pm$ 0	17.1 $\pm$ 0	17.1 $\pm$ 0
50	17.1 $\pm$ 0	17.1 $\pm$ 0	17.1 $\pm$ 0	17.1 $\pm$ 0	17.1 $\pm$ 0	16.93 $\pm$ 0	17.1 $\pm$ 0	17.1 $\pm$ 0
60	17.1 $\pm$ 0	17.1 $\pm$ 0	17.1 $\pm$ 0	17.1 $\pm$ 0	17.1 $\pm$ 0	16.93 $\pm$ 0	17.1 $\pm$ 0	17.1 $\pm$ 0
70	17.1 $\pm$ 0	17.1 $\pm$ 0	17.1 $\pm$ 0	17.1 $\pm$ 0	17.1 $\pm$ 0	16.93 $\pm$ 0	17.1 $\pm$ 0	17.1 $\pm$ 0
80	17.1 $\pm$ 0	17.1 $\pm$ 0	17.1 $\pm$ 0	17.1 $\pm$ 0	17.1 $\pm$ 0	16.93 $\pm$ 0	17.1 $\pm$ 0	17.1 $\pm$ 0
90	17.1 $\pm$ 0	17.1 $\pm$ 0	17.1 $\pm$ 0	17.1 $\pm$ 0	17.1 $\pm$ 0	16.93 $\pm$ 0	17.1 $\pm$ 0	17.1 $\pm$ 0
ACCURACY (%) WITH HARDWARE-IMPLEMENTED MLP (AUDIOMNIST)								
0	93.76 $\pm$ 1.34	<b>93.82 <math>\pm</math> 1.6</b>	92.02 $\pm$ 1.66	92.63 $\pm$ 1.21	92.36 $\pm$ 1.53	91.38 $\pm$ 1.27	93.33 $\pm$ 1.29	92.34 $\pm$ 1.38
10	91.80 $\pm$ 1.22	90.89 $\pm$ 2.12	89.32 $\pm$ 2.01	89.87 $\pm$ 2.22	90.01 $\pm$ 2.45	90.71 $\pm$ 2.45	90.41 $\pm$ 2.74	<b>91.56 <math>\pm</math> 1.93</b>
20	89.45 $\pm$ 2.1	88.92 $\pm$ 2.56	84.39 $\pm$ 3.41	89.59 $\pm$ 2.50	81.61 $\pm$ 3.81	89.42 $\pm$ 2.68	84.47 $\pm$ 4.79	<b>90.86 <math>\pm</math> 2.83</b>
30	89.04 $\pm$ 2.44	89.65 $\pm$ 2.77	72.35 $\pm$ 3.93	88.19 $\pm$ 3.28	48.31 $\pm$ 5.73	89.57 $\pm$ 3.01	51.64 $\pm$ 6.53	<b>89.8 <math>\pm</math> 3.42</b>
40	86.24 $\pm$ 3.59	90.26 $\pm$ 2.58	59.43 $\pm$ 5.48	87.99 $\pm$ 3.97	34.69 $\pm$ 6.61	87.8 $\pm$ 3.42	35.73 $\pm$ 7.49	<b>89.27 <math>\pm</math> 4.13</b>
50	83.50 $\pm$ 4.63	82.63 $\pm$ 4.43	45.26 $\pm$ 7.31	82.39 $\pm$ 4.42	19.38 $\pm$ 5.2	83.21 $\pm$ 4.93	21.22 $\pm$ 5.56	<b>86.29 <math>\pm</math> 4.9</b>
60	49.11 $\pm$ 6.32	62.20 $\pm$ 5.82	31.23 $\pm$ 5.78	61.16 $\pm$ 5.94	10 $\pm$ 0	62.48 $\pm$ 6.63	10 $\pm$ 0	<b>63.88 <math>\pm</math> 6.34</b>
70	10 $\pm$ 0	16.74 $\pm$ 2.45	10 $\pm$ 0	21.92 $\pm$ 3.84	10 $\pm$ 0	24.72 $\pm$ 4.47	10 $\pm$ 0	<b>34.75 <math>\pm</math> 3.76</b>
80	10 $\pm$ 0	10 $\pm$ 0	10 $\pm$ 0	10 $\pm$ 0	10 $\pm$ 0	13.15 $\pm$ 2.14	10 $\pm$ 0	<b>17.29 <math>\pm</math> 3.55</b>
90	10 $\pm$ 0	10 $\pm$ 0	10 $\pm$ 0	10 $\pm$ 0	10 $\pm$ 0	10 $\pm$ 0	10 $\pm$ 0	10 $\pm$ 0

1776 **Table 13** presents the classification accuracy of the MLP model, along with the baseline, benchmarks,  
1777 and our mechanism, under SAFs, using the MNIST, FMNIST, UCI-HAR, and AudioMNIST. The  
1778 model incorporating our mechanism classifies the data samples more accurately than the baseline and  
1779 benchmarks when implemented with hardware. We observe that the overall classification accuracy of  
1780 the model decreases. This is because the precision for neurons’ membrane potential and synaptic  
1781 weights degrades due to low floating-point and bit width in the FPGA device, which damages the  
data stored in trained synaptic weights and neuronal activities.

We implement VGG-7/11/15 with the SyncNN framework and evaluate the fault tolerance of the benchmarks and proposed mechanism (Panchapakesan et al., 2021). We set the bit-width for synaptic weights to 8. Other settings for SyncNN are the same as the settings in the SyncNN paper (Panchapakesan et al., 2021). We adopt the same SNN model settings in Subsection 6.1 to the FPGA-based VGG models.

**Table 14:** The FPGA-based VGG-7/11/15 SNNs’ classification accuracy in a 95% confidence interval using CIFAR-10 with 2 time steps under SAFs. Note that we adopt 2 time steps for training. For inference, we use 1800 cycles to process data in the FPGA device.

FAULT RATIO(%)	BASELINE	ECOC	SOFTSNN	ROUTING	ASTROCYTE	FALVOLT	LIFA	PROPOSED
ACCURACY (%) WITH HARDWARE-IMPLEMENTED VGG-7								
0	53.84 $\pm$ 4.94	51.09 $\pm$ 4.86	54.08 $\pm$ 4.67	<b>54.15 <math>\pm</math> 4.26</b>	53.21 $\pm$ 4.6	53.91 $\pm$ 4.57	52.72 $\pm$ 4.65	53.89 $\pm$ 4.48
10	34.18 $\pm$ 4.15	39.26 $\pm$ 4.07	22.48 $\pm$ 4.46	33.37 $\pm$ 4.12	32.16 $\pm$ 4.54	36.92 $\pm$ 4.82	35.38 $\pm$ 4.73	<b>45.93 <math>\pm</math> 4.31</b>
20	18.73 $\pm$ 3.07	31.97 $\pm$ 3.65	17.52 $\pm$ 5.11	24.06 $\pm$ 3.71	22.18 $\pm$ 3.95	31.91 $\pm$ 3.79	21.99 $\pm$ 4.02	<b>41.23 <math>\pm</math> 4.05</b>
30	11.62 $\pm$ 1.62	25.78 $\pm$ 3.14	16.8 $\pm$ 3.92	10 $\pm$ 0	10 $\pm$ 0	20.7 $\pm$ 4.15	10 $\pm$ 0	<b>35.97 <math>\pm</math> 4.88</b>
40	10 $\pm$ 0	19.29 $\pm$ 3.28	15.04 $\pm$ 3.17	10 $\pm$ 0	10 $\pm$ 0	17.28 $\pm$ 3.84	10 $\pm$ 0	<b>26.29 <math>\pm</math> 3.96</b>
50	10 $\pm$ 0	12.81 $\pm$ 2.25	10 $\pm$ 0	10 $\pm$ 0	10 $\pm$ 0	10 $\pm$ 0	10 $\pm$ 0	<b>13.39 <math>\pm</math> 2.94</b>
60	10 $\pm$ 0	10 $\pm$ 0	10 $\pm$ 0	10 $\pm$ 0	10 $\pm$ 0	10 $\pm$ 0	10 $\pm$ 0	10 $\pm$ 0
70	10 $\pm$ 0	10 $\pm$ 0	10 $\pm$ 0	10 $\pm$ 0	10 $\pm$ 0	10 $\pm$ 0	10 $\pm$ 0	10 $\pm$ 0
80	10 $\pm$ 0	10 $\pm$ 0	10 $\pm$ 0	10 $\pm$ 0	10 $\pm$ 0	10 $\pm$ 0	10 $\pm$ 0	10 $\pm$ 0
90	10 $\pm$ 0	10 $\pm$ 0	10 $\pm$ 0	10 $\pm$ 0	10 $\pm$ 0	10 $\pm$ 0	10 $\pm$ 0	10 $\pm$ 0
ACCURACY (%) WITH HARDWARE-IMPLEMENTED VGG-11								
0	52.74 $\pm$ 4.63	50.34 $\pm$ 4.51	<b>54.82 <math>\pm</math> 4.32</b>	54.29 $\pm$ 4.45	52.13 $\pm$ 4.63	53.89 $\pm$ 4.38	53.02 $\pm$ 4.47	52.87 $\pm$ 4.2
10	33.27 $\pm$ 3.95	33.02 $\pm$ 3.84	26.53 $\pm$ 3.72	32.98 $\pm$ 3.93	34.16 $\pm$ 4.05	41.81 $\pm$ 4.24	35.57 $\pm$ 4.13	<b>45.02 <math>\pm</math> 4.08</b>
20	26.91 $\pm$ 3.28	30.83 $\pm$ 3.37	18.88 $\pm$ 3.6	24.17 $\pm$ 3.56	24.93 $\pm$ 3.75	27.3 $\pm$ 3.43	24.89 $\pm$ 3.94	<b>42.58 <math>\pm</math> 3.79</b>
30	10 $\pm$ 0	25.65 $\pm$ 3.51	17.63 $\pm$ 3.92	10 $\pm$ 0	16.89 $\pm$ 3.81	10 $\pm$ 0	11.46 $\pm$ 1.46	<b>36.62 <math>\pm</math> 3.84</b>
40	10 $\pm$ 0	20.27 $\pm$ 3.64	10 $\pm$ 0	10 $\pm$ 0	10 $\pm$ 0	10 $\pm$ 0	10 $\pm$ 0	<b>26.84 <math>\pm</math> 3.29</b>
50	10 $\pm$ 0	14.44 $\pm$ 3.76	10 $\pm$ 0	10 $\pm$ 0	10 $\pm$ 0	10 $\pm$ 0	10 $\pm$ 0	<b>17.92 <math>\pm</math> 3.65</b>
60	10 $\pm$ 0	10 $\pm$ 0	10 $\pm$ 0	10 $\pm$ 0	10 $\pm$ 0	10 $\pm$ 0	10 $\pm$ 0	10 $\pm$ 0
70	10 $\pm$ 0	10 $\pm$ 0	10 $\pm$ 0	10 $\pm$ 0	10 $\pm$ 0	10 $\pm$ 0	10 $\pm$ 0	10 $\pm$ 0
80	10 $\pm$ 0	10 $\pm$ 0	10 $\pm$ 0	10 $\pm$ 0	10 $\pm$ 0	10 $\pm$ 0	10 $\pm$ 0	10 $\pm$ 0
90	10 $\pm$ 0	10 $\pm$ 0	10 $\pm$ 0	10 $\pm$ 0	10 $\pm$ 0	10 $\pm$ 0	10 $\pm$ 0	10 $\pm$ 0
ACCURACY (%) WITH HARDWARE-IMPLEMENTED VGG-15								
0	45.04 $\pm$ 4.07	41.92 $\pm$ 3.95	<b>47.39 <math>\pm</math> 3.81</b>	43.58 $\pm$ 3.86	43.02 $\pm$ 3.77	45.58 $\pm$ 3.26	44.61 $\pm$ 3.74	44.35 $\pm$ 4.61
10	40.16 $\pm$ 5.24	31.19 $\pm$ 4.76	14.21 $\pm$ 1.91	41.5 $\pm$ 4.83	32.28 $\pm$ 5.13	41.87 $\pm$ 4.59	29.84 $\pm$ 5.33	<b>42.94 <math>\pm</math> 5.09</b>
20	21.42 $\pm$ 4.64	23.7 $\pm$ 4.59	13.22 $\pm$ 2.08	25.28 $\pm$ 4.29	10 $\pm$ 0	10 $\pm$ 0	20.37 $\pm$ 3.91	<b>41.47 <math>\pm</math> 4.96</b>
30	10 $\pm$ 0	21.26 $\pm$ 3.54	12.89 $\pm$ 1.75	10 $\pm$ 0	10 $\pm$ 0	10 $\pm$ 0	10 $\pm$ 0	<b>33.62 <math>\pm</math> 5.17</b>
40	10 $\pm$ 0	15.28 $\pm$ 2.94	11.01 $\pm$ 1.01	10 $\pm$ 0	10 $\pm$ 0	10 $\pm$ 0	10 $\pm$ 0	<b>27.59 <math>\pm</math> 4.25</b>
50	10 $\pm$ 0	10 $\pm$ 0	10 $\pm$ 0	10 $\pm$ 0	10 $\pm$ 0	10 $\pm$ 0	10 $\pm$ 0	<b>11.74 <math>\pm</math> 1.19</b>
60	10 $\pm$ 0	10 $\pm$ 0	10 $\pm$ 0	10 $\pm$ 0	10 $\pm$ 0	10 $\pm$ 0	10 $\pm$ 0	10 $\pm$ 0
70	10 $\pm$ 0	10 $\pm$ 0	10 $\pm$ 0	10 $\pm$ 0	10 $\pm$ 0	10 $\pm$ 0	10 $\pm$ 0	10 $\pm$ 0
80	10 $\pm$ 0	10 $\pm$ 0	10 $\pm$ 0	10 $\pm$ 0	10 $\pm$ 0	10 $\pm$ 0	10 $\pm$ 0	10 $\pm$ 0
90	10 $\pm$ 0	10 $\pm$ 0	10 $\pm$ 0	10 $\pm$ 0	10 $\pm$ 0	10 $\pm$ 0	10 $\pm$ 0	10 $\pm$ 0

Table 14 exhibits the classification accuracy of the VGG-7/11/15 models, along with the baseline, benchmarks, and proposed mechanism under SAFs, using CIFAR-10. In the cases with deep convolution SNNs, our mechanism successfully enhances the fault tolerance of hardware-implemented SNNs based on the FPGA device.

1812  
1813  
1814  
1815  
1816  
1817  
1818  
1819  
1820  
1821  
1822  
1823  
1824  
1825  
1826  
1827  
1828  
1829  
1830  
1831  
1832  
1833  
1834  
1835

1836 **C EFFICIENCY ANALYSIS BASED ON TIME/SPATIAL COMPLEXITY AND**  
 1837 **TIME/ENERGY CONSUMPTION**  
 1838

1839 To demonstrate that our mechanism enhances the fault tolerance of SNN models without requiring  
 1840 complex algorithms, we measure the computational and spatial complexities of our mechanism and  
 1841 compare them to those of the benchmarks. Additionally, we measure the energy consumption of our  
 1842 mechanisms on the FPGA device since energy consumption is a significant advantage of SNNs that  
 1843 makes them suitable for neuromorphic device implementation.

1845 **C.1 COMPLEXITY ANALYSIS**  
 1846

1847 We calculate the time and spatial complexities of the benchmarks and the proposed mechanism  
 1848 through experimental evidence that demonstrates the time and energy consumption of them in real  
 1849 devices.

1850 **C.1.1 TIME COMPLEXITY**  
 1851

1852 We thoroughly analyze the time complexity of the benchmarks and the proposed mechanism. The  
 1853 following items present the time complexity of the benchmarks and the proposed mechanism.

1. **ECOC:**  $T_{\text{ECOC}} = \Theta(EP^2n + NBCL)$ .
2. **SoftSNN:**  $T_{\text{SoftSNN}} = \Theta(NW)$ .
3. **Routing:**  $T_{\text{route}} = \Theta\left(\sum_{\ell=1}^L C_{\text{out}}^{(\ell)} C_{\text{in}}^{(\ell)} k_{\ell}^2 + \delta_{\text{swap}} \sum_{\ell=1}^L K_{\ell} \log K_{\ell}\right)$ .
4. **Astrocyte:**  $T_{\text{Astro}} = \Theta(P + NP)$ .
5. **FalVolt:**  $T_{\text{FalVolt}} = \Theta(M + N(M + fW))$ .
6. **LIFA:**  $T_{\text{LIFA}} = \Theta(P + NP)$ .
7. **Proposed:**  $T_{\text{proposed, mlp}} = \Theta(NS[B + A + T + BTD]) + O(N_{\text{sal}} F_{\text{model}}^{\text{MLP}})$ ,  
 $T_{\text{proposed, conv}} = \Theta(NS[B + A + T + BTD])$ .

1869 **Notations of time complexity equations**  
 1870

1. **ECOC.**  $B$ : batch size;  $N$ : number of training/inference steps (batches processed);  $C$ : number of classes;  $E$ : number of extension code blocks;  $m$ : Hamming-code parameter;  $n = 2^m - 1$ : per code block length;  $L = E n$ : code length;  $P$ : candidate-pool size used in code book construction.
2. **Soft SNN.**  $W = \sum_{i=1}^M P_i$ : total number of trainable weights over the  $M$  layers;  $P_i$ : number of weights in layer  $i$ ;  $P_{\text{max}} = \max_i P_i$ : size of the largest layer.
3. **Routing.**  $L_{\text{layers}}$ : number of routed layers;  $C_{\text{in}}^{(\ell)}, C_{\text{out}}^{(\ell)}$ : input/output channels of layer  $\ell$ ;  $k_{\ell}$ : kernel size of layer  $\ell$  (so  $k_{\ell}^2 = 1$  for MLP/Linear);  $K_{\ell} = \min\{C_{\text{in}}^{(\ell)}, C_{\text{out}}^{(\ell)}\}$ : effective channel count for top- $K$  matching;  $\delta_{\text{swap}} \in \{0, 1\}$ : flag indicating whether sorting + channel-swap is enabled;  $W$ : total number of trainable weights across routed layers.
4. **Astrocyte.**  $N$ : number of batch iterations in an epoch;  $P$ : total number of trainable parameters over hooked layers;  $\chi$ : output-channel chunk size used in the backward pass;  $p_{\text{out}}^{\text{max}}$ : maximum number of parameters associated with a single output channel (e.g.,  $9 C_{\text{in}}$  for a  $3 \times 3$  conv).
5. **FalVolt.**  $N$ : number of batch iterations in an epoch;  $W$ : total number of weights subject to potential fault mapping;  $M$ : number of spiking/protected modules whose thresholds or states are managed;  $f \in [0, 1]$ : fraction of weights affected by faults (worst case  $f = 1$ );  $W_{\text{mask}}$ : number of stored fault-mask entries.

1890 6. **LIFA.**  $N$ : number of batch iterations in an epoch;  $P$ : total number of trainable parameters  
 1891 across protected layers (for conv:  $P = \sum_{\ell} C_{\text{out}}^{(\ell)} C_{\text{in}}^{(\ell)} k_{\ell}^2$ ; for linear:  $k_{\ell}^2 = 1$ );  $C =$   
 1892  $\sum_{\ell} C_{\text{out}}^{(\ell)}$ : total output-channel count across protected layers.  
 1893

1894 7. **Proposed.**  $N$ : number of batch iterations in an epoch;  $S = H \times W$ : spatial size  
 1895 (pixels) per sample;  $B$ : batch size;  $D$ : input channels;  $T$ : number of time steps  
 1896 (fragments) per sample;  $A$ : number of orientation candidates; (*optional only if the fault*  
 1897 *influence map (saliency and weight projection) is used*)  $N_{\text{sal}}$ : number of steps that compute  
 1898 saliency/backprop;  $F_{\text{model}}^{\text{MLP}}$ : per-step FLOPs of the MLP backbone under saliency.

1899 With MNIST and FMNIST ( $S = 28 \times 28 = 784$ ,  $D = 1$ ), our fragmentation step scales as  
 1900

$$T_{\text{proposed}} = \Theta(S B T) = \Theta(784 B T), \quad (5)$$

1903 while all weight-scanning benchmarks (Astrocyte and LIFA) based on astrocytes scale with the  
 1904 number of parameters:  
 1905

$$T_{\text{scan}} = \Theta(W), \quad T_{\text{FalVolt}} = \Theta(M + fW) \asymp \Theta(fW) \quad (\text{for non-vanishing } f), \quad (6)$$

1908 where  $W$  is the total trainable weights,  $M$  the number of spiking/protected modules, and  $f \in [0, 1]$   
 1909 the fraction of weights affected by faults. Hence, the decisive ratios are  
 1910

$$\frac{T_{\text{proposed}}}{T_{\text{scan}}} \asymp \frac{784 B T}{W}, \quad \frac{T_{\text{proposed}}}{T_{\text{FalVolt}}} \asymp \frac{784 B T}{f W}. \quad (7)$$

1913 For the CNNs in our setting (VGG-7/11/15, ResNet-18),  $W$  is in the multi-million range even on  
 1914 MNIST/FMNIST; with common batches/fragments ( $B \in [64, 128]$ ,  $T \in [2, 4]$ ) one has  $W \gg 784 B T$ ,  
 1915 so strictly  $T_{\text{proposed}} < T_{\text{scanning}}$ . The same conclusion holds against FalVolt for any fixed, non-negligible  
 1916  $f$  (e.g.,  $f \geq 0.05$ ), since then  $fW \gg 784 B T$  in these networks, yielding  $T_{\text{ours}} < T_{\text{FalVolt}}$  as well.  
 1917 ECOC differs in that its per-step cost is  $T_{\text{ECOC}} = \Theta(B C L)$ , giving  
 1918

$$\frac{T_{\text{proposed}}}{T_{\text{ECOC}}} \asymp \frac{S T D}{C L} = \frac{784 T}{C L}, \quad (8)$$

1922 which is typically of the same order for  $C=10$  and  $L \in [64, 256]$ , while ECOC still incurs a one-off  
 1923 build of  $\Theta(E P^2 n)$ . In summary, without the fault influence, our mechanism has strictly smaller  
 1924 per-step time complexity than all weight-scanning benchmarks under the MLP/VGG/ResNet models.  
 1925 It is competitive with (or smaller than) ECOC while avoiding the heavy one-time construction of  
 1926 ECOC. As shown in Appendix A.1 and A.2, our mechanism is not significantly dependent on the  
 1927 fault influence with CIFAR-10 and CIFAR-100 under VGG and ResNet models, indicating that our  
 1928 mechanism saves time by using only the complexity to make fragments under VGG and ResNet  
 1929 models with CIFAR-10 and CIFAR-100.  
 1930

### C.1.2 SPATIAL COMPLEXITY

1932 We evaluate the spatial complexity of the benchmarks and the proposed mechanism in detail. The  
 1933 following items present the spatial complexity of the benchmarks and the proposed mechanism  
 1934

1. **ECOC:**  $S_{\text{ECOC}} = \Theta(P^2 + CL + BC)$ .
2. **SoftSNN:**  $S_{\text{SoftSNN}} = \Theta(W)$ .
3. **Routing:**  $S_{\text{route}} = \Theta(W)$ .
4. **Astrocyte:**  $S_{\text{Astro}} = \Theta(P + \chi p_{\text{out}}^{\max})$ .
5. **FalVolt:**  $S_{\text{FalVolt}} = \Theta(M + W_{\text{mask}})$ .
6. **LIFA:**  $S_{\text{LIFA}} = \Theta(P + C)$ .
7. **Proposed:**  $S_{\text{proposed}} = \Theta(S [ BTD + A ])$ .

1944

## Notations of spatial complexity equations

1945

1946

1947

1948

1949

1950

1951

1952

1953

1954

1955

1956

1957

1958

1959

1960

1961

1962

1963

1964

1965

1966

1967

1968

1969

1970

1971

1972

1973

1974

1975

1976

1977

1978

1979

1980

1981

1982

1983

1984

1985

1986

1987

1988

1989

1990

1991

1992

1993

1994

1995

1996

1997

1998

1999

2000

2001

2002

2003

2004

2005

2006

2007

2008

2009

2010

2011

2012

2013

2014

2015

2016

2017

2018

2019

2020

2021

2022

2023

2024

2025

2026

2027

2028

2029

2030

2031

2032

2033

2034

2035

2036

2037

2038

2039

2040

2041

2042

2043

2044

2045

2046

2047

2048

2049

2050

2051

2052

2053

2054

2055

2056

2057

2058

2059

2060

2061

2062

2063

2064

2065

2066

2067

2068

2069

2070

2071

2072

2073

2074

2075

2076

2077

2078

2079

2080

2081

2082

2083

2084

2085

2086

2087

2088

2089

2090

2091

2092

2093

2094

2095

2096

2097

2098

2099

20100

20111

20122

20133

20144

20155

20166

20177

20188

20190

20192

20194

20196

20198

20199

20200

20201

20202

20203

20204

20205

20206

20207

20208

20209

20210

20211

20212

20213

20214

20215

20216

20217

20218

20219

20220

20221

20222

20223

20224

20225

20226

20227

20228

20229

20230

20231

20232

20233

20234

20235

20236

20237

20238

20239

20240

20241

20242

20243

20244

20245

20246

20247

20248

20249

20250

20251

20252

20253

20254

20255

20256

20257

20258

20259

20260

20261

20262

20263

20264

20265

20266

20267

20268

20269

20270

20271

20272

20273

20274

20275

20276

20277

20278

20279

20280

20281

20282

20283

20284

20285

20286

20287

20288

20289

20290

20291

20292

20293

20294

20295

20296

20297

20298

20299

20300

20301

20302

20303

20304

20305

20306

20307

20308

20309

20310

20311

20312

20313

20314

20315

20316

20317

20318

20319

20320

20321

20322

20323

20324

20325

20326

20327

20328

20329

20330

20331

20332

20333

20334

20335

20336

20337

20338

20339

20340

20341

20342

20343

20344

20345

20346

20347

20348

20349

20350

1998  
1999

## C.2 TRAINING TIME

2000 We measure the training time of the baseline, benchmarks, and the proposed mechanism using the  
 2001 MLP (MNIST), VGG-7 (CIFAR-10), ResNet-18 (CIFAR-100), and ResNet-34 (Tiny-ImageNet)  
 2002 models with 2 time steps. We train the models on a workstation with an Nvidia GeForce RTX 4080  
 2003 GPU with Ubuntu 24.04.

2004 **Table 15:** Various models’ training time (sec) in a 95% confidence interval with the baseline, benchmarks, and  
 2005 proposed mechanism on a workstation under SAFs with a fault ratio of 0.5 and 2 time steps.

	Baseline	ECOC	SoftSNN	Routing	Astrocyte	FalVolt	LIFA	Proposed
MLP	<b>193.84 ± 2.71</b>	197.62 ± 2.85	196.51 ± 2.56	198.29 ± 3.05	288.75 ± 4.51	201.47 ± 3.21	293.86 ± 4.77	205.24 ± 4.23
VGG-7	<b>291.16 ± 3.57</b>	296.91 ± 3.8	294.34 ± 3.65	298.81 ± 4.01	351.82 ± 5.27	303.53 ± 4.26	356.74 ± 5.53	310.38 ± 5.18
ResNet-18	<b>382.53 ± 4.12</b>	385.61 ± 4.03	384.77 ± 4.53	396.54 ± 4.68	721.97 ± 6.28	408.9 ± 4.94	724.62 ± 6.09	413.32 ± 4.5
ResNet-34	<b>4259.57 ± 18.62</b>	4304.4 ± 20.11	4298.46 ± 21.39	4350.83 ± 25.75	8005.37 ± 36.21	4317.89 ± 26.04	8154.17 ± 32.83	4392.13 ± 26.51

2006 Our mechanism consumes significantly less training time than weight-scanning approaches based on  
 2007 astrocytes (Astrocyte and LIFA), as we demonstrate that our mechanism definitely consumes less  
 2008 time than the astrocyte-based approaches due to their less complexity. Unlike these approaches, the  
 2009 training time of the models with our mechanism does not increase significantly as the complexity of  
 2010 the models and datasets increases. The model with ours also consumes comparable training time to  
 2011 that of ECOC, SoftSNN, Routing, and FalVolt. This evaluation result shows that our mechanism does  
 2012 not severely inflate the burden on training time.

## C.3 ENERGY CONSUMPTION ON THE REAL FPGA DEVICE

2013 We measure the energy consumption of the model with the baseline, benchmarks, and proposed  
 2014 mechanism on the FPGA device during testing. Table 16 exhibits the energy consumption of the  
 2015 FPGA-based MLP with MNIST/FMNIST and FPGA-based VGG-7 with CIFAR-100 using 2 time  
 2016 steps.

2017 **Table 16:** The MLP models’ energy consumption (mJ) to process a single sample in a 95% confidence interval  
 2018 with the baseline, benchmarks, and proposed mechanism on the real FPGA hardware with two time steps.

	Baseline	ECOC	SoftSNN	Routing	Astrocyte	FalVolt	LIFA	Proposed
MNIST	85.31 ± 1.05	88.76 ± 1.27	86.23 ± 1.18	90.44 ± 1.31	150.72 ± 1.61	95.15 ± 1.23	165.69 ± 1.59	<b>67.16 ± 0.82</b>
FMNIST	87.19 ± 1.36	90.54 ± 1.57	88.68 ± 1.43	92.82 ± 1.51	156.08 ± 1.99	98.23 ± 1.72	168.33 ± 1.93	<b>78.37 ± 0.95</b>
CIFAR-10	203.85 ± 2.07	216.41 ± 2.13	212.96 ± 1.97	228.16 ± 2.45	319.5 ± 3.56	209.87 ± 2.92	336.09 ± 3.44	<b>194.14 ± 2.35</b>

2019 The MLP model with our mechanism exhibits the least energy consumption among the MLP models  
 2020 on the real FPGA device. This is because our mechanism shrinks the size of the data samples through  
 2021 fragmentation, and the probability of spike occurrence declines since the number of non-zero pixels  
 2022 decreases during fragmentation, as mentioned in Subsection 5.3. This effect enables the model with  
 2023 our mechanism to consume less energy than the models with all benchmarks, despite our mechanism  
 2024 having higher time complexity and consumption than some benchmarks. However, the benchmarks  
 2025 increase the complexity of the decoding (ECOC), keep neurons’ activation frequent (SoftSNN and  
 2026 Routing), utilize the astrocyte module to activate non-faulty synapses (Astrocyte and LIFA), and  
 2027 incorporate additional learnable parameters to adjust neuronal activities (Falvolt). Therefore, the  
 2028 MLP models with the benchmark require more energy than ours.

2029  
2030  
2031  
2032  
2033  
2034  
2035  
2036  
2037  
2038  
2039  
2040  
2041  
2042  
2043  
2044  
2045  
2046  
2047  
2048  
2049  
2050  
2051

2052 **D DETAILED MATHEMATICAL EXPLANATION OF THE MOTIVATION STUDY**  
 2053

2054 We demonstrate how synaptic faults ruin the usable learning capacity of SNN models mathematically.  
 2055

2056 **D.1 SETUP AND NOTATION**  
 2057

2058 Consider a spiking neuron with membrane potential  $V_t \in \mathbb{R}$ , threshold  $\vartheta \in \mathbb{R}$ , and spike output  
 2059  $K_t \in \{0, 1\}$ . During training, we replace the Heaviside step  $H$  by a surrogate  $\sigma : \mathbb{R} \rightarrow [0, 1]$  so that  
 2060  $K_t \approx \sigma(V_t - \vartheta)$  and  $\sigma'$  is used in backpropagation. Let the *surrogate gradient corridor width* be  
 2061  $\delta > 0$  such that  $\sigma'(u) \approx 0$  whenever  $|u| > \delta$ . For a feedforward pre-activation at layer  $\ell$  and time  $t$ ,  
 2062

2063 
$$z_t^{(\ell)} = W^{(\ell)} K_t^{(\ell-1)} + b^{(\ell)} \quad (\text{vector form}), \quad (14)$$

2064 and for a single neuron with input  $x \in \mathbb{R}^d$  and weights  $w \in \mathbb{R}^d$  we write  $z = w^\top x + b$ . For an LIF  
 2065 neuron, we use  
 2066

2067 
$$V_t = \alpha V_{t-1} + z_t - \vartheta K_{t-1}, \quad K_t \approx \sigma(V_t - \vartheta), \quad \alpha \in (0, 1). \quad (15)$$
  
 2068

2069 **D.2 SURROGATE GRADIENT CORRIDOR**  
 2070

2071 Let  $u := z - \vartheta$ . Many arctangent surrogates used in SNNs have a backward derivative of the rational  
 2072 form  
 2073

2074 
$$\phi'(u) = \frac{A}{1 + (\beta u)^2}, \quad A > 0, \beta > 0, \quad (16)$$
  
 2075

2077 which yields, for a target gradient floor  $\gamma \in (0, A)$ , the corridor  
 2078

2079 
$$\mathcal{C}_\gamma := \{u : \phi'(u) \geq \gamma\} = [-\delta(\gamma), \delta(\gamma)], \quad \delta(\gamma) = \frac{1}{\beta} \sqrt{\frac{A}{\gamma} - 1}. \quad (17)$$
  
 2080

2082 Additionally, we derive the surrogate gradient corridor of the arctangent function, which is widely  
 2083 used as a surrogate gradient function for LIF neurons.  
 2084

Let  $u := z - \vartheta$  and consider the arctangent surrogate derivative  
 2085

2086 
$$\phi'(u) = \frac{\alpha_s}{\pi(1 + (\alpha_s u)^2)}, \quad \alpha_s > 0. \quad (18)$$
  
 2087

2088 For a target gradient floor  $\gamma \in (0, \alpha_s/\pi)$ , define the corridor(Li et al., 2024a; Zenke & Vogels, 2021;  
 2089 Shrestha & Orchard, 2018)  
 2090

2091 
$$\mathcal{C}_\gamma := \{u : \phi'(u) \geq \gamma\} = [-\delta, \delta], \quad \delta(\gamma) = \frac{1}{\alpha_s} \sqrt{\frac{\alpha_s}{\pi\gamma} - 1}. \quad (19)$$
  
 2092

2094 whose peak is  $A = 1/\pi$ . Setting the gradient floor to  $r = fA = f/\pi$  yields the corridor half-width  
 2095

2096 
$$\delta(f) = \frac{2}{\pi\alpha} \sqrt{\frac{1}{f} - 1}. \quad (20)$$
  
 2097

2098 In practice, we initialize  $\alpha = 2$  and  $f = 0.2$  (thus  $r \approx 0.0637$ ), then adapt  $f$  per layer using  
 2099 mini-batch membrane statistics so that the corridor covers a target score  $p$  of the observed  $U - \vartheta$   
 2100 distribution: with  $\hat{\sigma}_\ell$  the running standard deviation and  $z_p$  the normal quantile for score  $p$ , we set  
 2101  $\delta(f_\ell) \approx z_p \hat{\sigma}_\ell$ , i.e (Zenke & Vogels, 2021; Wang et al., 2023; Che et al., 2022; Lian et al., 2023).  
 2102

2103 
$$f_\ell = \frac{1}{1 + \left(\frac{\pi\alpha}{2} z_p \hat{\sigma}_\ell\right)^2}. \quad (21)$$
  
 2104

2105 This keeps most samples within the high-gradient band while avoiding an overly narrow corridor.

2106 **Remark 1** (Mapping to implementation). For the common parameterization  $\phi'(u) = \frac{\alpha_s}{\pi(1+(\alpha_s u)^2)}$ ,  
 2107 one has  $A = \alpha_s/\pi$  and  $\beta = \alpha_s$ . For the SpikingJelly ATan  $\phi'(u) = \frac{\alpha/2}{1+(\frac{\pi\alpha}{2}u)^2}$ , one has  $A = \alpha/2$  and  
 2108  $\beta = \pi\alpha/2$  (Fang et al., 2023). Both are instances of equation 16, so equation 17 applies verbatim.  
 2109

### 2111 D.3 FAULT MODELING

2112 We consider synaptic faults that perturb parameters and/or inputs:

$$2114 \quad w \mapsto w + \Delta w, \quad x \mapsto x + \Delta x, \quad (22)$$

2116 where  $\Delta w, \Delta x$  may be sparse (e.g., SA0/SA1 at a subset of synapses) or dense (e.g., analog drift).  
 2117 The post-fault pre-activation is

$$2119 \quad z' = (w + \Delta w)^\top (x + \Delta x) + b = z + \Delta z, \quad \Delta z = \underbrace{\Delta w^\top x}_{\text{param fault}} + \underbrace{w^\top \Delta x}_{\text{input fault}} + \underbrace{\Delta w^\top \Delta x}_{\text{higher-order}}. \quad (23)$$

2122 By the Cauchy–Schwarz inequality,

$$2124 \quad |\Delta z| \leq \|x\|_2 \|\Delta w\|_2 + \|w\|_2 \|\Delta x\|_2 + \|\Delta w\|_2 \|\Delta x\|_2. \quad (24)$$

2125 SA0 on an input line  $j$  is modeled by  $(\Delta x)_j = -x_j$ ; SA1 by  $(\Delta x)_j = c - x_j$  for a fixed logic level  
 2126  $c$ . Bit/weight stuck faults are included in  $\Delta w$ .

### 2128 D.4 FROM FAULTS TO SATURATION

2130 At time  $t$ , the only instantaneous change from a synaptic fault is  $z_t \mapsto z_t + \Delta z_t$ , hence

$$2132 \quad V'_t = \alpha V_{t-1} + (z_t + \Delta z_t) - \vartheta K_{t-1} = V_t + \Delta z_t, \quad \Rightarrow \quad V'_t - \vartheta = (V_t - \vartheta) + \Delta z_t. \quad (25)$$

2134 **Lemma 1** (Corridor escape: sufficient conditions). Let  $a_t := V_t - \vartheta$  and suppose  $|a_t| \leq \delta$  (pre-fault  
 2135 state inside the corridor).

- 2136 1. (Sign-aligned escape) If  $a_t \Delta z_t \geq 0$  and  $|\Delta z_t| \geq \delta - |a_t|$ , then  $|a_t + \Delta z_t| \geq \delta$ , hence  
 2137  $\sigma'(V'_t - \vartheta) \approx 0$  at time  $t$ .
- 2139 2. (Sign-agnostic escape) Regardless of the sign of  $\Delta z_t$ , if  $|\Delta z_t| > \delta + |a_t|$ , then  $|a_t + \Delta z_t| > \delta$ .

2141 *Proof.* (1) If  $a_t \Delta z_t \geq 0$  then  $|a_t + \Delta z_t| = ||a_t| + |\Delta z_t|| \geq \delta$  when  $|\Delta z_t| \geq \delta - |a_t|$ . (2) By the  
 2142 reverse triangle inequality,  $|a_t + \Delta z_t| \geq ||\Delta z_t| - |a_t|| > \delta$ .

### 2143 D.5 EXPECTED GRADIENT BOUND FOR A SINGLE NEURON

2145 Let  $g_t := \partial \mathcal{L} / \partial S_t$  and suppose  $0 \leq \sigma'(u) \leq C_\sigma \mathbf{1}\{|u| \leq \delta\}$ . Then,

$$2147 \quad \left\| \frac{\partial \mathcal{L}}{\partial w} \right\| = \left\| \sum_{t=1}^T g_t \sigma'(V'_t - \vartheta) x_t \right\| \leq C_\sigma \sum_{t=1}^T \|g_t\| \|x_t\| \mathbf{1}\{|V'_t - \vartheta| \leq \delta\}. \quad (26)$$

2150 Taking expectations and using the Cauchy–Schwarz inequality yields the model-free bound

$$2152 \quad \mathbb{E} \left\| \frac{\partial \mathcal{L}}{\partial w} \right\| \leq C_\sigma \sum_{t=1}^T \left( \mathbb{E} [\|g_t\|^2 \|x_t\|^2] \right)^{1/2} \cdot \mathbb{P}(|V'_t - \vartheta| \leq \delta)^{1/2}. \quad (27)$$

2155 Under a mild independence/mixing assumption between  $\|g_t\| \|x_t\|$  and the corridor event, one may  
 2156 write the simpler scaling

$$2158 \quad \mathbb{E} \left\| \frac{\partial \mathcal{L}}{\partial w} \right\| \lesssim C_\sigma \sum_{t=1}^T \mathbb{E} [\|g_t\| \|x_t\|] p_t, \quad p_t := \mathbb{P}(|V'_t - \vartheta| \leq \delta). \quad (28)$$

2160 D.6 DEPTH- AND TIME-WISE COMPOUNDING  
21612162 For a parameter in layer  $\ell$ , a generic backpropagation path contains factors  $\sigma'(V_t^{(j)} - \vartheta)$  for  $j \leq \ell$   
2163 and relevant  $t$ . Bounding  $\sigma'$  by indicators,  
2164

2165 
$$|\Pi| \leq C_\sigma^{N_\Pi} \prod_{j,t: \gamma_{j,t}=1} \mathbf{1}\{|V_t^{(j)} - \vartheta| \leq \delta\}, \quad N_\Pi = \sum_{j,t} \gamma_{j,t}. \quad (29)$$
  
2166

2167 Taking expectations gives ( $\Pi$  denotes the product of all gradient factors along a single backpropagation  
2168 path leading to a given parameter.)  
2169

2170 
$$\mathbb{E} |\Pi| \leq C_\sigma^{N_\Pi} \mathbb{P} \left( \bigcap_{j,t: \gamma_{j,t}=1} \{|V_t^{(j)} - \vartheta| \leq \delta\} \right). \quad (30)$$
  
2171

2172 A *conservative* bound is  
2173

2174 
$$\mathbb{E} |\Pi| \leq C_\sigma^{N_\Pi} \min_{j,t: \gamma_{j,t}=1} p_{j,t}, \quad p_{j,t} := \mathbb{P}(|V_t^{(j)} - \vartheta| \leq \delta). \quad (31)$$
  
2175

2176 If corridor events are approximately independent (or satisfy a weak-mixing condition), then  
2177

2178 
$$\mathbb{E} |\Pi| \leq C_\sigma^{N_\Pi} \prod_{j,t: \gamma_{j,t}=1} p_{j,t} \leq C_\sigma^{N_\Pi} (p^*)^{N_\Pi}, \quad p^* := \sup_{j,t} p_{j,t}, \quad (32)$$
  
2179

2180 exhibiting exponential attenuation as  $N_\Pi$  grows.  
21812182 D.7 FIRST-LAYER SENSITIVITY IN MLP  
21832184 For the first layer (vector form) with  $z^{(1)} = W^{(1)}x + b^{(1)}$  and perturbations  $(\Delta W^{(1)}, \Delta x)$ ,  
2185

2186 
$$\|\Delta z^{(1)}\| \leq \|\Delta W^{(1)}\|_{\text{op}} \|x\|_2 + \|W^{(1)}\|_{\text{op}} \|\Delta x\|_2 + \|\Delta W^{(1)}\|_{\text{op}} \|\Delta x\|_2, \quad (33)$$
  
2187

2188 so sizeable input/weight faults directly shift  $z^{(1)}$  without any preceding contraction, shrinking corridor  
2189 occupancy in deeper layers via equation 30–equation 32.  
21902191 D.8 SUFFICIENT CONDITION FOR GRADIENT COLLAPSE  
21922193 Define  $p_{j,t}$  as above and let  $\mathcal{G}$  be the multiset of “corridor gates” along dominant backpropagation  
2194 paths with size  $N_*$ . If a fraction  $\rho \in (0, 1]$  of gates satisfy  $p_{j,t} \leq \varepsilon \ll 1$ , then  
2195

2196 
$$\mathbb{E} |\Pi| \leq \begin{cases} C_\sigma^{N_*} \varepsilon^{\rho N_*}, & \text{under independence/mixing,} \\ C_\sigma^{N_*} \varepsilon, & \text{(conservative, no independence).} \end{cases} \quad (34)$$
  
2197

2198 Either case shows attenuation; the independent/mixing case yields exponential decay in depth  $\times$  time.  
21992200 D.9 EFFECTIVE BIAS INTERPRETATION FOR SA0/SA1 OF SAFs  
22012202 For SA1 on a subset  $\mathcal{J}$  of input lines with logic level  $c$ ,  
2203

2204 
$$\Delta z = w^\top \Delta x = \sum_{j \in \mathcal{J}} w_j(c - x_j) = c \sum_{j \in \mathcal{J}} w_j - \sum_{j \in \mathcal{J}} w_j x_j, \quad (35)$$
  
2205

2206 acting as an additive bias shift plus removal of signal terms. Persistent shifts displace  $V_t$  away from  
2207  $\vartheta$  across time steps, driving down corridor occupancy  $p_{j,t}$  and compounding the bottleneck via  
2208 equation 32.  
2209

2214 D.10 SUMMARY  
2215

2216 Synaptic faults induce a pre-activation shift  $\Delta z$  decomposed in equation 23 and bounded in equation  
2217 24. When  $|\Delta z|$  is large relative to the corridor width  $\delta$ , Lemma 1 ensures  $|V_t - \vartheta| > \delta$  so  
2218  $\sigma'(V_t - \vartheta) \approx 0$ . The expected gradient is then attenuated proportionally to (at least)  $\sqrt{p_{j,t}}$  per time  
2219 step equation 27; under independence/mixing, it scales with  $p_{j,t}$  equation 28. Across layers and time  
2220 steps, this attenuation multiplies equation 32, producing the *bottleneck problem*, with the first layer of  
2221 MLP especially vulnerable by equation 33.

2222 E NEAR-OPTIMALITY OF THE PROPOSED MECHANISM  
2223

2225 We show why our solution is the near-optimal solution to improve the fault tolerance of SNNs in this  
2226 section.

2228 E.1 SETUP AND NOTATION  
2229

2230 We consider inputs  $x \in \mathbb{R}^n$  and a fixed number of stripes (1D profiles in Section 5)  $T \in \mathbb{N}$ . Indices  
2231 are  $i \in \{1, \dots, n\}$  and stripes are  $t \in \{1, \dots, T\}$ . A stripe partition is represented by binary masks  
2232  $M_t(i) \in \{0, 1\}$  that satisfy  $\sum_{i=1}^T M_t(i) = 1$  for every  $i$ , and contiguity is taken with respect to a  
2233 one-dimensional scan order of the indices induced by an angle  $\theta$  in a finite set  $\Theta \subset [0, \pi)$ . Given  
2234 any nonnegative vector  $s \in \mathbb{R}_+^n$ , the load of stripe  $t$  is the linear functional  $S_t(s) = \sum_i s_i M_t(i)$ ; we  
2235 also write the total mass  $U(s) = \sum_i s_i$ , the per-stripe mean  $\mu(s) = U(s)/T$ , and the element-wise  
2236 maximum  $m(s) = \max_i s_i$ . For vectors  $a, b \in \mathbb{R}^n$ , the inner product is  $\langle a, b \rangle = \sum_i a_i b_i$  and  $\|v\|_p$   
2237 denotes the  $\ell_p$  norm; the Hadamard product is  $a \odot b$ .

$$2239 S_t(s) := \sum_{i=1}^n s_i M_t(i), \quad U(s) := \sum_{i=1}^n s_i, \quad \mu(s) := \frac{U(s)}{T}, \quad m(s) := \max_i s_i. \quad (36)$$

2242 Given trained weights  $w \in \mathbb{R}^n$  and a fault/perturbation  $\Delta w$ , we set  $\hat{w} := w + \Delta w$  and restrict the  
2243 input to stripe  $t$  by  $x_t := x \odot M_t$ . The (stripe) pre-activation is

$$2245 z_t := \langle \hat{w}, x_t \rangle, \quad x_t := x \odot M_t, \quad \hat{w} := w + \Delta w. \quad (37)$$

2246 We denote by  $z^* > 0$  the corridor threshold, i.e., the largest value for which the chosen surrogate  
2247 derivative  $\phi'(z)$  remains in its effective (non-vanishing) regime for all  $|z| \leq z^*$ . To construct stripes,  
2248 we employ an implementable importance map  $I \in \mathbb{R}_+^n$  and assume a two-sided calibration with  
2249 respect to the ideal per-index load  $u_i := |w_i| |x_i|$ : there exist constants  $0 < c_- \leq 1 \leq c_+$  such that

$$2251 c_- |w_i| |x_i| \leq I_i \leq c_+ |w_i| |x_i|, \quad i = 1, \dots, n. \quad (38)$$

2253 When  $I = u$  one has  $c_- = c_+ = 1$ . The quantile (greedy) stripes used in the paper are obtained by  
2254 scanning indices in the chosen order and inserting a cut whenever the cumulative load with respect to  
2255  $I$  first exceeds integer multiples of  $\mu(I)$ , producing  $T$  contiguous fragments.

2256 E.2 FAULT MODELS AND A BASIC UPPER BOUND  
2257

2259 We consider the following three fault models, mentioned in Section 2.

2260 **SAFs:** Some synapses are permanently stuck at  $G_{\min}$  or  $G_{\max}$  so the implemented weight becomes  
2261  $w'_i$  (e.g., SA0/SA1). Let  $\Delta w_i := w'_i - w_i$  and assume  $\|\Delta w\|_\infty \leq \varepsilon_{\text{SAF}}$ . Then for any stripe  $t$  (Boyd  
2262 & Vandenberghe, 2004),

$$2264 |z_t| = |\langle w + \Delta w, x_t \rangle| \leq \underbrace{\sum_i |w_i| |x_i| M_t(i)}_{S_t(u)} + \varepsilon_{\text{SAF}} \underbrace{\sum_i |x_i| M_t(i)}_{S_t(|x|)} = S_t(u) + \varepsilon_{\text{SAF}} S_t(|x|). \quad (39)$$

**RWFs:** Each coordinate experiences an independent, mean-zero, bounded (or sub-Gaussian) perturbation  $\Delta w_i$ . If  $|\Delta w_i| \leq b$  and the  $\Delta w_i$  are independent, then for any  $\tau > 0$  and stripe  $t$ ,

$$\Pr(|\langle \Delta w, x_t \rangle| > \tau) \leq 2 \exp\left(-\frac{\tau^2}{2b^2 \|x_t\|_2^2}\right), \quad (40)$$

so equalizing  $S_t(|x|) = \|x_t\|_1$  across  $t$  uniformly tightens the tail bound (sub-Gaussian and Hoeffding) (Hoeffding, 1963).

**CEFs:** Wiring errors apply a linear transformation to the input so that  $z_t = w^\top (Ax_t)$ . This is equivalent to using the effective weight  $w' := A^\top w$ , i.e.,  $\Delta w^{(c)} := (A^\top - I)w$ . If  $\|\Delta w^{(c)}\|_\infty \leq \varepsilon_{\text{CEF}}$ , then

$$|z_t| = |\langle w + \Delta w^{(c)}, x_t \rangle| \leq S_t(u) + \varepsilon_{\text{CEF}} S_t(|x|). \quad (41)$$

A permutation fault  $A = P$  is a special case; taking  $\varepsilon_{\text{CEF}} = \|(P^\top - I)w\|_\infty$  yields the same bound (Boyd & Vandenberghe, 2004).

### E.3 CALIBRATION: ALIGNING THE IMPORTANCE MAP WITH THE EFFECTIVE PER-INDEX LOAD

We formalize the requirement that the implementable importance  $I$  should approximate  $u$  within stripe-wise sums.

**Assumption 1** (Two-sided calibration.). *There exist constants  $0 < c_- \leq 1 \leq c_+$  such that for all indices  $i$ ,*

$$c_- u_i \leq I_i \leq c_+ u_i. \quad (42)$$

**Lemma 2** (Calibration). *Under the assumption (Two-sided calibration), for any stripe partition,*

$$S_t(u) \leq \frac{1}{c_-} S_t(I), \quad \mu(u) \leq \frac{1}{c_-} \mu(I), \quad m(u) \leq \frac{1}{c_-} m(I). \quad (43)$$

*Proof.* From  $u_i \leq I_i/c_-$ , sum over  $i$  in stripe  $t$ . Similar for totals and maxima.

### E.4 QUANTILE STRIPES ARE ADDITIVELY NEAR-OPTIMAL (CONTIGUOUS CASE)

Fix a nonnegative sequence  $a_1, \dots, a_n$  obtained by scanning the image along any 1D order (e.g., the  $\theta$ -scan used in the main text). Let  $U(a) = \sum_i a_i$  and target mean  $\mu(a) = U(a)/T$ . Define the *quantile (greedy) contiguous partition* in Subsections 5.2 and 5.3 by sweeping from left to right and cutting whenever the cumulative sum first exceeds multiples of  $\mu(a)$ , producing  $T$  contiguous stripes.

**Lemma 3** (Additive bound for greedy quantiles). *Let  $m(a) := \max_i a_i$ . Then the greedy quantile partition satisfies*

$$\max_{t \leq T} S_t(a) \leq \mu(a) + m(a). \quad (44)$$

Moreover, any contiguous partition must have  $\max_t S_t(a) \geq \mu(a)$ ; hence, the greedy partition is a  $+m(a)$ -additive approximation to the optimal contiguous partition.

*Proof.* Each of the first  $T - 1$  stripes stops at the first index that causes the running sum to exceed  $\mu(a)$ . The overshoot over  $\mu(a)$  is therefore at most the last included element, i.e.,  $\leq m(a)$ . Hence every one of the first  $T - 1$  stripes has load in  $(\mu(a), \mu(a) + m(a)]$ . The final stripe has the remaining mass  $U(a) - \sum_{t=1}^{T-1} S_t(a) \leq \mu(a)$ . Thus, the maximum stripe load is at most  $\mu(a) + m(a)$ . The lower bound  $\geq \mu(a)$  holds by a pigeonhole argument.

**Theorem 1** (Near-optimality for  $u$  via quantiles on  $I$ ). *Construct stripes by greedy quantiles on the calibrated importance  $I$ . Under Assumption 1:*

$$\max_t S_t(u) \leq \frac{1}{c_-} (\mu(I) + m(I)). \quad (45)$$

If  $I = u$  (so  $c_- = c_+ = 1$ ), the greedy partition achieves  $\max_t S_t(u) \leq \mu(u) + m(u)$ , i.e., a  $+m(u)$  additive approximation to the optimal contiguous value. For a calibrated  $I$  with Assumption 1, we have  $\max_t S_t(u) \leq \frac{1}{c_-}(\mu(I) + m(I))$ . Translating this bound to the  $u$ -optimum introduces a calibration-dependent drift via  $\mu(I) \in [c_- \mu(u), c_+ \mu(u)]$ , so the additive gap to the optimal contiguous value is at most  $\frac{1}{c_-}m(I) + (\frac{c_+}{c_-} - 1)\mu(u)$ . The baseline  $\mu(u)$  is at most  $\frac{1}{c_-}\mu(I)$ . Proof. Apply Lemma 3 with  $a = I$  to obtain  $\max_t S_t(I) \leq \mu(I) + m(I)$ . Then use Lemma 2:  $S_t(u) \leq S_t(I)/c_-$ .

**Remark 2** (Direct partitioning condition). (i) If one directly partitions using  $a = u$ , then  $c_- = 1$  and the bound gives  $\max_t S_t(u) \leq \mu(u) + m(u)$ . (ii) The proof does not assume the particular 1D order beyond contiguity; the order may be induced by any scan (e.g., the  $\theta$ -parameterization used to define stripes).

## E.5 CORRIDOR PRESERVATION: SUFFICIENT CONDITIONS

Under SAFs and CEFs, combining the bounds with Theorem 1 yields a closed-form uniform bound on  $|z_t|$ :

$$|z_t| \leq \underbrace{\frac{1}{c_-}(\mu(I) + m(I))}_{\text{from } u} + \underbrace{\varepsilon S_t(|x|)}_{\text{fault term}}. \quad (46)$$

The stripes are constructed by greedy quantiles on  $I$  (not on  $|x|$ ). Let  $X_{\max} := \max_{t \leq T} \text{St}(|x|)$ , computed on the *same*  $I$ -quantile partition. A simple sufficient condition for staying within the corridor is then

$$\frac{1}{c_-}\{\mu(I) + m(I)\} + \varepsilon X_{\max} \leq z^*, \quad X_{\max} := \max_{t \in [T]} S_t(|x|) \text{ (computed on the } \text{same } I\text{-quantile partition).} \quad (47)$$

**Remark 3** (Optional (co-monotone scan)). If along the 1D scan used to build the  $I$ -quantile partition the sequences  $I$  and  $|x|$  are approximately co-monotone—so that applying Lemma 3 to  $|x|$  is justified—then

$$X_{\max} \leq \mu(|x|) + m(|x|). \quad (48)$$

In this case, a convenient sufficient condition is

$$\frac{1}{c_-}\{\mu(I) + m(I)\} + \varepsilon(\mu(|x|) + m(|x|)) \leq z^*. \quad (49)$$

Under RWFs, Hoeffding’s tail (and a union bound) implies that with probability at least  $1 - 2T \exp\{-\tau^2/(2b^2 \max_t \|x_t\|_2^2)\}$ , all stripes satisfy  $|\langle \Delta w, x_t \rangle| \leq \tau$  (Hoeffding, 1963). Thus, the (random) bound analogous to the above holds with the deterministic term  $\varepsilon S_t(|x|)$  replaced by  $\tau$ , chosen at the desired confidence level.

## E.6 ON THE GINI OBJECTIVE (PRIMARY SURROGATE FOR MIN-MAX LOAD)

We treat *minimizing the Gini coefficient of the 1D projection of  $I$*  as a **primary surrogate** for suppressing the worst-case stripe load. Recall that  $G(S)$  equals one-half of the relative mean absolute difference and is equivalent to the Lorenz-based definition. Hence, it directly reduces pairwise dispersion. The next proposition turns this dispersion control into a deviation bound that is *linear* in  $G(S)$  (Yitzhaki & Schechtman, 2013).

**Proposition 1** (Gini  $\Rightarrow$  deviation bound). Let  $S \in \mathbb{R}_+^T$  with mean  $\mu$  and Gini coefficient  $G(S)$ . Then

$$\max_t |S_t - \mu| \leq \frac{1}{T} \sum_{i,j} |S_i - S_j| = 2T \mu G(S).$$

2376 *Proof.* By  $\sum_j (S_t - S_j) = T(S_t - \mu)$  and the triangle inequality,  $|S_t - \mu| = \frac{1}{T} |\sum_j (S_t - S_j)| \leq$   
 2377  $\frac{1}{T} \sum_j |S_t - S_j|$ . Summing over  $t$  and taking the maximum yields  $\max_t |S_t - \mu| \leq \frac{1}{T} \sum_{i,j} |S_i - S_j|$ .  
 2378 Since  $\sum_{i,j} |S_i - S_j| = 2T^2 \mu G(S)$ , the claim follows.  
 2379

2380 Combine Proposition 1 with the additive near-optimality bound for contiguous quantile stripes  
 2381 (Lemma/Theorem:  $\max_t S_t \leq \mu + m$  for the greedy split). Minimizing  $G(S)$  tightens  $\max_t |S_t - \mu|$   
 2382 and thus reduces  $\max_t S_t$  under the same partition, making the corridor constraint strictly easier to  
 2383 satisfy. In short: **Gini**  $\downarrow \Rightarrow$  pairwise dispersion  $\downarrow \Rightarrow$  deviation  $\downarrow \Rightarrow$  min–max load  $\downarrow$ .  
 2384

## 2385 E.7 COMPUTING THE SCAN/STRIPES

2386 Let  $\Theta \subset [0, \pi]$  denote a finite set of scan angles (or any family of 1D orders). For a fixed order, the  
 2387 greedy quantile partition runs in linear time. If one wishes to *search* over  $\Theta$ , evaluate the objective  
 2388  $\max_t S_t(I)$  for each order and pick the best; since the objective only changes at permutation “event  
 2389 points”, coarse uniform sampling of  $\Theta$  is typically sufficient in practice. When an exact optimum  
 2390 over contiguous partitions is desired for a fixed order, classical Dynamic Programming (DP) or  
 2391 feasibility–check with binary search finds  $\min_{\text{contig}} \max_t S_t(I)$  in polynomial time; our greedy rule  
 2392 is the simple additive-approximate alternative used in the paper (Skiena, 2008).  
 2393

## 2394 E.8 SUMMARY

2395 For any calibrated  $I$ , greedy quantile stripes achieve the near–optimality bound above; if  $I = u$ ,  
 2396 the achieved maximum load is within  $+m(u)$  of the contiguous optimum for  $u$ . Under the SAFs  
 2397 and CEFs, the closed-form sufficient condition ensures  $|z_t| \leq z^*$  for all stripes, preventing gradient  
 2398 collapse; under RWFs, the analogous high-probability statement follows from the sub-Gaussian tail  
 2399 bound. The constants involved are the calibration  $c_-$ , the fault radius  $\varepsilon$  (or  $(b, \tau)$  in the probabilistic  
 2400 model), and the observable statistics  $\mu(\cdot)$  and  $m(\cdot)$ .  
 2401

## 2402 F FAULT-TOLERANCE CAPACITY PREDICTION OF OUR MECHANISM

2403 In this section, we analyze the fault-tolerance capacity of our mechanism under the SAF, RWF, and  
 2404 CEF injection using arctangent as a surrogate gradient function. The boundary of synaptic weights is  
 2405  $[-1, 1]$  (Le Gallo et al., 2023; Lammie et al., 2022).  
 2406

### 2407 F.1 SETUP AND NOTATION

2408 Let  $w \in [-1, 1]^N$  be the clean weight vector,  $K := \|w\|_2$ , and let a fraction  $\rho \in [0, 1]$  of synapses be  
 2409 faulty. All results below are per layer and can be applied layer-wise. Please refer to the derivation  
 2410 of the surrogate gradient (arctangent) corridor in Subsection C.2 while reading our paragraphs on  
 2411 capacity calculation.  
 2412

2413 With dynamic fragmentation and per-fragment RMS normalization to  $\|\tilde{x}_t\|_2 = \alpha_n$ ,  
 2414

$$2415 |u_t| = |\hat{w}^\top \tilde{x}_t + b - \vartheta| \leq \|\hat{w}\|_2 \alpha_n + m, \quad m := |b - \vartheta|. \quad (50)$$

2416 Hence it suffices that  $\|\hat{w}\|_2 \leq B$ , where  
 2417

$$2418 B := \frac{\delta(\gamma) - m}{\alpha_n} \quad (\text{requires } \delta(\gamma) > m). \quad (51)$$

### 2420 F.2 CAPACITY UNDER SAFS

2421 Under SA0, we replace faulty entries by  $-1$ ; under SA1 by  $+1$ . In either case  $|\hat{w}_i| = 1$  on faulty  
 2422 indices, so  
 2423

$$2424 \|\hat{w}\|_2^2 = \|w\|_2^2 - \sum_{i \in F} w_i^2 + \rho N \cdot 1 \leq K^2 + \rho N, \quad (52)$$

where the inequality is the *deterministic worst-case* (we drop the nonnegative subtraction term). Therefore, a sufficient condition to remain inside the corridor is

$$K^2 + \rho N \leq B^2 \implies \rho_{\text{SA}\pm, \text{worst}}^* = \frac{B^2 - K^2}{N} \text{ (clipped to } [0, 1]). \quad (53)$$

If faulty indices are drawn *uniformly at random* (independent of  $w$ ), then  $\mathbb{E}[\sum_{i \in F} w_i^2] = \rho K^2$  and

$$\mathbb{E}\|\hat{w}\|_2^2 = (1 - \rho)K^2 + \rho N \cdot 1 = K^2 + \rho(N - K^2), \quad (54)$$

whence the *in-expectation* capacity is

$$\rho_{\text{SA}\pm, \text{exp}}^* = \frac{B^2 - K^2}{N - K^2} \text{ (clipped to } [0, 1]). \quad (55)$$

### F.3 CAPACITY UNDER RWFs

On faulty indices,  $\hat{w}_i = w_i + \varepsilon_i$  with  $\mathbb{E}[\varepsilon_i] = 0$  and  $\text{Var}(\varepsilon_i) = \sigma_w^2$ . Independence yields  $\mathbb{E}\|\hat{w}\|_2^2 = K^2 + \rho N \sigma_w^2$ , so

$$\rho_{\text{RWF}, \text{exp}}^* = \frac{B^2 - K^2}{N \sigma_w^2} \text{ (clipped to } [0, 1]). \quad (56)$$

A high-probability version follows from sub-Gaussian concentration by replacing  $N \sigma_w^2$  with an upper-tail bound.

### F.4 CAPACITY UNDER CEFs

A fraction  $\rho$  of entries are replaced by i.i.d.  $U[a, b]$  and then frozen. Let  $\mu_f = \frac{a+b}{2}$  and  $\sigma_f^2 = \frac{(b-a)^2}{12}$  so that  $\mathbb{E}[\hat{w}_i^2] = \mu_f^2 + \sigma_f^2$ . If faulty indices are random (independent of  $w$ ),

$$\mathbb{E}\|\hat{w}\|_2^2 = (1 - \rho)K^2 + \rho N(\mu_f^2 + \sigma_f^2) \Rightarrow \rho_{\text{CEF}, \text{exp}}^* = \frac{B^2 - K^2}{N(\mu_f^2 + \sigma_f^2) - K^2} \text{ (clipped to } [0, 1]). \quad (57)$$

For the common symmetric case  $U[-1, 1]$ ,  $\mu_f = 0$ ,  $\sigma_f^2 = 1/3$  and thus

$$\rho_{\text{CEF}, \text{exp}}^* = \frac{B^2 - K^2}{N/3 - K^2} \text{ (clipped).} \quad (58)$$

If a *deterministic worst-case* guarantee is required (independent of the draw), note that  $|\hat{w}_i| \leq 1$  almost surely, so the same bound as SA0/SA1 applies:

$$\rho_{\text{CEF}, \text{worst}}^* = \frac{B^2 - K^2}{N} \text{ (clipped to } [0, 1]). \quad (59)$$

### F.5 SUMMARY

Here, we explain how to calculate the capacity of the proposed mechanism. Choose a gradient floor  $\gamma$  (e.g.,  $f\%$  of the arctangent peak so  $\gamma = f \cdot \alpha_s/\pi$ ), compute  $\delta(\gamma)$  and  $B$  via equation 51, measure  $K = \|w\|_2$ , and then plug into the formula for the fault model of interest. If  $\rho \leq \rho^*$ , our mechanism keeps  $|u_t| \leq \delta(\gamma)$  for all steps (deterministic case) or in expectation (stochastic case), thereby ensuring  $\phi'(u_t) \geq \gamma$ .

## G CONVERGENCE ANALYSIS WITH THE PROPOSED MECHANISM

We present that Stochastic Gradient Descent (SGD) and Gradient Descent (GD) optimizers derive gradients of fault-injected SNN models and induce the models to update weights when we adopt our mechanism to the SNN models.

2484  
2485

## G.1 SETUP AND NOTATION

2486  
2487  
2488  
2489  
2490  
2491  
2492  
2493

We denote a data sample by  $(x, y)$ , and the SNN by  $f_W(\cdot)$  with parameters  $W$ . We include the (possibly stochastic) fragment+RMS transform  $T$  and analyze the expected objective  $\tilde{L}(W) = \mathbb{E}_{(x,y), T}[\ell(f_W(T(x)), y)]$ . At step  $t$ , with mini-batch estimator  $g_t$  and step size  $\eta_t$ , the update is  $W_{t+1} = W_t - \eta_t g_t$ . For spiking neurons, we write the pre-activation as  $u_t := z_t - \vartheta$  and use a surrogate derivative  $\phi'(u)$ . Throughout, we assume the *gradient-corridor* condition  $\phi'(u_t) \geq \gamma$  holds along the iterates, which is enforced by the fragment RMS bound and the per-layer effective weight norms  $\|\hat{w}^{(\ell)}\|_2 \leq B^{(\ell)}$  referring to Appendix E. Symbols  $L, \sigma^2, \mu$  are in Appendix C, D, and E, referenced only when required by a lemma or theorem.

2494

## G.2 BAND CONDITION ENFORCED BY OUR MECHANISM

2495  
2496  
2497

With dynamic fragmentation and per-fragment RMS normalization  $\|\tilde{x}_t\|_2 = \alpha_n$ , each step satisfies

2498  
2499

$$|u_t| = |\hat{w}^\top \tilde{x}_t + b - \vartheta| \leq \|\hat{w}\|_2 \alpha_n + m, \quad m := |b - \vartheta|. \quad (60)$$

2500  
2501

Defining

2502  
2503  
2504

$$B := \frac{\delta(\gamma) - m}{\alpha_n} \quad (\text{requires } \delta(\gamma) > m), \quad (61)$$

2505

One obtains the following corridor-invariance lemma.

2506  
2507  
2508

**Lemma 4** (Corridor invariance). *If  $\|\hat{w}\|_2 \leq B$ , then  $|u_t| \leq \delta(\gamma)$  for all fragments  $t$ , hence  $\phi'(u_t) \geq \gamma$ . Proof. Combine equation 60 with equation 61 and the definition of  $\delta(\gamma)$  in equation 17.*

2509  
2510

## G.3 OPTIMIZATION OBJECTIVE AND ASSUMPTIONS

2511  
2512

Let  $\tilde{\mathcal{L}}(W) := \mathbb{E}_{(x,y), \mathcal{T}}[\ell(f_W(\mathcal{T}(x)), y)]$ , where  $\mathcal{T}$  denotes the (possibly stochastic, data/model-aware) transformation induced by our mechanism (e.g., masks and RMS scaling). Assume:

2513  
2514

**Assumption 2** ( $L$ -smoothness).  $\nabla \tilde{\mathcal{L}}$  is  $L$ -Lipschitz.

2515  
2516  
2517

**Assumption 3** (Unbiased mini-batch gradients, bounded variance).  $\mathbb{E}[g_t | W_t] = \nabla \tilde{\mathcal{L}}(W_t)$  and  $\mathbb{E}[\|g_t - \nabla \tilde{\mathcal{L}}(W_t)\|^2 | W_t] \leq \sigma^2$ .

2518  
2519

**Assumption 4** (Corridor stability). *For each layer, capacity constraints on the fault ratio ensure  $\|\hat{w}^{(\ell)}\|_2 \leq B^{(\ell)}$ , so Lemma holds layer-wise and  $\phi'(u_t^{(\ell)}) \geq \gamma$  during training.*

2520

## G.4 DESCENT LEMMA AND MASTER INEQUALITY

2521  
2522

By  $L$ -smoothness and  $W_{t+1} = W_t - \eta_t g_t$ ,

2523  
2524  
2525  
2526

$$\tilde{\mathcal{L}}(W_{t+1}) \leq \tilde{\mathcal{L}}(W_t) - \eta_t \langle \nabla \tilde{\mathcal{L}}(W_t), g_t \rangle + \frac{L\eta_t^2}{2} \|g_t\|^2. \quad (62)$$

2527  
2528  
2529

Taking expectation and using Assumption 2 with  $\mathbb{E}\|g_t\|^2 = \|\nabla \tilde{\mathcal{L}}(W_t)\|^2 + \mathbb{E}\|g_t - \nabla \tilde{\mathcal{L}}(W_t)\|^2 \leq \|\nabla \tilde{\mathcal{L}}(W_t)\|^2 + \sigma^2$  gives (Nesterov, 2014)

2530  
2531  
2532

$$\mathbb{E}[\tilde{\mathcal{L}}(W_{t+1})] \leq \mathbb{E}[\tilde{\mathcal{L}}(W_t)] - \eta_t \left(1 - \frac{L\eta_t}{2}\right) \mathbb{E}[\|\nabla \tilde{\mathcal{L}}(W_t)\|^2] + \frac{L\eta_t^2}{2} \sigma^2. \quad (63)$$

2533  
2534  
2535

**Theorem 2** (SGD convergence to stationarity). *If  $\eta_t \equiv \eta \in (0, 1/L]$ , summing equation 63 over  $t = 0, \dots, T-1$  yields*

2536  
2537

$$\frac{1}{T} \sum_{t=0}^{T-1} \mathbb{E}[\|\nabla \tilde{\mathcal{L}}(W_t)\|^2] \leq \frac{2(\tilde{\mathcal{L}}(W_0) - \tilde{\mathcal{L}}^*)}{\eta T} + L\eta\sigma^2. \quad (64)$$

2538 With a Robbins–Monro schedule ( $\sum_t \eta_t = \infty$ ,  $\sum_t \eta_t^2 < \infty$ ) we obtain  
 2539  $\lim_{T \rightarrow \infty} \min_{t < T} \mathbb{E} \|\nabla \tilde{\mathcal{L}}(W_t)\|^2 = 0$ . *Role of Assumption 3:* By preventing artificial saturation  
 2540 ( $\phi'(u) \approx 0$ ), the corridor ensures that gradient signals remain informative until genuine  
 2541 stationarity (Bottou et al., 2018).

2542 **Theorem 3** (Monotone decrease for full-batch GD). *In the deterministic case ( $\sigma = 0$ ) with  $\eta \in$   
 2543  $(0, 1/L]$ ,*

$$2545 \quad \tilde{\mathcal{L}}(W_{t+1}) \leq \tilde{\mathcal{L}}(W_t) - \frac{\eta}{2} \|\nabla \tilde{\mathcal{L}}(W_t)\|^2, \quad (65)$$

2547 so  $\sum_t \|\nabla \tilde{\mathcal{L}}(W_t)\|^2 < \infty$  and every limit point of  $\{W_t\}$  is stationary.

2549 **Corollary 1** (Linear rate under PL). *If  $\tilde{\mathcal{L}}$  satisfies the Polyak–Łojasiewicz (PL) inequality  
 2550  $\frac{1}{2} \|\nabla \tilde{\mathcal{L}}(W)\|^2 \geq \mu(\tilde{\mathcal{L}}(W) - \tilde{\mathcal{L}}^*)$  for some  $\mu > 0$  on the corridor-stable region, then for GD  
 2551 with  $\eta \in (0, 1/L]$  (Karimi et al., 2020),*

$$2553 \quad \tilde{\mathcal{L}}(W_t) - \tilde{\mathcal{L}}^* \leq (1 - \eta\mu)^t (\tilde{\mathcal{L}}(W_0) - \tilde{\mathcal{L}}^*). \quad (66)$$

## 2555 G.5 SUMMARY

2557 Our mechanism enforces equation 17–equation 61 so that surrogate gradients do not vanish spuri-  
 2558 ously; Under standard smoothness/stochasticity assumptions, SGD converges to stationarity, and  
 2559 GD decreases monotonically, with linear rates under PL. Capacity bounds on the fault ratio provide  
 2560 concrete regimes where the corridor assumption holds layer-wise (Neftci et al., 2019).

2561  
 2562  
 2563  
 2564  
 2565  
 2566  
 2567  
 2568  
 2569  
 2570  
 2571  
 2572  
 2573  
 2574  
 2575  
 2576  
 2577  
 2578  
 2579  
 2580  
 2581  
 2582  
 2583  
 2584  
 2585  
 2586  
 2587  
 2588  
 2589  
 2590  
 2591